NASA Contractor Report 187226

Dynamic Delamination Crack Propagation in a Graphite/ Epoxy Laminate

J.E. Grady and C.T. Sun
Purdue University
West Lafayette, Indiana

October 1991

Prepared for
Lewis Research Center
Under Grant NAG3–211

National Aeronautics and Space Administration

TABLE OF CONTENTS

	Page
LIST OF TABLES	iii
LIST OF FIGURES	iv
ABSTRACT	ix
1. INTRODUCTION	1
2. EXPERIMENTAL APPARATUS AND PROCEDURE FOR IMPACT TESTING	6
2.1 Impact Specimen Preparation	6
2.2 Ballistic Impact Testing of Composite Specimens	6
2.3 Measurement of Delamination	7
3. IMPACT RESPONSE OF CRACKED LAMINATES - EXPERIMENTAL RESULTS	14
3.1 Threshold Impact Velocity	14
3.2 Dynamic Crack Propagation	15
3.2.1 Midplane Delamination	15
3.2.2 Off-Midplane Delamination	17
3.3 Stiffness Loss Due to Delamination	18
4. MODELING THE IMPACT FORCE	55
4.1 Model 1 - Preliminary Model	55
4.2 Model 2 - Experimental Model	56
4.2.1 Impact of a Longitudinal Bar	57
4.2.1.1 Hertzian Contact Law - Analysis of Low Speed Longitudinal Impact of a Bar	57
4.2.1.2 High Speed Longitudinal Impact of a Bar	62
4.2.2 High Speed Transverse Impact of a Laminated Beam	63
4.3 Contact Area and Impact Force	66
5. INSTABILITY OF DELAMINATION CRACKS - CRITICAL STRAIN ENERGY RELEASE RATE	105
5.1 Equivalent Moduli	105

Page

5.2 Finite Element Modeling. 113
5.3 Strain Energy Release Rate 117
5.3.1 Verification of Crack Closure Method. 118
5.4 Impact Analysis of Cracked Laminates 120

6. SUMMARY. 142

LIST OF REFERENCES. 146

LIST OF TABLES

Table		Page
3.1	Variation of Delaminated Area with Impact Velocity for Specimen Configuration A.	21
3.2	Variation of Delaminated Area with Impact Velocity for Specimen Configuration B.	22
3.3	Variation for Delaminated Area with Impact Velocity for Specimen Configuration C.	23
3.4	Variation of Delaminated Area with Impact Velocity for Specimen Configuration D.	24
3.5	Variation of Delaminated Area with Impact Velocity for Specimen Configuration E.	25
3.6	Variation of Delaminated Area with Impact Velocity for Specimen Configuration F.	26
3.7	Variation of Delaminated Area with Impact Velocity for Specimen Configuration H.	27
4.1	Force Histories Used in Analysis of Impact on Short Composite Beam Specimen	68
4.2	Force Histories Used in Analysis of Impact on Long Composite Beam Specimen	69
5.1	Force Histories Used in Analysis of Pre-Cracked Composite Beam Specimens.	124

LIST OF FIGURES

Figure		Page
2.1	Nominal Impact Specimen Dimensions.	9
2.2	Ballistic Impact Experimental Set-Up.	10
2.3	Camera Arrangement.	11
2.4	Lighting Arrangement.	12
2.5	Ultrasonic C-Scans of Impacted Specimens.	13
3.1	Impact Specimen Configurations.	28
3.2	Delaminated Area Versus Impact Energy for Specimen Configuration A	29
3.3	Delaminated Area Versus Impact Energy for Specimen Configuration B	30
3.4	Delaminated Area Versus Impact Energy for Specimen Configuration C	31
3.5	Delaminated Area Versus Impact Energy for Specimen Configuration D	32
3.6	Delaminated Area Versus Impact Energy for Specimen Configuration E	33
3.7	Delaminated Area Versus Impact Energy for Specimen Configuration H	34
3.8	Impact Response of Specimen E8.	35
3.9	Crack Propagation History in Specimen E8.	36
3.10	Impact Response of Specimen B6.	37
3.11	Crack Propagation History in Specimen B6.	38
3.12	Impact Response of Specimen G1.	39
3.13	Crack Propagation History in Specimen G1.	40
3.14	Impact Response of Specimen H4.	41

Page

3.15 Crack Propagation History in Specimen H4. 42

3.16 Impact Response of Specimen C4. 43

3.17 Crack Propagation History in Specimen C4. 45

3.18 Impact Response of Specimen C7. 46

3.19 Crack Propagation History in Specimen C7. 48

3.20 Vibration Test Set-Up 49

3.21 Natural Frequency Versus Delaminated Area for First Bending Mode. 50

3.22 Natural Frequency Versus Delaminated Area for Second Bending Mode. 51

3.23 Natural Frequency Versus Delaminated Area for Third Bending Mode. 52

3.24 Natural Frequency Versus Delaminated Area for Fourth Bending Mode. 53

3.25 Natural Frequency Versus Delaminated Area for Fifth Bending Mode. 54

4.1 Strain History at Impact Point of Beam Subjected to 1166 in/s Impact with Half-Inch Diameter Rubber Impactor. 70

4.2 Strain History 2.0 Inches From Impact Point of Beam Subjected to 1166 in/s Impact with Half-Inch Diameter Rubber Impactor. 71

4.3 Longitudinal Bar Experimental Set-Up. 72

4.4 Force History From 6.21 in/s Impact of 5/8 Inch Diameter Steel Ball on Aluminum Bar 73

4.5 Strain History at Midpoint of Bar From 62.1 in/s Impact of 5/8 Inch Diameter Steel Ball. 74

4.6 Propagation and Reflection of Longitudinal Strain Pulse From 62.1 in/s Impact of 5/8 Inch Diameter Steel Ball. 75

4.7 Force History Measured From 3500 in/s Impact of Half-Inch Diameter Impactor 76

Page

4.8 Force Amplitude Versus V^2 for Half-Inch Diameter Impactor. 77

4.9 Inverse Contact Time Versus Impact Velocity for Half-Inch Diameter Impactor 78

4.10 t_{F_o} /T Versus Impact Velocity for Half-Inch Diameter Impactor 79

4.11 Measured Impulse Versus Incident Momentum for Half-Inch Diameter Impactor 80

4.12 Force Amplitude Versus V^2 for 3/8 Inch Diameter Impactor. 81

4.13 Inverse Contact Time Versus Impact Velocity for 3/8 Inch Diameter Impactor. 82

4.14 t_{F_o} /T Versus Impact Velocity for 3/8 Inch Diamter Impactor. 83

4.15 Measured Impulse Versus Incident Momentum for 3/8 Inch Diameter Impactor. 84

4.16 Strain History at Gage 1 in Short Beam Specimen Using Force History No. 1 85

4.17 Strain History at Gage 2 in Short Beam Specimen Using Force History No. 1 86

4.18 Strain History at Gage 1 in Short Beam Specimen Using Force History No. 2 87

4.19 Strain History at Gage 2 in Short Beam Specimen Using Force History No. 2 88

4.20 Strain History at Gage 1 in Short Beam Specimen Using Force History No. 3 89

4.21 Strain History at Gage 2 in Short Beam Specimen Using Force History No. 3 90

4.22 Strain History at Gage 1 in Short Beam Specimen Using Force History No. 4 91

4.23 Strain History at Gage 2 in Short Beam Specimen Using Force History No. 4 92

Page

4.24 Strain History at Gage 1 in Long Beam Specimen Using Force History No. 1. 93

4.25 Strain History at Gage 2 in Long Beam Specimen Using Force History No. 1. 94

4.26 Strain History at Gage 1 in Long Beam Specimen Using Force History No. 2. 95

4.27 Strain History at Gage 2 in Long Beam Specimen Using Force History No. 2. 96

4.28 Strain History at Gage 1 in Long Beam Specimen Using Force History No. 3. 97

4.29 Strain History at Gage 2 in Long Beam Specimen Using Force History No. 3. 98

4.30 Strain History at Gage 1 in Long Beam Specimen Using Force History No. 4. 99

4.31 Strain History at Gage 2 in Long Beam Specimen Using Force History No. 4. 100

4.32 Force Amplitude Versus V^2 for Impact on Composite Laminates. 101

4.33 Inverse Contact Time Versus Impact Velocity for Impact on Composite Laminates. 102

4.34 t_{F_o}/T Versus Impact Velocity for Impact on Composite Laminates. 103

4.35 Nodal Force Distribution at a Fixed Instant in Time. 104

5.1 Lamina Reference Axes. 125

5.2 [0/90] Laminate and Reference Axes 126

5.3 Finite Element Discretization of $[90/0]_{5s}$ Graphite/Epoxy Laminate Remote from Crack Tip. 127

5.4 Finite Element Mesh Gradient Near Crack Tip. 128

5.5 Effect of Remote Mesh Refinement on Crack Tip Response of Homogeneous Beam with 1.0 Inch Crack 129

1. INTRODUCTION

Delamination is a mode of failure that is unique to composite laminates. A delamination crack can significantly reduce the compressive strength of a laminate, and can also induce matrix cracking, which will further degrade the structural integrity of the laminate. Delamination can be produced by both static and dynamic loads. Great attention has been given to the problem of free-edge delamination in laminates subjected to in-plane static and fatigue loadings [1-4], and many people have attempted to measure the fracture toughness with respect to delamination cracks [5-9]. Few attempts have been made, however, to measure the dynamic delamination fracture toughness. This is one of the goals of this research.

It is known that material properties often exhibit a strain-rate dependence [10]. In fact, the fracture toughness measured in a static loading test will, in general, be different from that observed under dynamic loading [11, 12]. Use of a statically measured fracture toughness in a dynamic crack propagation analysis can indeed seriously overestimate the crack arrest capability of a structure [13]. In addition, the effective initiation toughness measured under impact loading conditions [14] was found to be roughly twice that measured in static loading tests of high strength steel. The differences between the static and dynamic toughness are due primarily to the fact that the

static calculations cannot account for the return of kinetic energy to the crack tip, and the assumption that the fracture energy is independent of the crack propagation velocity [15]. Early work in crack arrest and dynamic fracture mechanics in general was motivated by brittle fracture commonly observed in the hulls of ships [16, 17]. To determine if the arrest toughness, K_a, was a material characteristic, Hoagland [16] performed experiments on wedge-loaded double-cantilever beam specimens of four different steels. The amount of stored strain energy at the onset of crack propagation was systematically varied from one specimen to another by changing the radius of the starter notch. As the initial notch tip bluntness was increased, the stress intensity at initiation increased, and a resulting decrease in stress intensity at arrest was observed. From these results it was concluded that the "arrest toughness" is not a material constant, but is dependent on the amount of initial strain energy stored in the structure.

An energy balance criterion can account for the return of kinetic energy to the crack tip. Hahn [17] concluded that fast fracture and arrest in a variety of steels are governed by an energy balance criterion, in which the excess energy (G-R) is available to drive the crack tip. When G<R, the kinetic energy contributes significantly to the crack driving force until arrest. In [18] Hahn studied fast fracture in a wedge-loaded double cantilever beam specimen using a beam-on-elastic-foundation model. He showed that there is a unique relationship between the steady-state crack propagation velocity and the crack length at arrest for a given material and specimen geometry.

Indeed, the stress intensity at arrest was found to vary with crack propagation history, and therefore it cannot be considered a material property.

A review of dynamic fracture toughness measurements in polymers is given by Kobayashi [19]. He points out that evidence from experiments on large polymeric specimens [20-22] seems to suggest a unique relation between the dynamic fracture toughness, K_{I_D}, for a propagating crack, and the crack propagation velocity, in polymers. Hodulak [23] tested dynamic fracture specimens of three different geometries to assess the uniqueness of the fracture toughness versus crack velocity relationship. He used a finite element analysis with an experimentally determined K_{I_D} vs. $\dot{a}$ relationship, and calculated the crack propagation history. His results showed that K_{I_D} vs. $\dot{a}$ relation is geometry dependent, and he concluded that dynamic crack propagation is not controlled solely by the instantaneous state surrounding a running crack, but is also significantly affected by the motion of the structure remote from the crack.

In contrast to in-plane static loads, under which delamination often initiates from free edges, impact loading always results in interior delamination near the impact zone. Thus, the delamination mechanism cannot be explained by using the free edge singular stress concept. The strain energy release rate was defined by Erdogan [24]. Several methods of calculating the energy release rate from a numerical analysis have been proposed. Rybicki [25] devised an efficient technique to calculate static Mode I and II energy release rates from a single finite element analysis. He used the near-tip nodal forces and

displacements to calculate the work required to close the crack by an amount Δa, assumed equal to one near-tip element length. It has been shown [26] that this crack closure technique is also valid in the case of dynamic loading, if the finite element mesh near the crack tip is small enough. The first objective of this work is to model the impact of a composite laminate and to determine from this model a critical value of strain energy release rate, G_c, required to cause instability of an existing delamination crack. This parameter, if it exists, may be a characteristic of the material. To model the impact response of the laminate adequately, an accurate representation of the impact force history must be determined. This is the second major objective of this work.

Insofar as the primary concern here is to model the dynamic behavior of the laminate from impact to the initiation of propagation of the delamination crack, no attempt is made to model the propagation of the crack. Therefore, the analysis of the cracked laminates presented here is valid only until the onset of crack propagation in the laminate.

The presentation of this work is organized as follows. Chapter 2 explains the equipment and procedures used to perform the Ballistic Impact experiments. In Chapter 3, the photographic data and the corresponding measurements taken from it are presented. A technique used to characterize the stiffness loss in the delaminated impact specimens is illustrated. Chapter 4 describes how the impact force history was modeled, and how this model was incorporated into the impact analysis of the composite laminate. Chapter 5 is a presentation

and discussion of the results of the impact analysis of the laminates. Chapter 6 is the summary.

2. EXPERIMENTAL APPARATUS AND PROCEDURE FOR IMPACT TESTING

2.1 Impact Specimen Preparation

Impact specimens were cut from 20-ply $[90/0]_{5s}$ T-300/934 graphite/epoxy laminates of dimension 0.105x12x18 in. These laminates were fabricated at the NASA Lewis Research Center in Cleveland, Ohio. A delamination crack was embedded in each laminate by placing a .001x1.0x18 in. strip of Teflon between two plies during the lay-up process. This prevented the two adjacent plies from bonding together in this area. A beam-like geometry was chosen for the impact specimens. Nominal dimensions are shown in Fig. 2.1. Thus, the initial delamination is a 1.0 inch long, through-the-width crack. The location of the embedded crack in both the longitudinal and thickness directions was varied between laminates. This was done to study the effect of crack location on delamination characteristics.

2.2 Ballistic Impact Testing of Composite Specimens

Silicon rubber balls $\frac{1}{4}$ inch in diameter were used as impactors. These relatively soft impactors do not cause significant surface damage near the impact site, thus allowing crack extension to be the primary mode of impact damage. Nitrogen gas was used to fire the impactor through the cannon, shown in Fig. 2.2. A chamber pressure of 20 psi could propel the 1 gram rubber ball at approximately 6000 inches

per second. The impact velocity was determined by two pairs of photo-electric diodes placed on both sides of the path of the impactor near the muzzle of the barrel. A high speed 16 mm FASTAX framing camera was used to record the crack propagation. It was mounted to give an edge-on view of the impact specimen, which was enclosed in a plexiglas box and clamped at one end in a cantilever fashion. The peak framing rate of the camera is 8000 frames per second. This rate is effectively doubled by an internal rotating prism which made two exposures per frame, thus taking 16000 pictures per second. Because of the high exposure rate of the film, very bright light was needed to adequately illuminate the impact specimen. This was provided by three 100-watt floodlights. The firing sequence was initiated from a control panel with timers set to trigger the camera and photo lights just before impact.

The details of this experimental set up are shown in Figs. 2.3 and 2.4

2.3 Measurement of Delamination

To facilitate the measurement of the delamination length from the high speed film, the edge of the impact specimen nearest the camera was painted yellow. This made the advancing crack clearly visible against the light background. In addition, dark stripes were painted at quarter-inch intervals along the edge of the specimens to serve as reference points in measuring the crack length. The Ultrasonic C-Scans of several impacted specimens shown in Fig. 2.5 indicate that the variation in delamination crack length through the width of the specimen is small. The measurements of crack length taken along the

outer edge of the specimen can therefore be assumed to represent the total delaminated area at a given time.

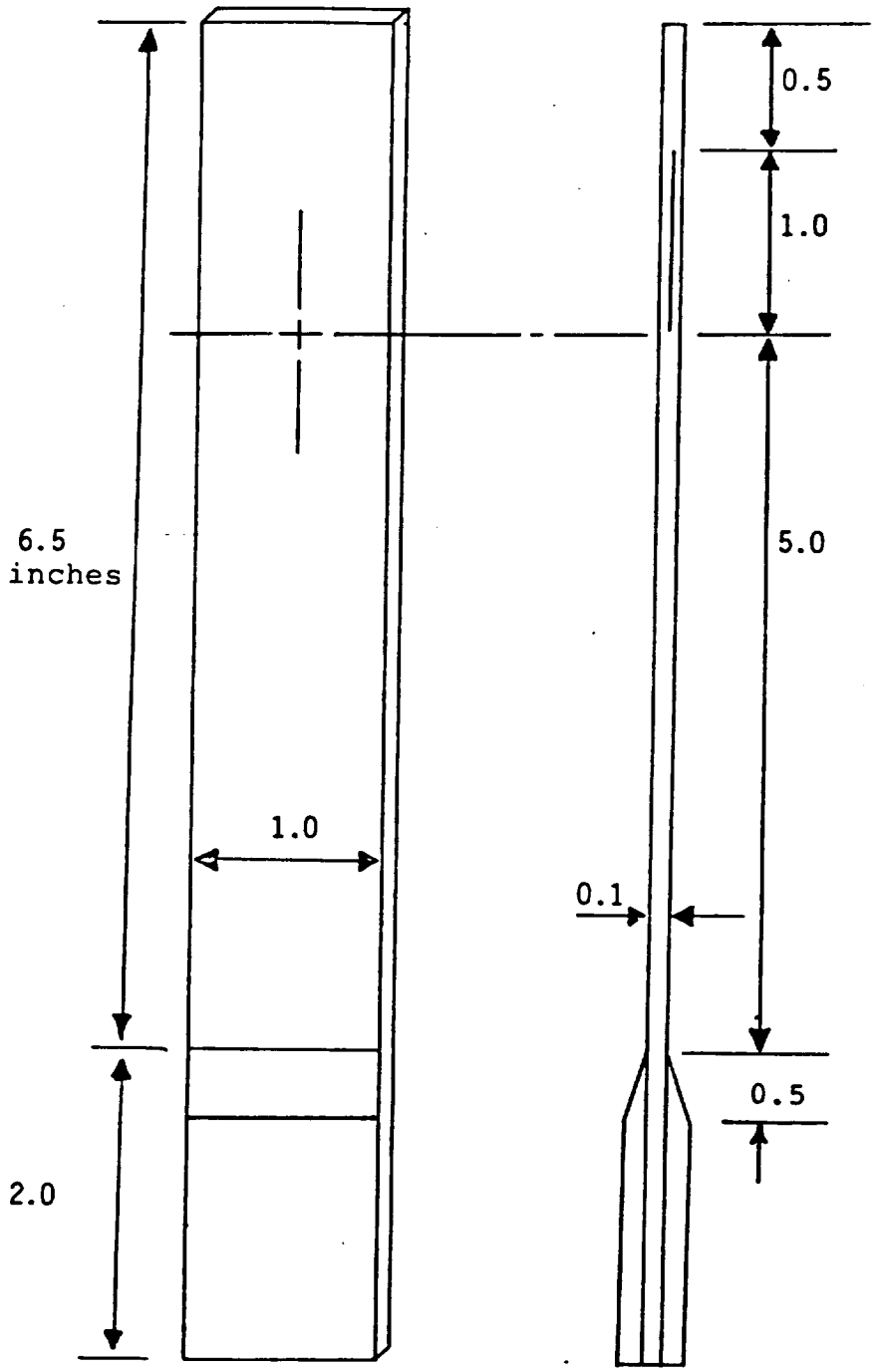

Figure 2.1 Nominal Impact Specimen Dimensions

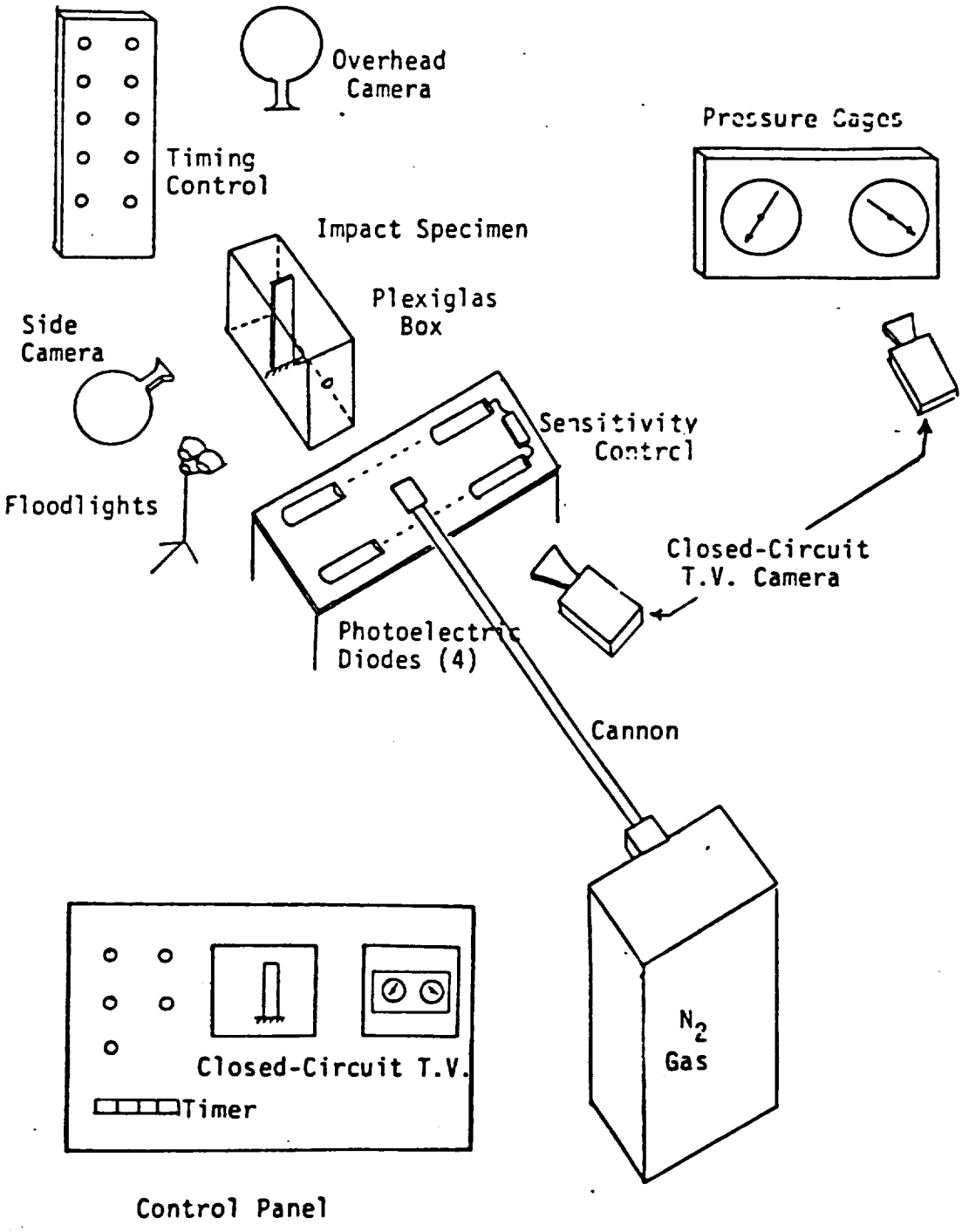

Figure 2.2 Ballistic Impact Experimental Set-Up

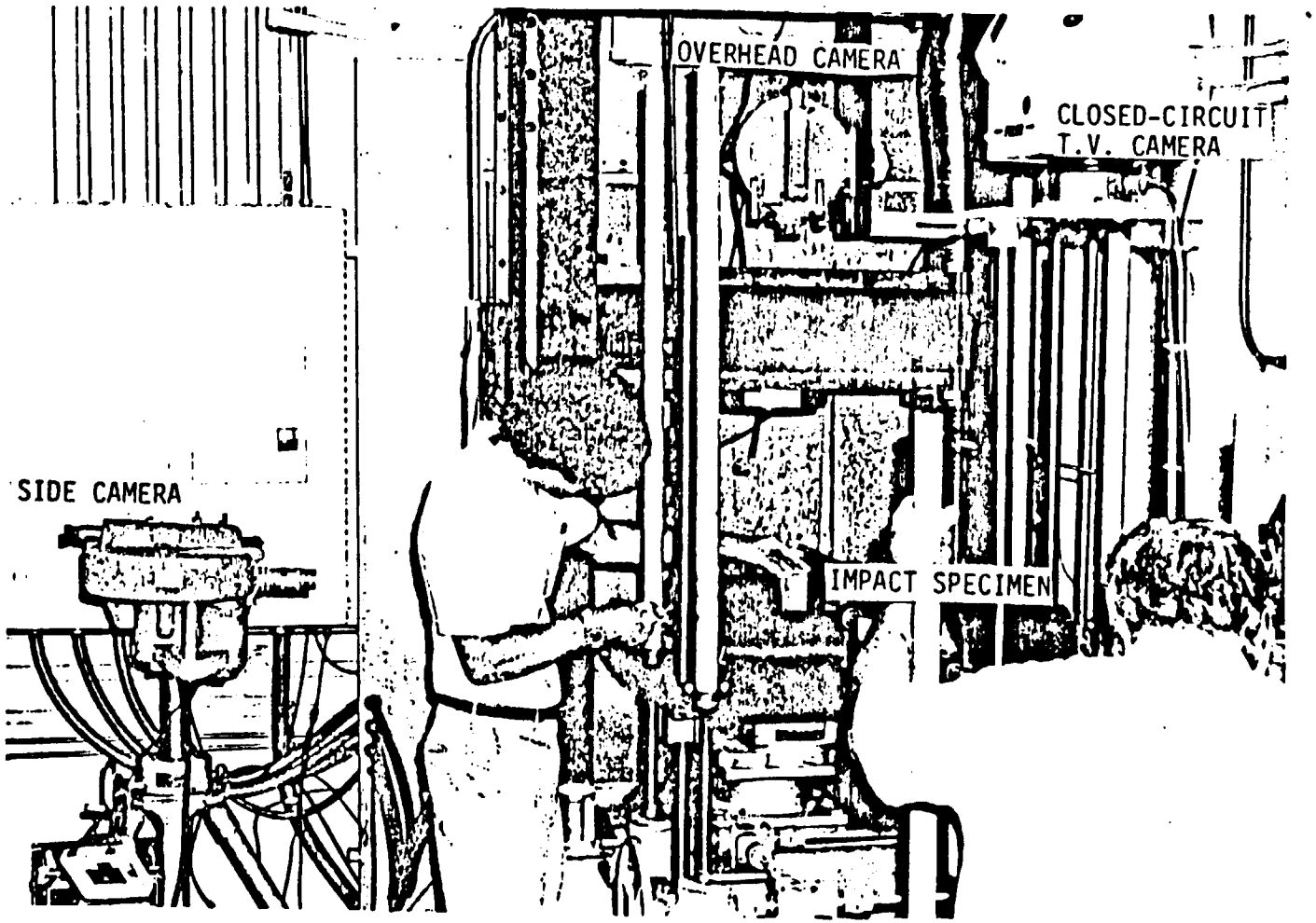

Figure 2.3 Camera Arrangement

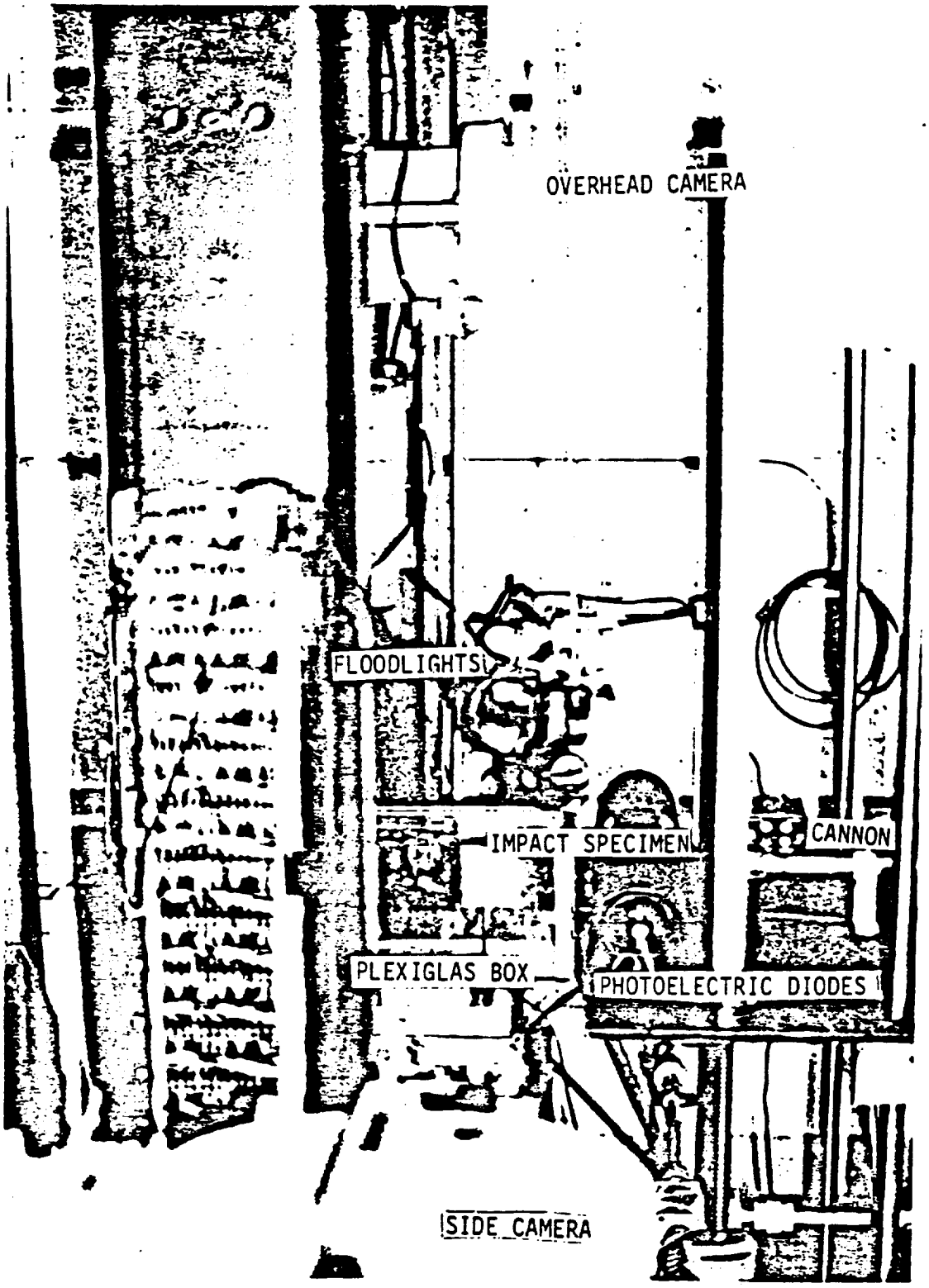

Figure 2.4 Lighting Arrangement

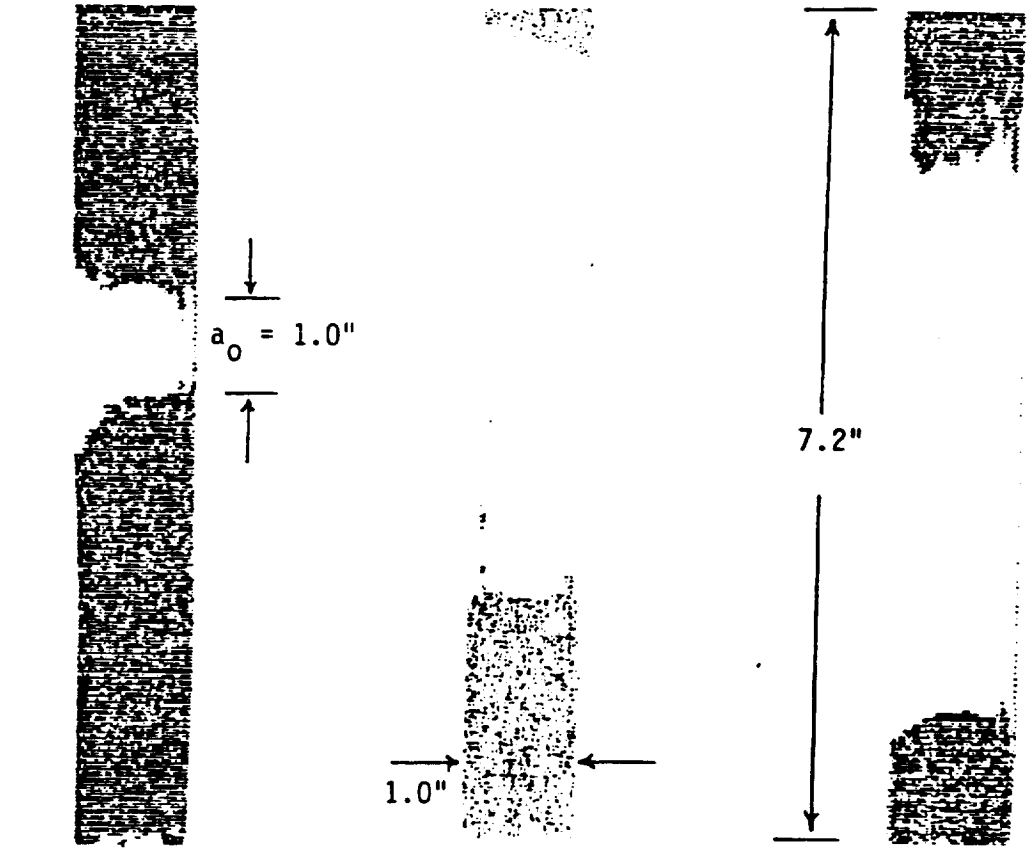

Figure 2.5 Ultrasonic C-Scans of Impacted Specimens

3. IMPACT RESPONSE OF CRACKED LAMINATES - EXPERIMENTAL RESULTS

3.1 Threshold Impact Velocity

The dependence of delamination damage on impact velocity is of primary interest. In this study, attention will be focused on the threshold velocity at which the embedded crack becomes unstable.

Figure 3.1 shows the geometry of eight different specimen configurations tested. The location of the impact point varied slightly between specimens due to small variations in alignment of the gun barrel. The extent of this variation, along with the relation between impact velocity and total delaminated area for each of the specimen configurations tested is shown in Tables 3.1-3.7 and in Figs. 3.2-3.7. Each specimen contains an initial (embedded) delamination. In most cases, the existence of an unambiguous threshold velocity is quite evident. Threshold velocities for specimen configurations A-H were determined from Figs. 3.2-3.7. Insufficient data was available for specimen configurations F and G so corresponding threshold velocity plots are not shown for these configurations. Among the three thickness locations tested, threshold velocity is greatest for the mid-plane crack (Table 3.2, Fig. 3.3) and lowest for the lower off-midplane crack (Table 3.3, Fig. 3.4). The results show that when impacted near the crack tip, the delamination crack becomes unstable

at lower velocities. Tables 3.4 and 3.5 show that this phenomenon is more pronounced for cracks located near the top (impact) surface. This behavior may be a result of the unsymmetrical distribution of shear stress over the cross section of the laminate which occurs near the point of impact. Joshi [27] showed that the maximum shear stress occurs near the impacted side of the laminate cross section during and shortly after the contact interval. This would suggest that the onset of crack propagation in specimens of the geometry shown in configuration D of Fig. 3.1 is dominated by a shearing (Mode II) rather than an opening (Mode I) action.

3.2 Dynamic Crack Propagation

3.2.1 Midplane Delamination

A typical impact sequence is shown in Fig. 3.7. Characteristics such as duration of contact period and beam displacement response can be estimated from the figure. It should be noted that all measurements were taken from larger images projected on a movie screen. The figures shown here are primarily for illustration. In this case, the embedded crack lies along the specimen midplane and directly under the impact site, as shown in the figure. The resulting crack propagation is shown in Fig. 3.8. The crack arrest ($438 < t < 688\mu s$) is apparently due to the nature of strain response near the propagating crack tip. A decrease in local curvature of the beam is accompanied by a decrease in available crack driving force. This correspondence is shown in frames 9-11 of Fig. 3.7. Frames 12-14 ($688 < t < 813\mu s$) show the subsequent increase in curvature, and the corresponding resumption of crack propagation.

Apparently, the geometry of the impact specimen can significantly affect the crack propagation. Strain (curvature) will be affected by the arrival of flexural wave reflections from the boundaries, so the position of the crack relative to the boundaries will affect crack propagation. The time delay between impact and initial crack propagation observed in Figs. 3.7 and 3.8 is a result of the impact occurring directly on the embedded crack. The distributed compression on the crack faces caused by the deforming impactor ($63 < t < 375\mu s$, Fig. 3.7) prevents any crack propagation from occuring during the contact interval. Now, if the embedded crack is moved sufficiently away from the impact site, as depicted in Figs. 3.9 and 3.10, the interference of the impactor with crack propagation should be minimized. Compare Figs. 3.7 and 3.8 with Fig. 3.9. All three figures show similar crack arrest characteristics as the reflections arrive. However, Figs. 3.9 and 3.10 show a significant difference in time between impact and onset of crack propagation.

Impact specimens with different initial crack lengths were tested in order to assess the uniqueness of G_c, the critical strain energy release rate, as the initial crack length was varied. Figs. 3.11 and 3.12 show the impact response of a specimen with a 0.5 inch initial delamination, and the measurements taken of the resulting crack extension. Similar data for a specimen with a 2.0 inch initial delamination are shown in Figs. 3.13 and 3.14. In both cases, the impact velocity is very close to the threshold velocity required to cause crack extension in specimens of that particular geometry. Accordingly, significant variations in the threshold velocity from

that determined for the configuration with a 1.0 inch long initial delamination (Fig. 3.3) are noted. It would be expected, based on elementary fracture mechanics, that the impact velocity required to initiate crack propagation in a laminate would decrease as the length of the initial crack is increased. This trend is reflected in the values of threshold velocity for the specimens with 0.5, 1.0, and 2.0 inch initial delaminations. The effect of initial crack length on G_c is yet to be established, however.

A comparison of the dynamic strain energy release rate prior to crack extension in specimens with 0.5, 1.0, and 2.0 inch initial delaminations should indicate if G_c is independent of the initial crack length. G_c may be characteristic of the material, analogous to the fracture toughness in static loading. An analysis of these three cases is presented in Chapter 5.

3.2.2 Off-Midplane Delamination

All of the cases discussed so far involved delamination along the midplane of the beam. If the embedded crack is placed at a different through-the-thickness location, different crack propagation characteristics are observed. In the following impact specimens, the embedded crack is halfway between the beam midplane and outer surface. Thus, five plies are on one side of the crack and fifteen on the other. For these specimens, the camera was oriented to record the propagation of both crack tips simultaneously, instead of only a single crack tip, as in the previous cases.

Some distinctly different features of crack propagation in this case can be seen from the photographs in Figs. 3.15 and 3.17.

"Buckling" of the delaminated plies is seen to occur at 125, 813 and 875 μs in Fig. 3.15 and at 63, 813 and 875 μs in Fig. 3.17. The photographs suggest, then, that the primary mode of crack extension in this case involves more Mode I (opening) than Mode II (shearing) type of action. The delamination buckling phenomenon has been noted in numerous other applications involving static, dynamic, and fatigue loading [28-35].

Tables 3.2 and 3.3 show that considerably greater impact energy is required to initiate crack propagation when the embedded crack lies along the midplane. The fact that no crack opening similar to that shown for off-midplane cracks is seen for midplane cracks (Figs. 3.7 and 3.9) suggests that considerably less Mode I action is involved when the crack lies on the midplane.

The intermittent nature of the delamination process is illustrated in Figs. 3.16 and 3.18 after the onset of crack propagation has occurred. Flexural wave propagation through the delaminated plies causes them to exhibit a beam-like dynamic behavior independent of the gross deformation of the specimen. Reflection of the waves between crack tips causes alternating propagation-arrest of the crack tips similar to that shown in Fig. 3.18 and to a lesser extent in Fig. 3.16.

3.3 Stiffness Loss Due to Delamination

Because the natural frequencies of a structure are dependent on its stiffness, a decrease in stiffness such as that caused by delamination should cause a corresponding decrease in the natural frequencies. To investigate this effect, the first five natural frequencies of a series of midplane-cracked specimens with geometry similar to

Configuration B in Fig. 3.1 were determined with the apparatus shown in Fig. 3.19 before and after they were impacted.

A sinusoidally time varying force was applied to the free end of the cantilevered specimens by means of a small magnet of negligible mass which was glued to the free end of the specimen, and a stationary magnetic exciter connected to a wave form generator. A Hewlett-Packard HP-141T Spectrum Analyzer slowly varied the forcing frequency of the wave form generator. This created a sinusoidally time varying magnetic field that was used to apply the harmonic force to the specimen through the magnet attached to its free end. A microphone was used to measure the magnitude of the output response (the motion of the specimen) accoustically. This was displayed graphically on the Spectrum Analyzer versus the input frequency. A dual trace oscilliscope was used to display the frequency and magnitude of both the input and output graphically.

The ultrasonic C-Scans of several typical impacted specimens shown in Fig. 2.5 indicate that the variation of crack length through the width of the specimen is small. Therefore, a two dimensional finite element analysis, which will necessarily assume a uniform through-the-width crack, should accurately predict the vibration characteristics of the damaged specimens. Four-node isoparametric plane-strain finite elements [36] were used to model the damaged and undamaged specimens. Figures 3.20-3.24 compare the measured and calculated results for the variation in the first five bending frequencies as a function of crack area. These results indicate that two dimensional elements can accurately model the low vibration modes

of both damaged and undamaged specimens of this geometry. In addition, the results seem to show that the higher frequencies are progressively more sensitive to delamination damage.

TABLE 3.1 Variation of Delaminated Area with Impact Velocity for Specimen Configuration A

Specimen	Impact Velocity, Vo (in/s)	Impact Distance, b (in)	Delaminated Area, A (in^2)*
A1	4803	5.76	1.00
A2	5118	5.66	1.00
A3	5433	5.79	1.00
A4	5591	5.70	1.97
A5	5827	5.89	1.40
A6	5827	6.01	1.00
A7	6141	6.01	2.90
A8	6811	5.98	3.56

*initial delaminated area is 1.00 in^2

TABLE 3.2 Variation of Delaminated Area with Impact Velocity for Specimen Configuration B

Specimen	Impact Velocity, Vo (in/s)	Impact Distance, b (in)	Delaminated Area, A (in^2)*
B1	5630	5.89	1.00
B2	5669	5.97	1.00
B3	5826	5.95	1.37
B4	5826	5.53	1.00
B5	5906	5.78	2.95
B6	6120	5.58	6.50
B7	6141	5.78	3.77
B8	6220	5.63	6.29
B9	6299	5.19	6.00
B10	6338	5.90	6.94

*initial delaminated area is 1.00 in^2

TABLE 3.3 Variation of Delaminated Area with Impact Velocity for Specimen Configuration C

Specimen	Impact Velocity, Vo (in/s)	Impact Distance, b (in)	Delaminated Area, A (in^2)*
C1	4764	5.75	1.82
C2	5433	5.85	2.59
C3	5551	5.86	2.40
C4	5591	5.85	2.06
C5	5669	5.56	4.07
C6	5669	5.76	3.35
C7	5945	5.41	3.95
C8	5945	5.59	4.67

*initial delaminated area is 1.00 in^2

TABLE 3.4 Variation of Delaminated Area with Impact Velocity for Specimen Configuration D

Specimen	Impact Velocity, Vo (in/s)	Impact Distance, b (in)	Delaminated Area, A (in^2)*
D1	3032	5.46	1.00
D2	4016	5.71	1.00
D3	4055	5.72	1.00
D4	4370	5.96	2.31
D5	4724	5.63	2.40
D6	5236	5.63	3.89
D7	5551	5.78	3.83

*initial delaminated area is 1.00 in^2

TABLE 3.5 Variation of Delaminated Area with Impact Velocity for Specimen Configuration E

Specimen	Impact Velocity, Vo (in/s)	Impact Distance, b (in)	Delaminated Area, A (in^2)*
E1	4803	5.59	1.00
E2	5315	5.68	1.00
E3	5551	5.62	1.00
E4	5569	5.61	1.00
E5	5709	5.67	1.65
E6	5827	5.59	2.02
E7	5866	5.66	1.52
E8	6220	5.60	6.50
E9	6378	5.78	2.98

*initial delaminated area is 1.00 in^2

TABLE 3.6 Variation of Delaminated Area with Impact Velocity for Specimen Configuration F

Specimen	Impact Velocity, Vo (in/s)	Impact Distance, b (in)	Delaminated Area, A (in^2)*
F1	4724	5.81	1.00
F2	4803	5.55	1.00
F3	5000	5.98	1.00
F4	5433	5.73	4.17†
F5	5512	5.89	1.00
F6	5591	5.36	4.05†

*initial delaminated area is 1.00 in^2

†transverse cracking caused extensive spalling on back surface

TABLE 3.7 Variation of Delaminated Area with Impact Velocity for Specimen Configuration H

Specimen	Impact Velocity, V_o (in/s)	Impact Distance, b (in)	Delaminated Area, A (in^2)*
H1	4848	7.69	2.00
H2	5364	7.63	2.00
H3	5445	7.63	2.00
H4	5445	8.00	6.88
H5	6012	7.50	2.00
H6	6252	7.88	2.13
H7	7500	7.88	7.88
H8	7632	7.50	7.88
H9	7716	7.63	7.88
H10	7716	7.75	7.88
H11	7728	7.31	7.88

* initial delaminated area is 2.00 in^2

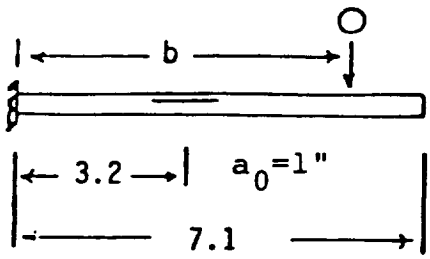

A

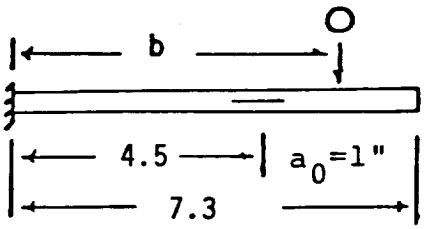

B

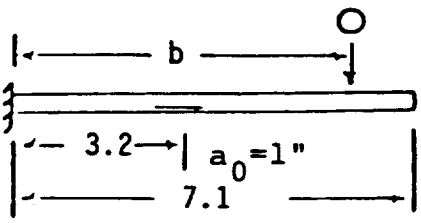

C

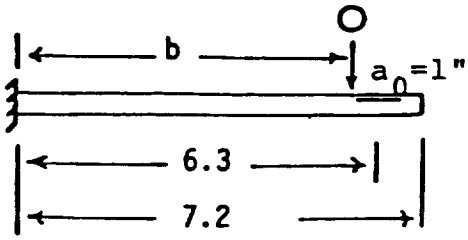

D

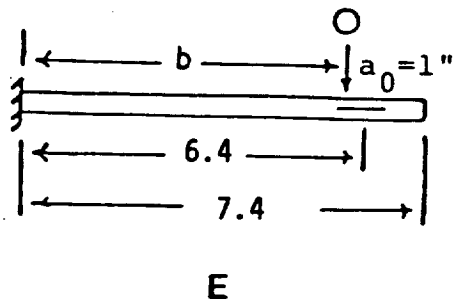

E

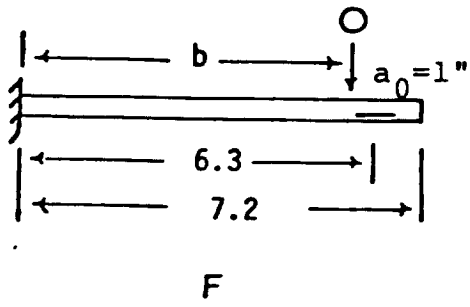

F

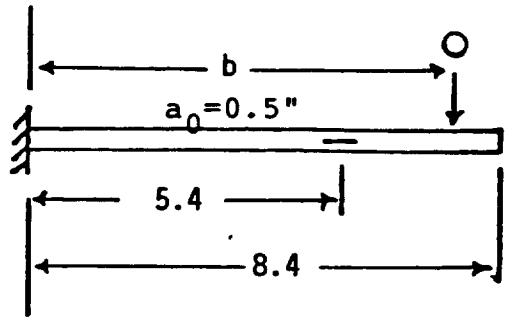

G

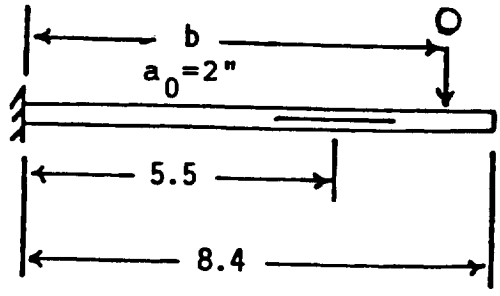

H

Figure 3.1 Impact Specimen Configurations

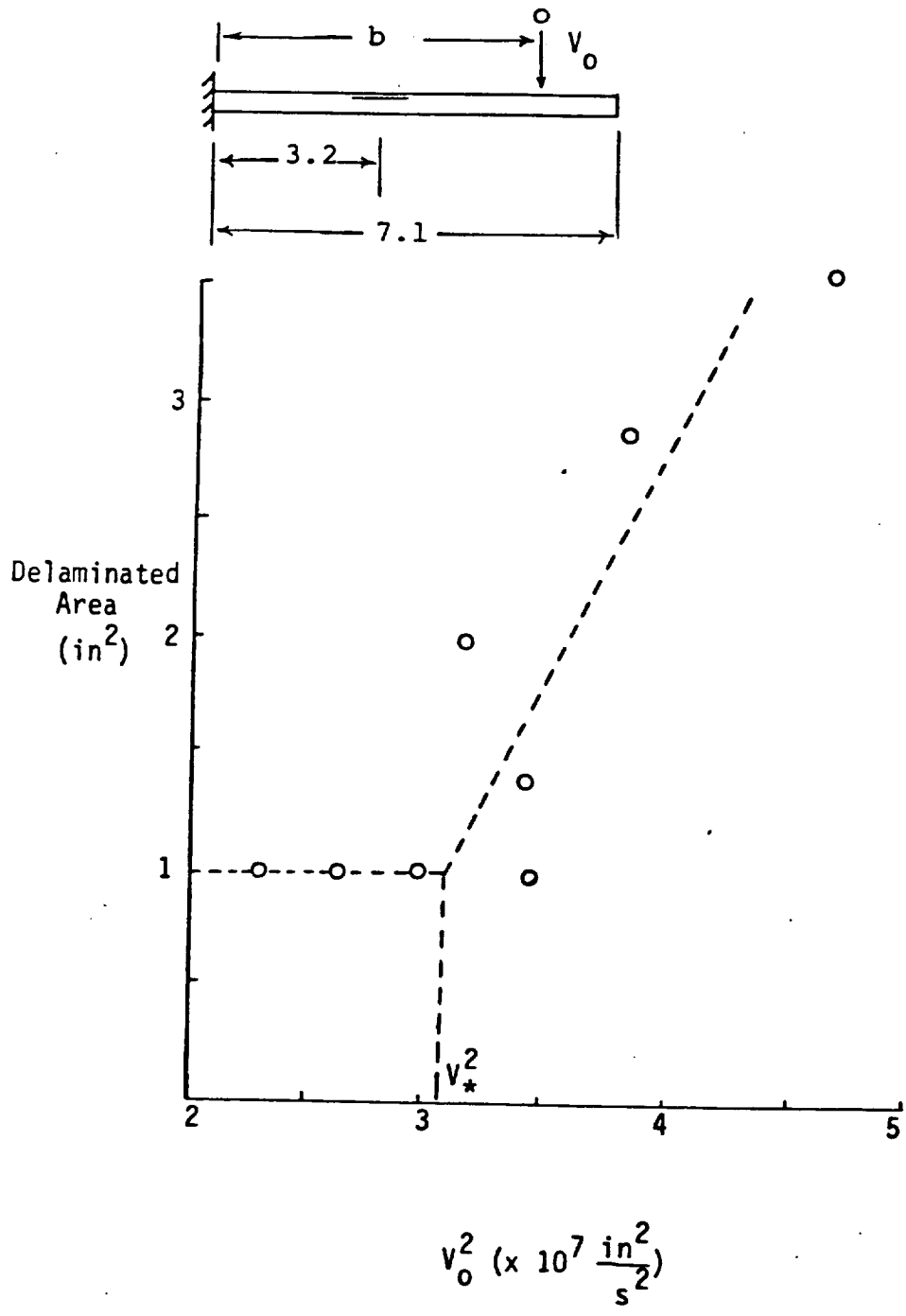

Figure 3.2 Delaminated Area Versus Impact Energy for Specimen Configuration A

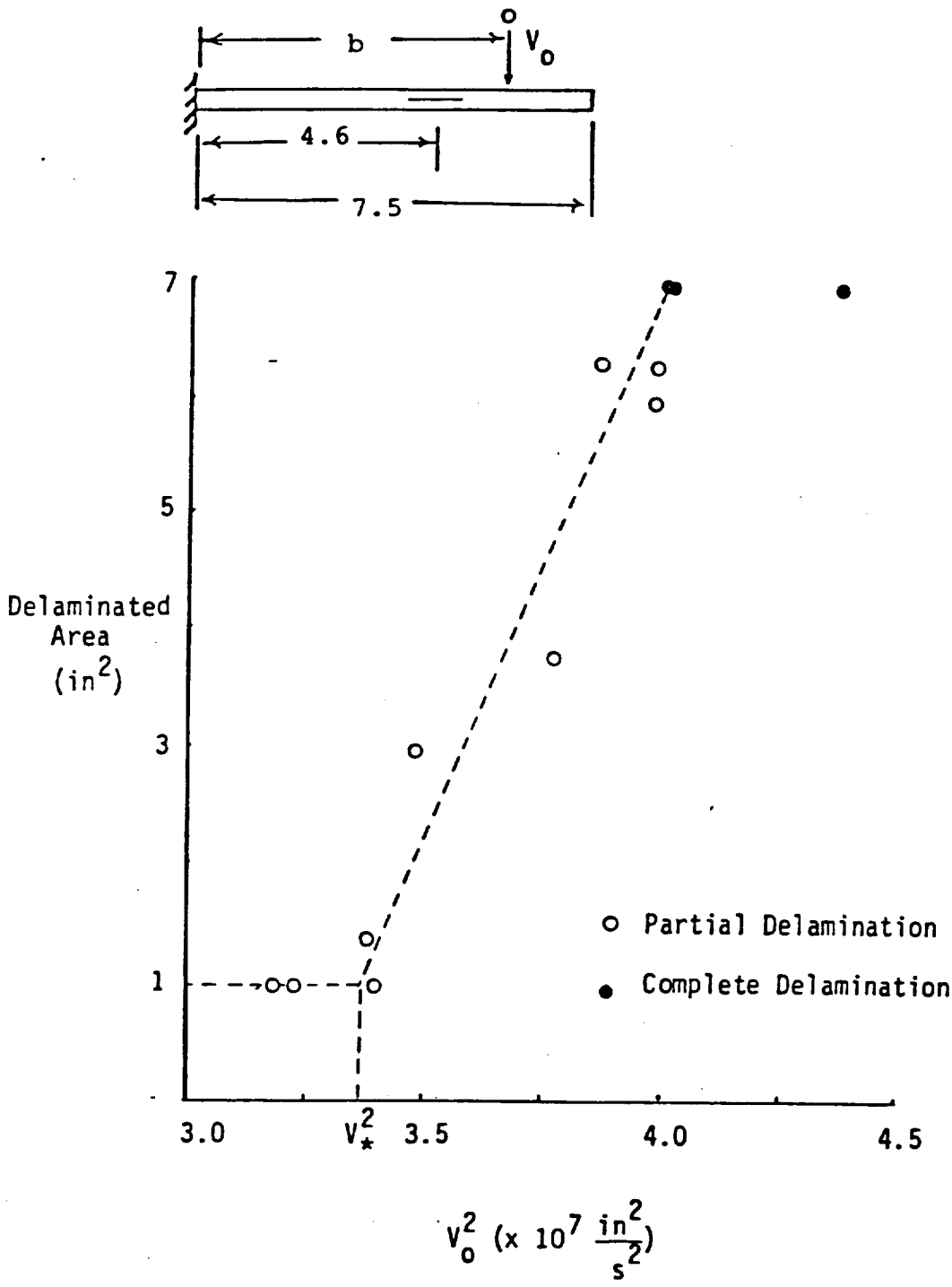

Figure 3.3 Delaminated Area Versus Impact Energy for Specimen Configuration B

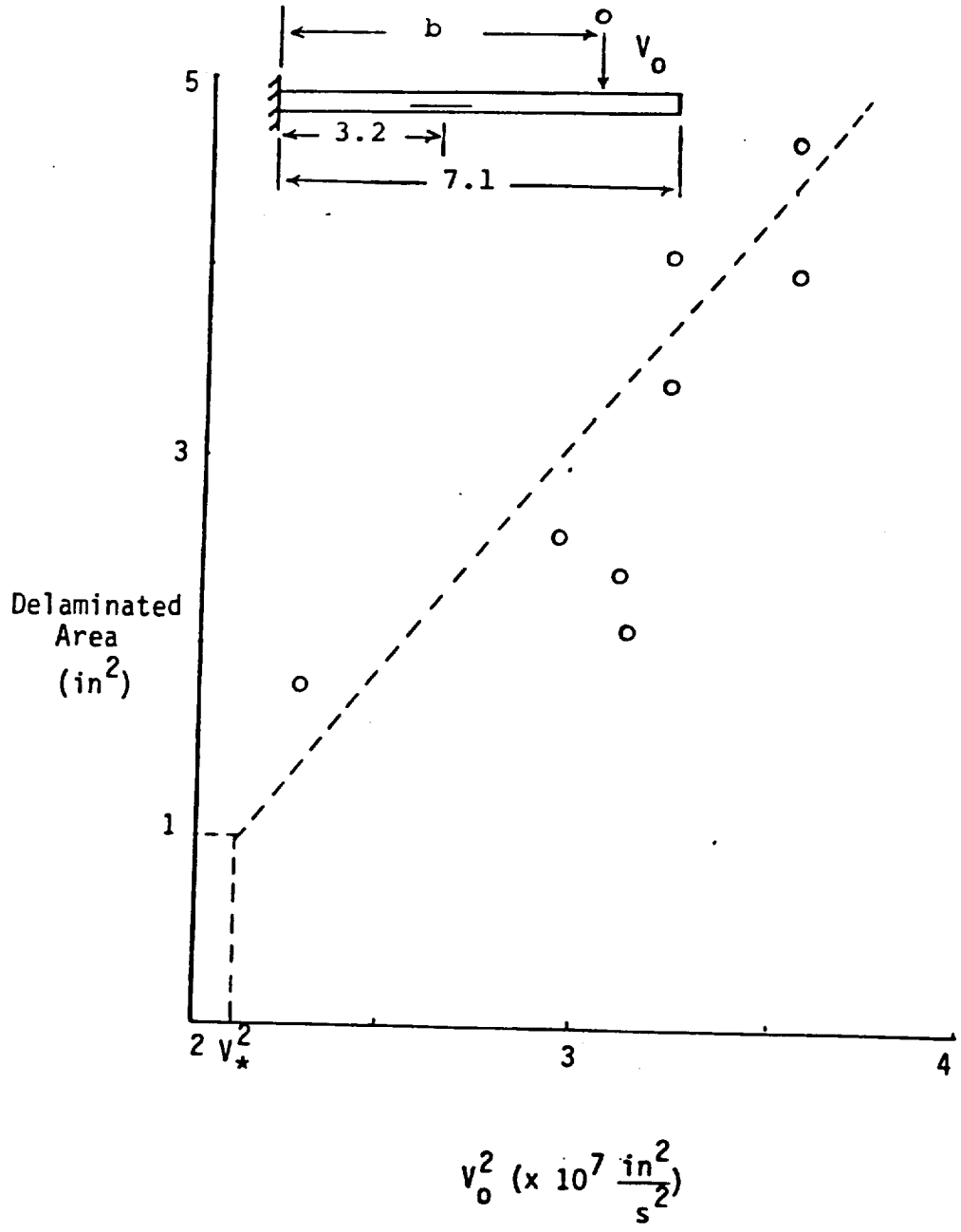

Figure 3.4 Delaminated Area Versus Impact Energy for Specimen Configuration C

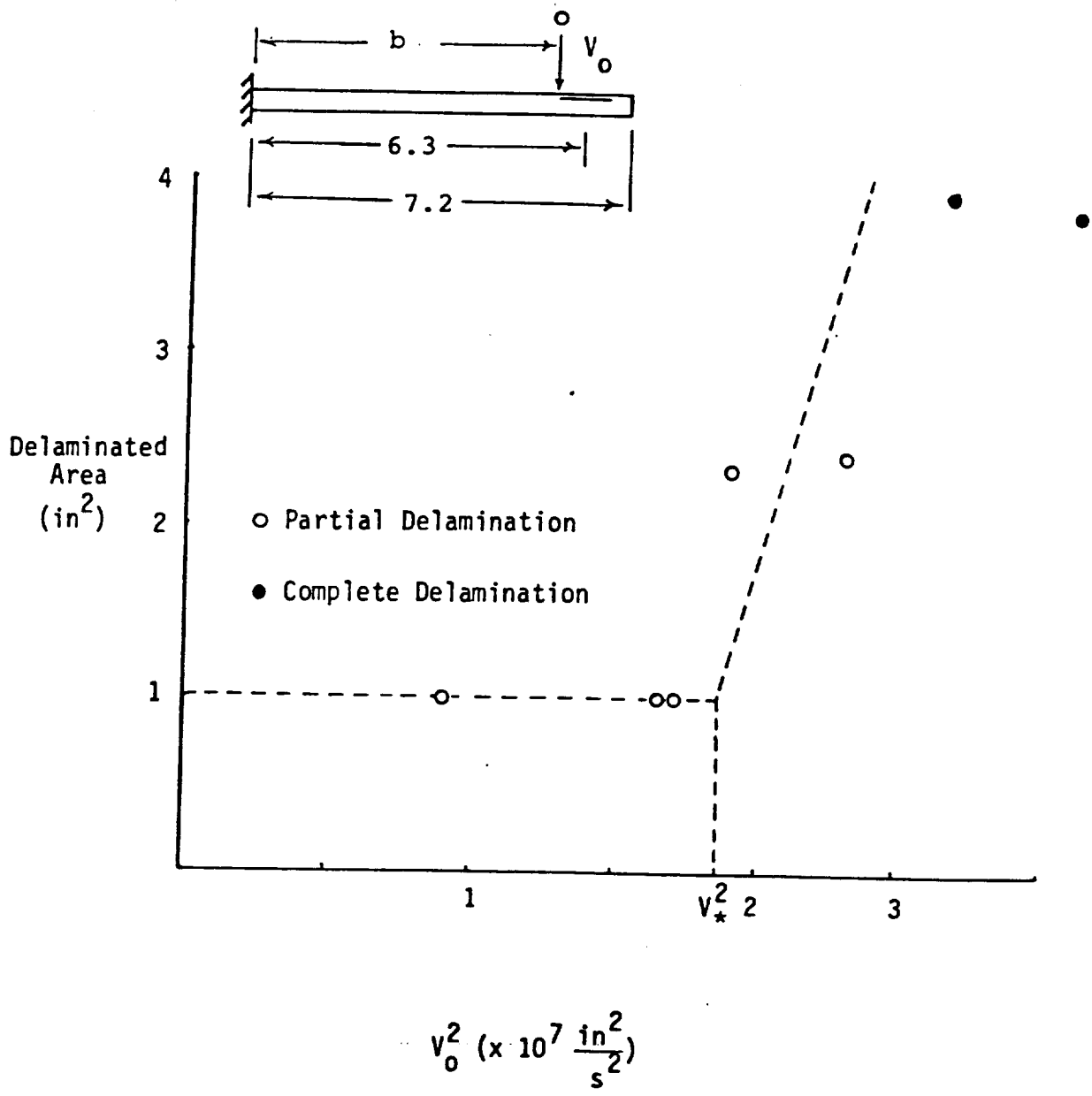

Figure 3.5 Delaminated Area Versus Impact Energy for Specimen Configuration D

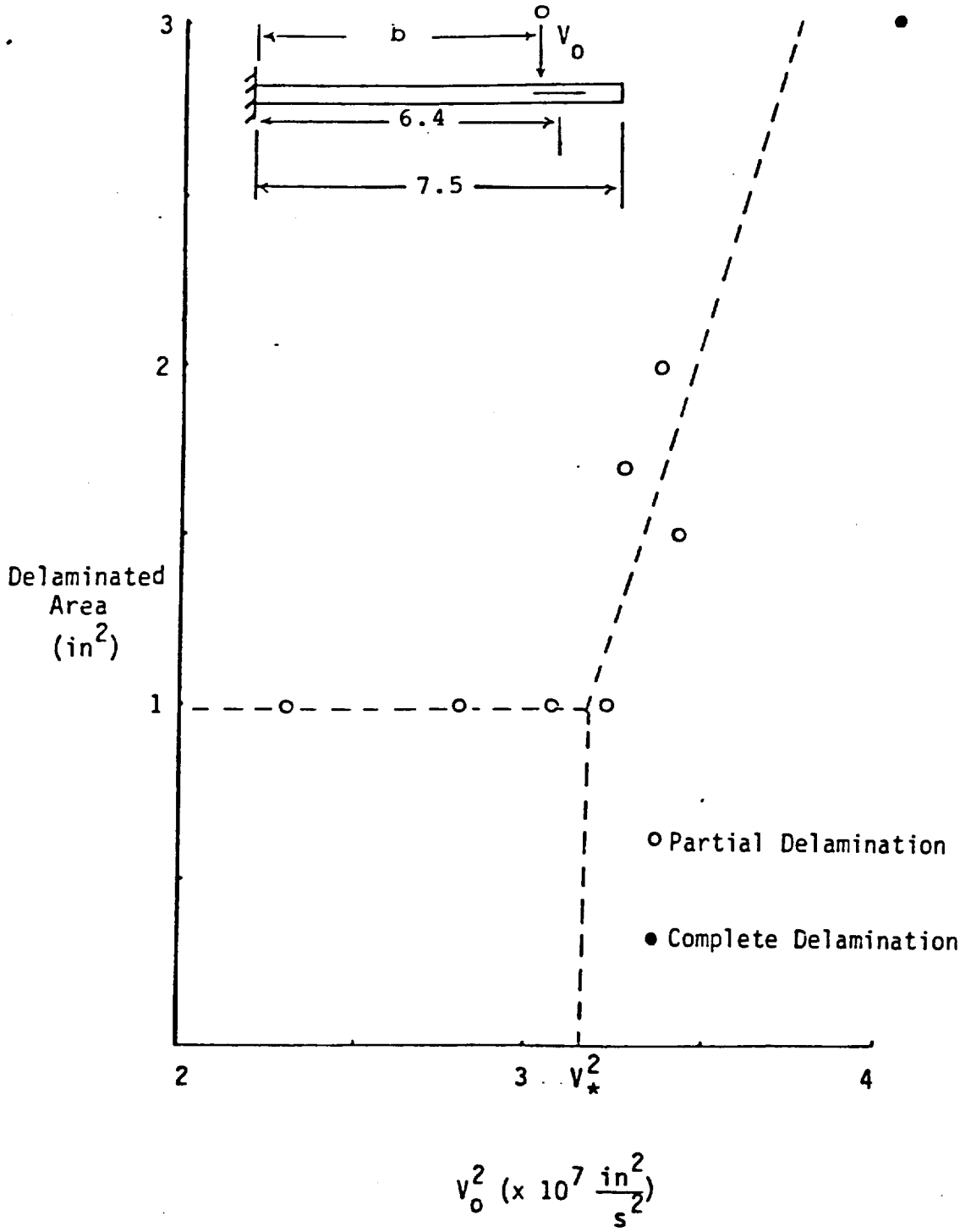

Figure 3.6 Delaminated Area Versus Impact Energy for Specimen Configuration E

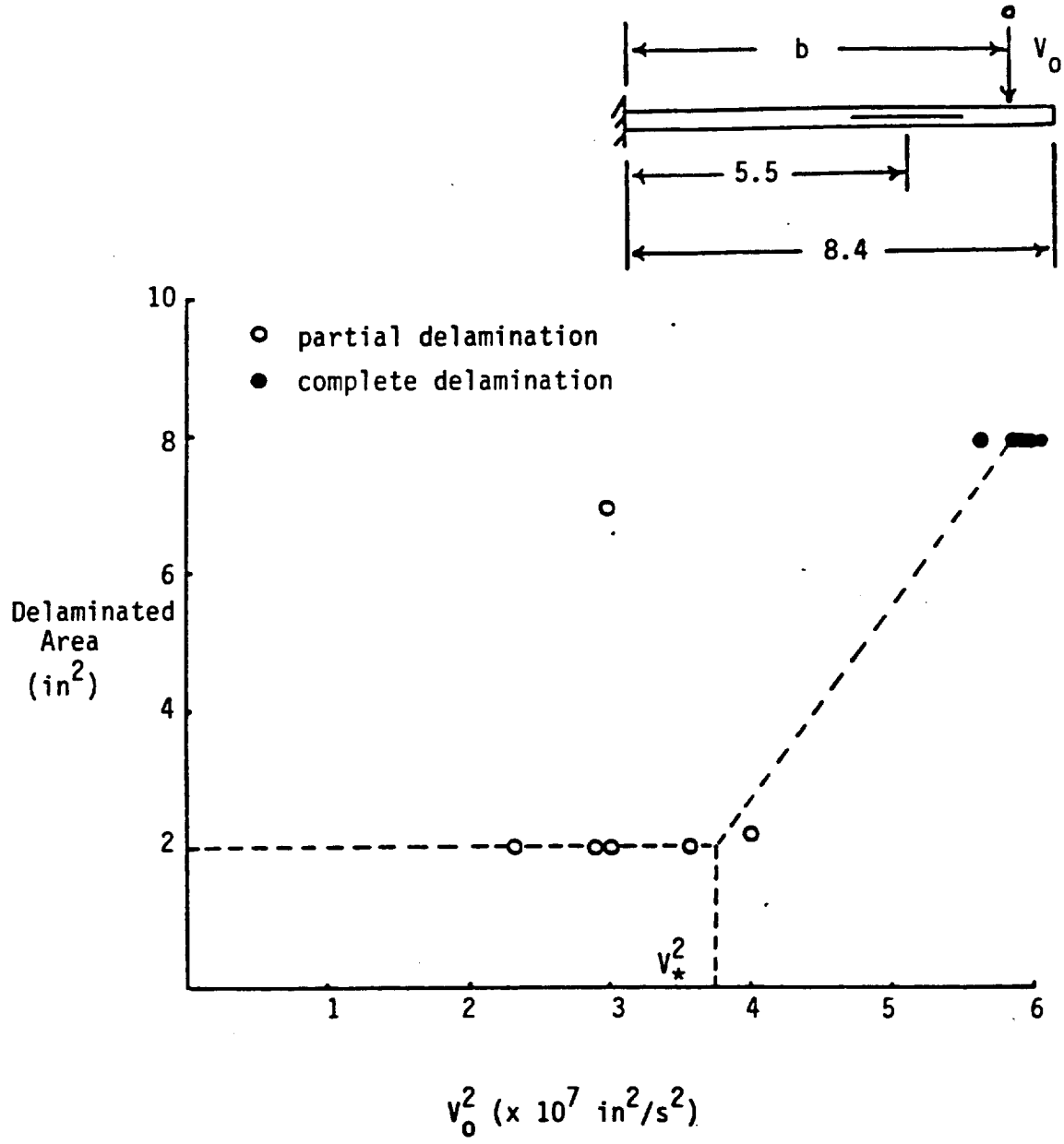

Figure 3.7 Delaminated Area Versus Impact Energy for Specimen Configuration H

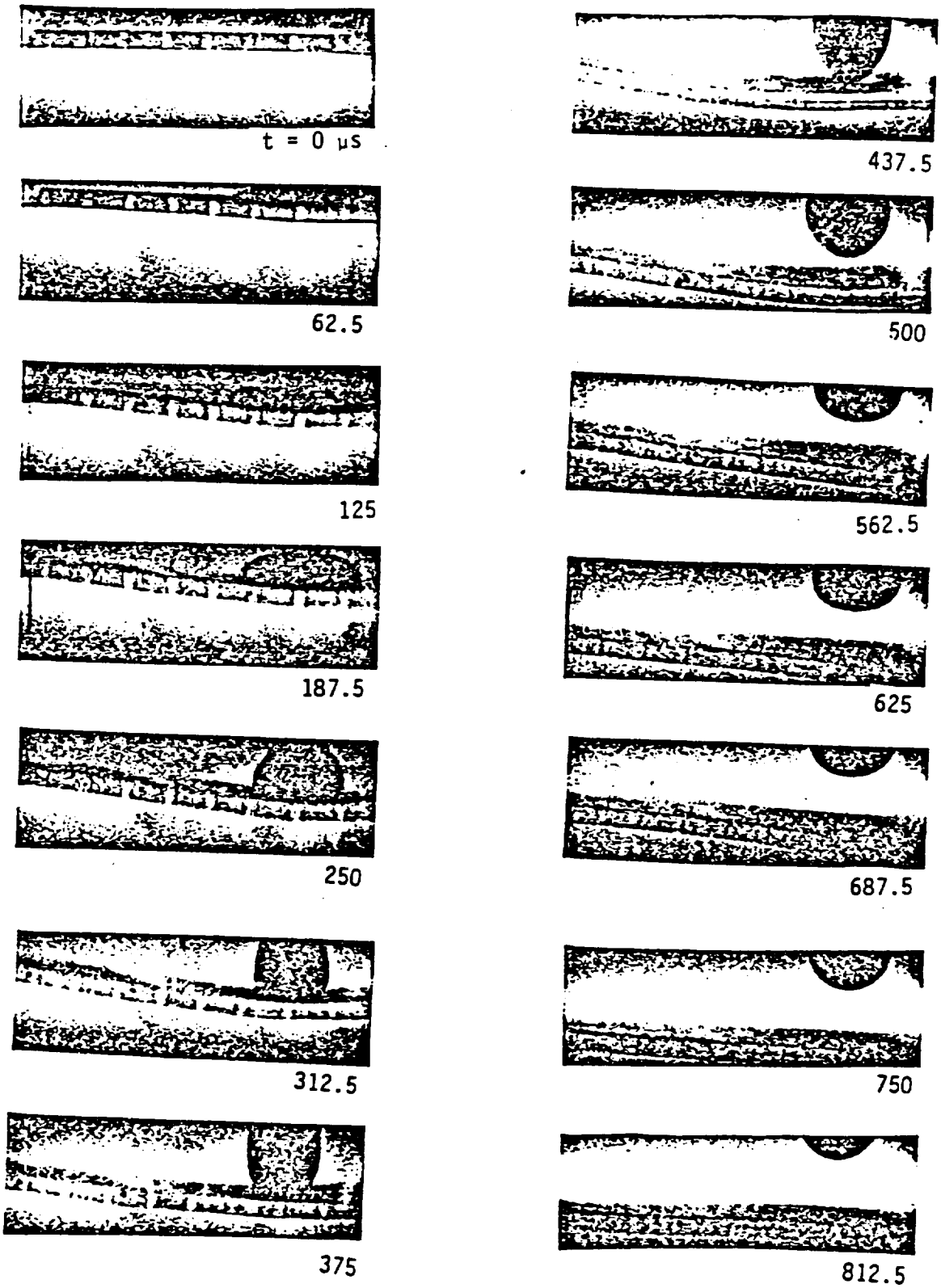

Figure 3.8 Impact Response of Specimen ES

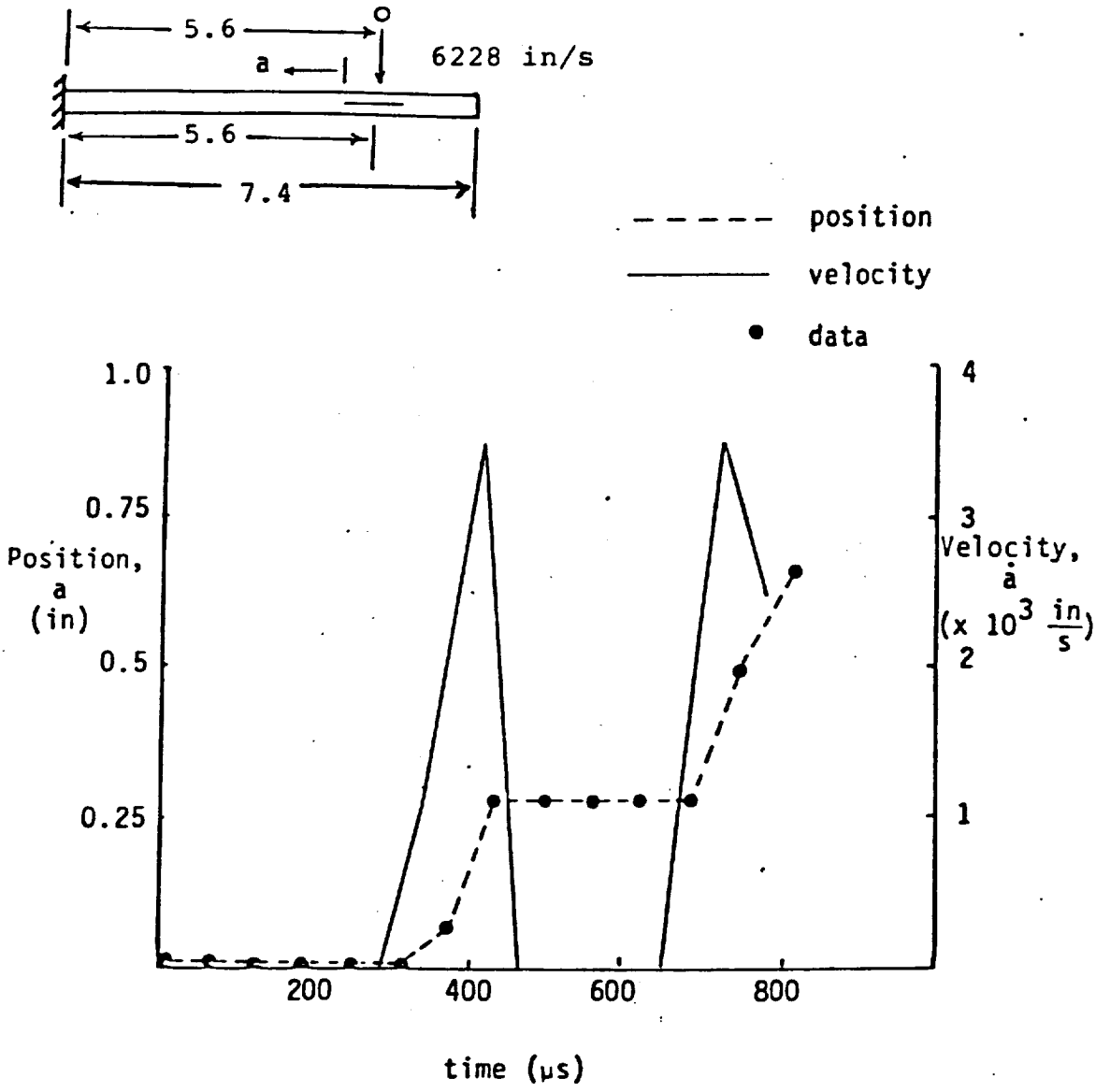

Figure 3.9 Crack Propagation History in Specimen E8

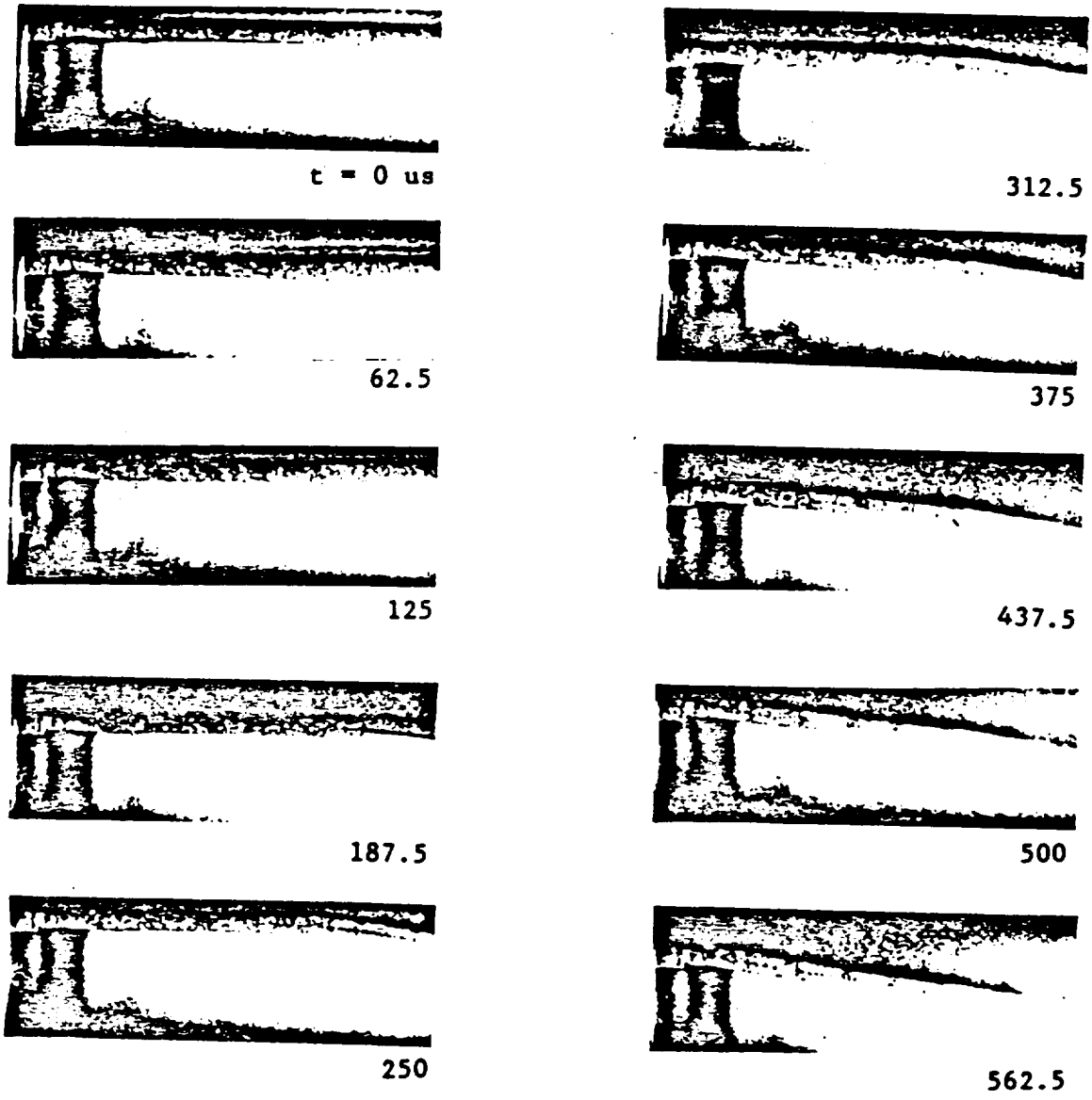

Figure 3.10 Impact Response of Specimen B6

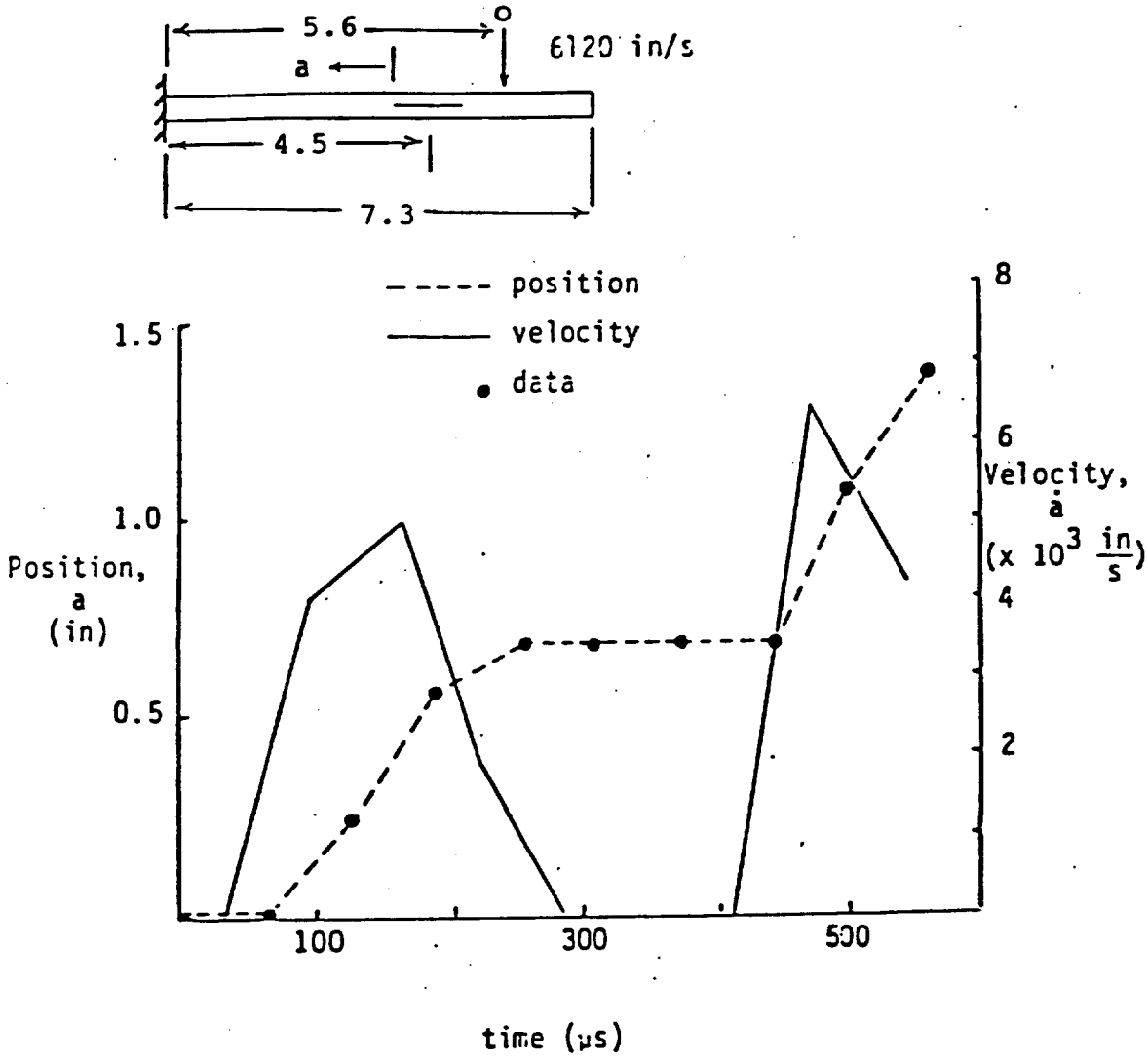

Figure 3.11 Crack Propagation History in Specimen B6

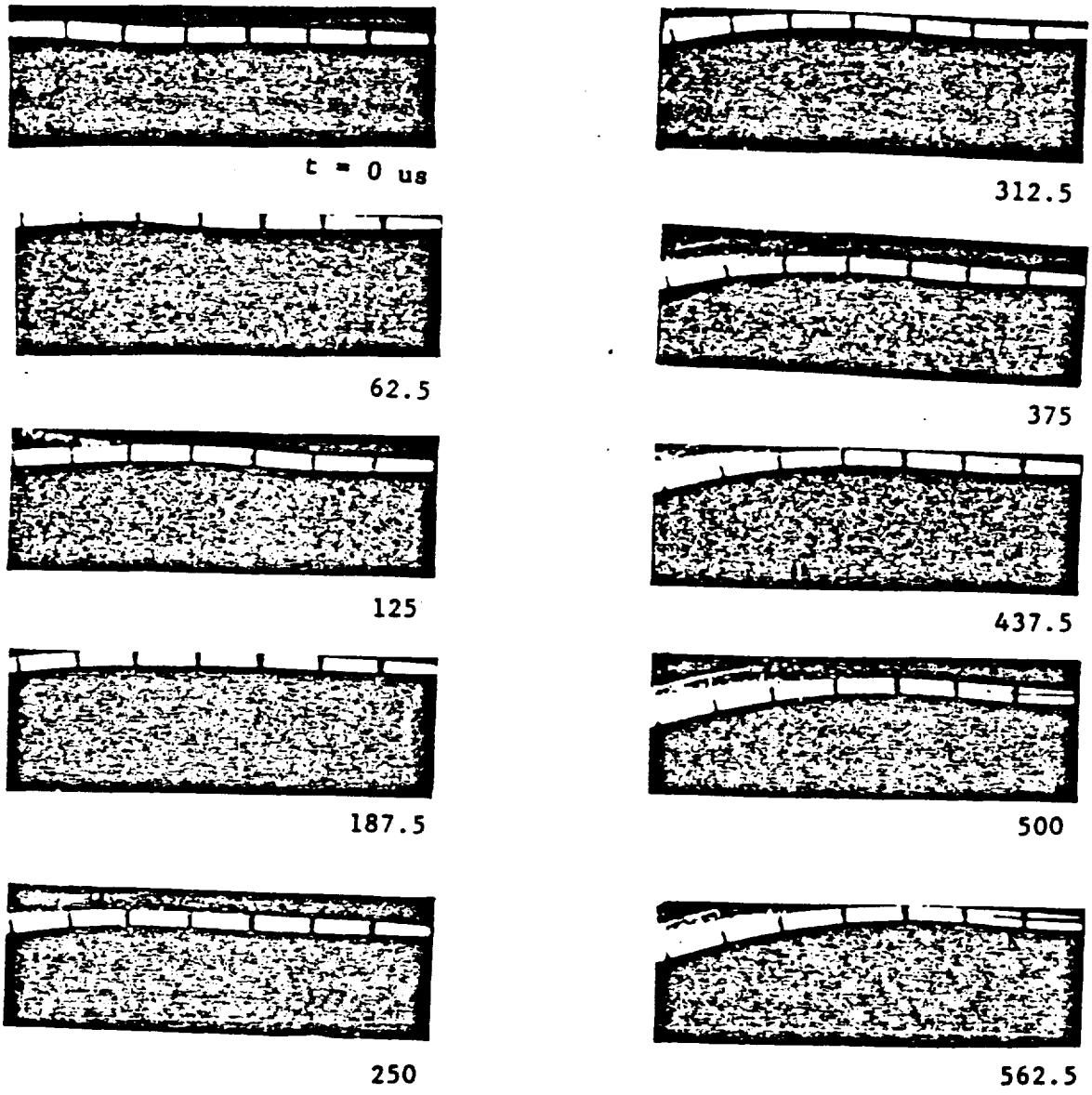

Figure 3.12 Impact Response of Specimen G1

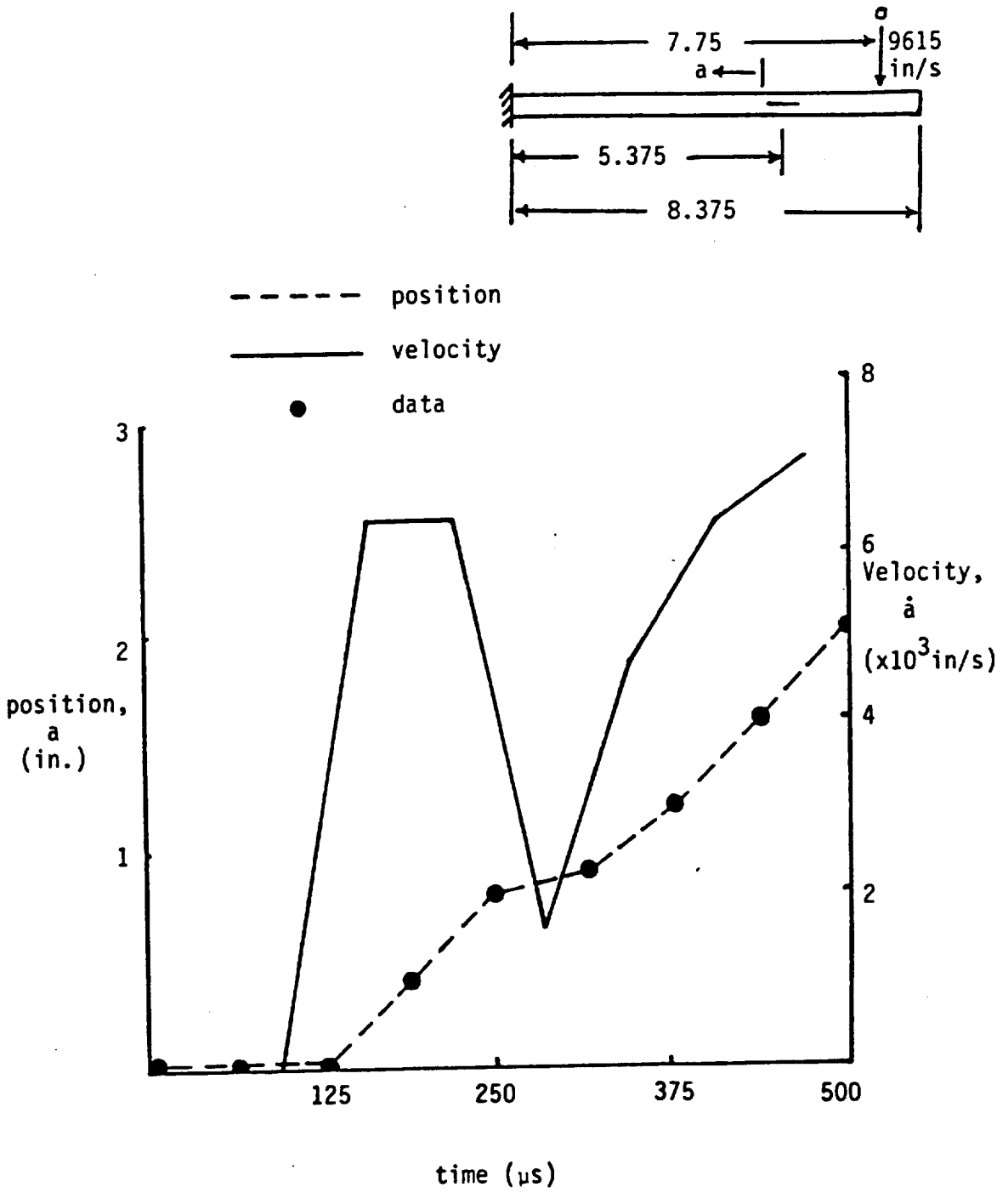

Figure 3.13 Crack Propagation History in Specimen G1

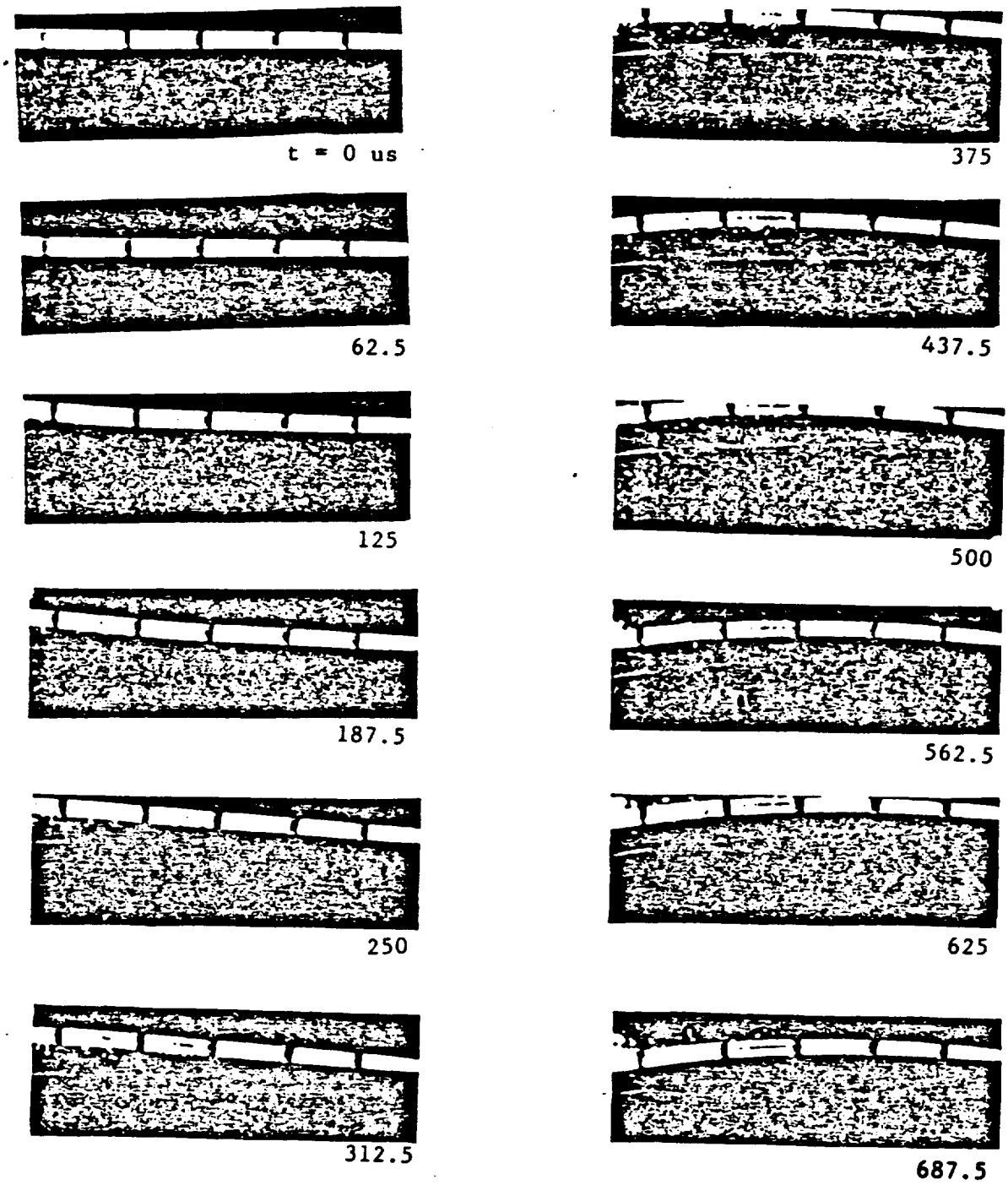

Figure 3.14 Impact Response of Specimen H4

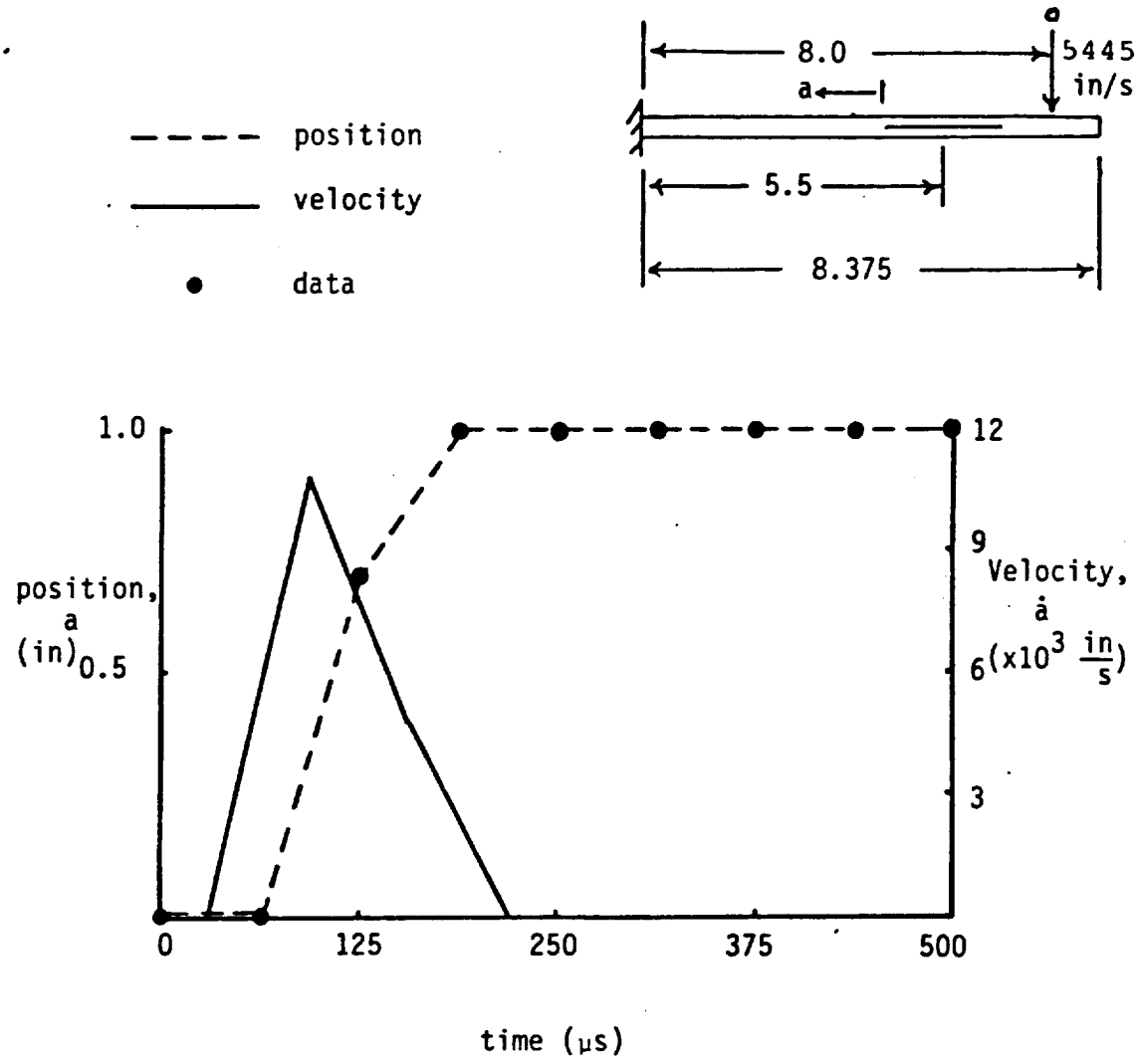

Figure 3.15 Crack Propagation History in Specimen H4

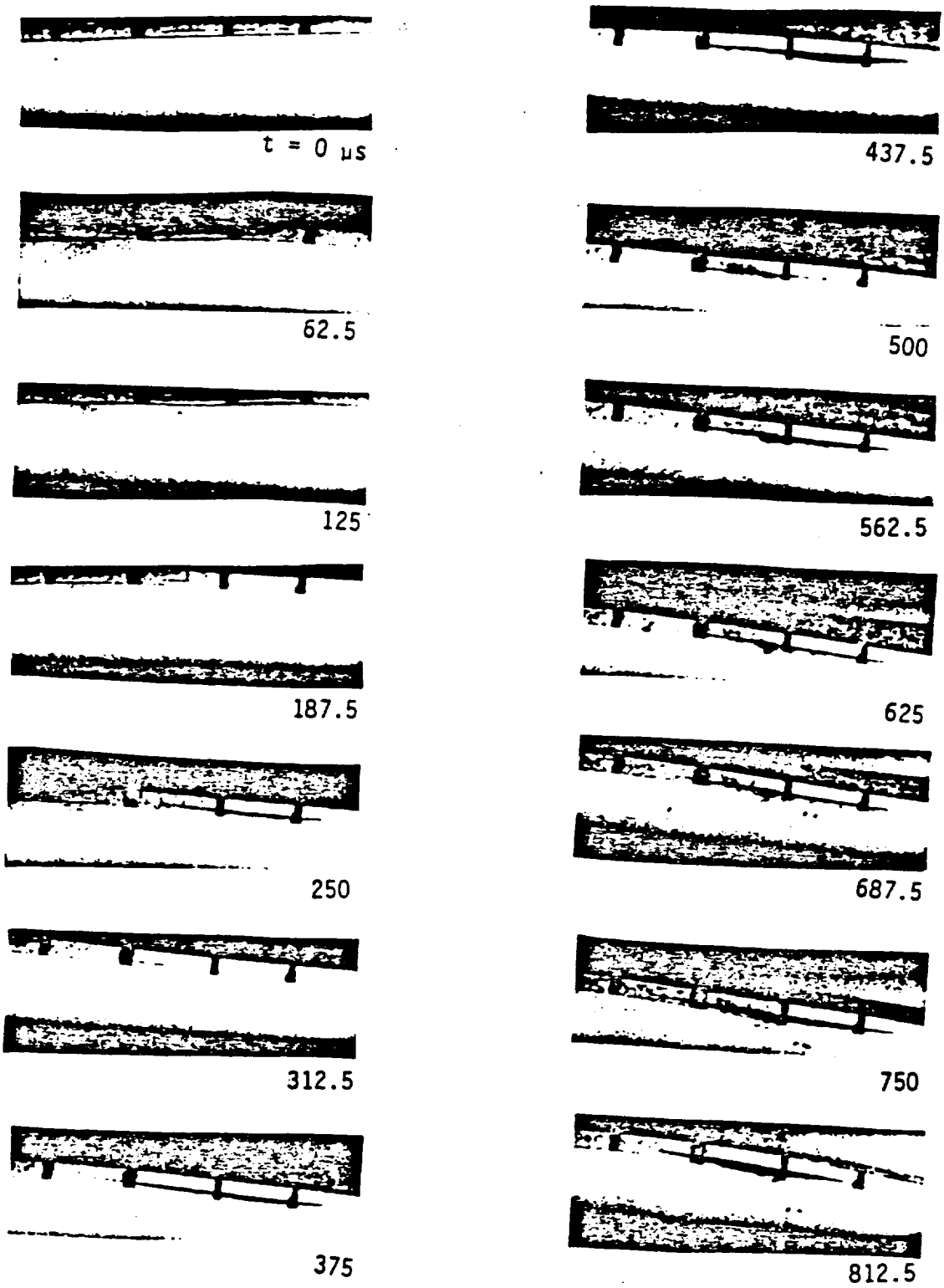

Figure 3.16 Impact Response of Specimen C4

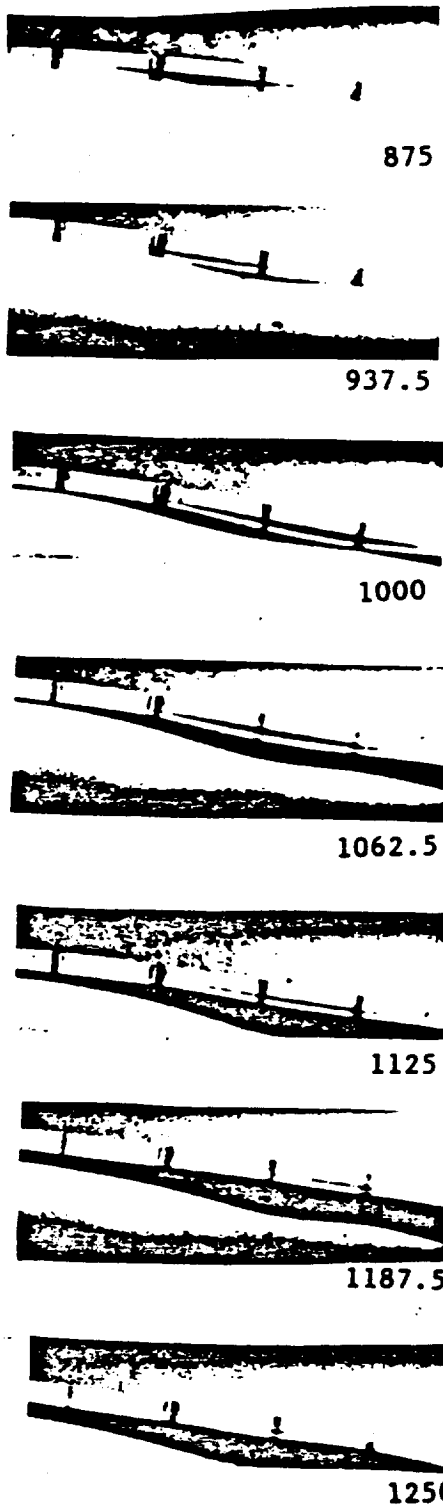

Figure 3.16 (continued)

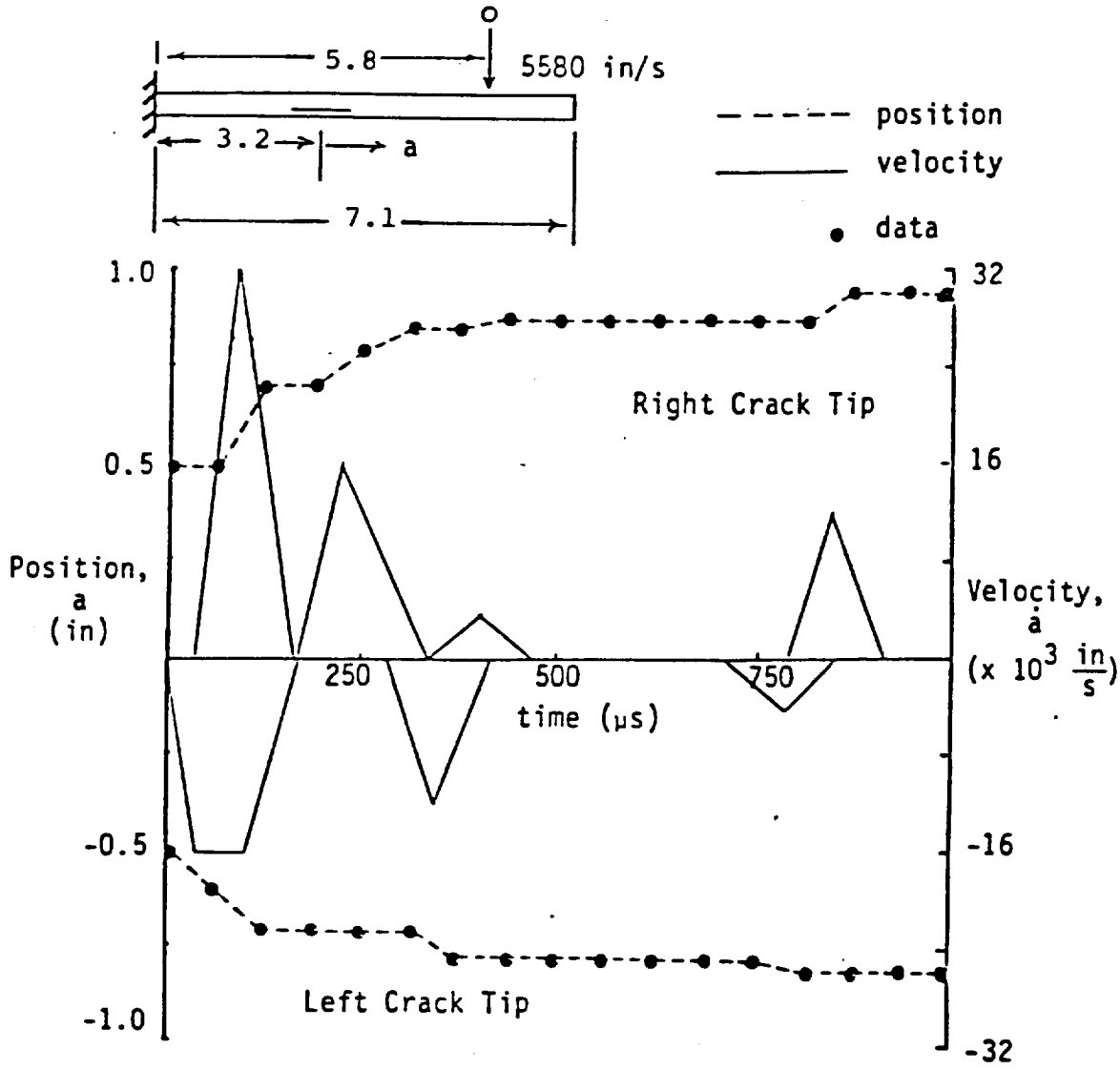

Figure 3.17 Crack Propagation History in Specimen C4

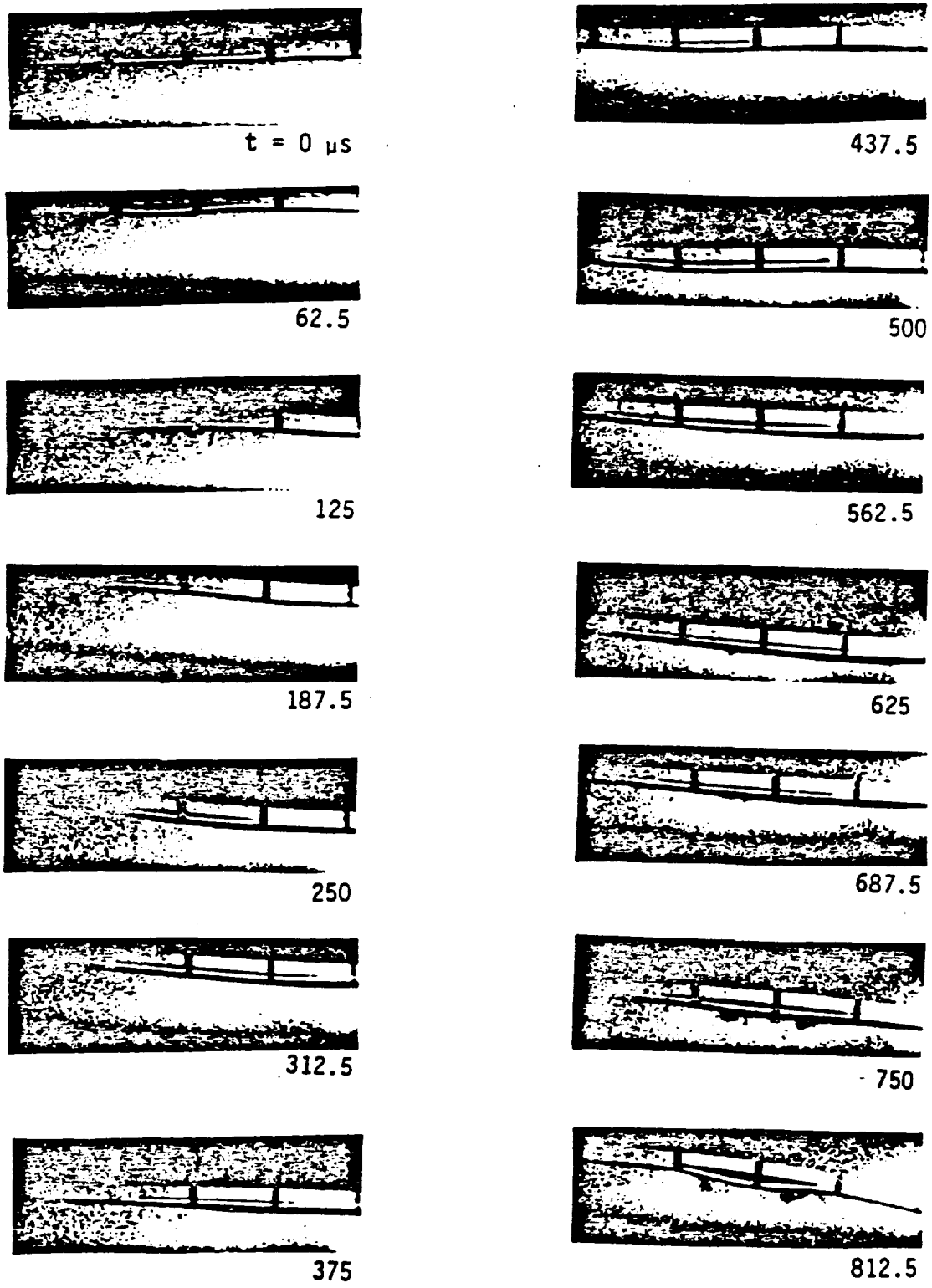

Figure 3.18 Impact Response of Specimen C7

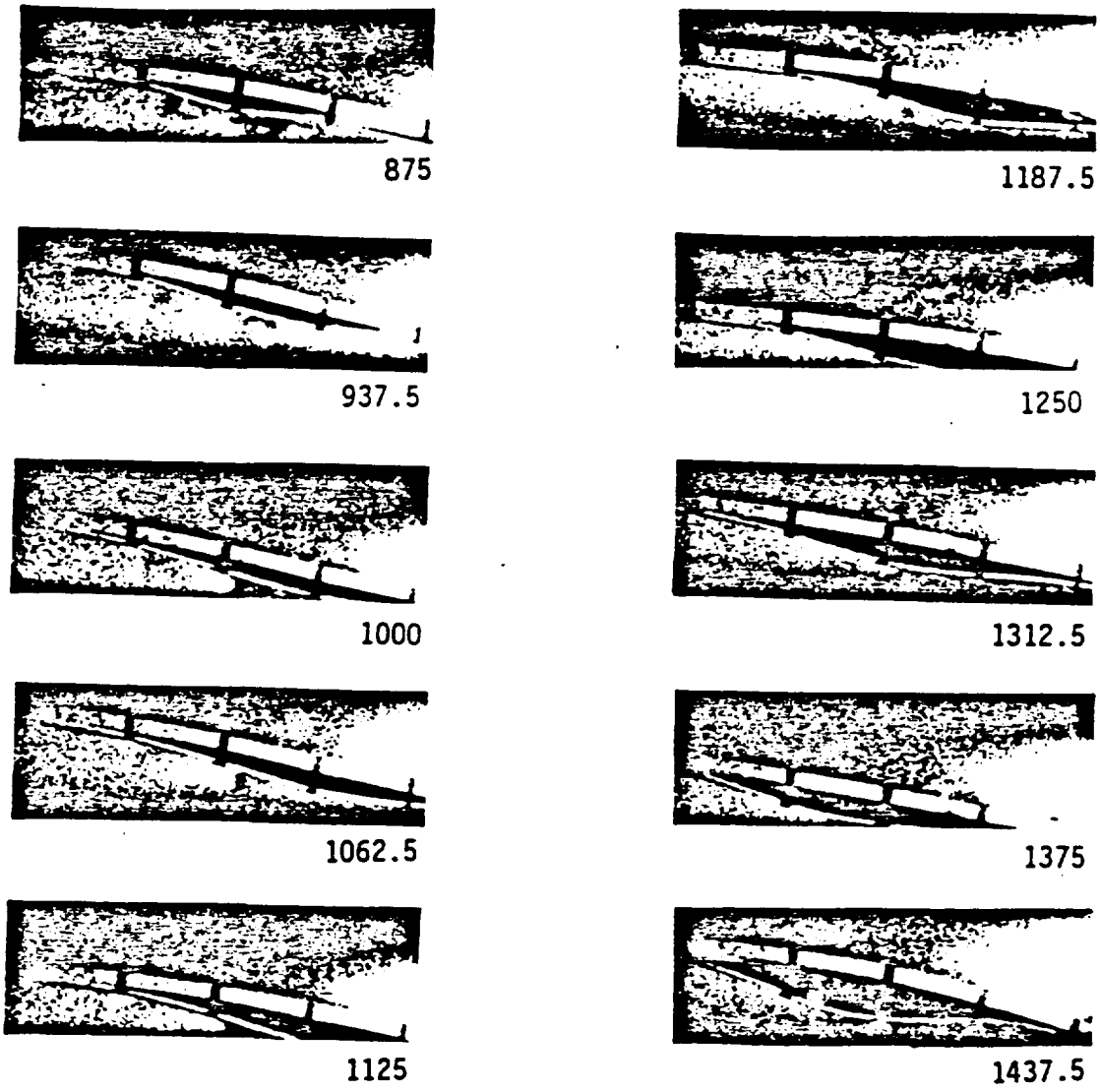

Figure 3.18 (continued)

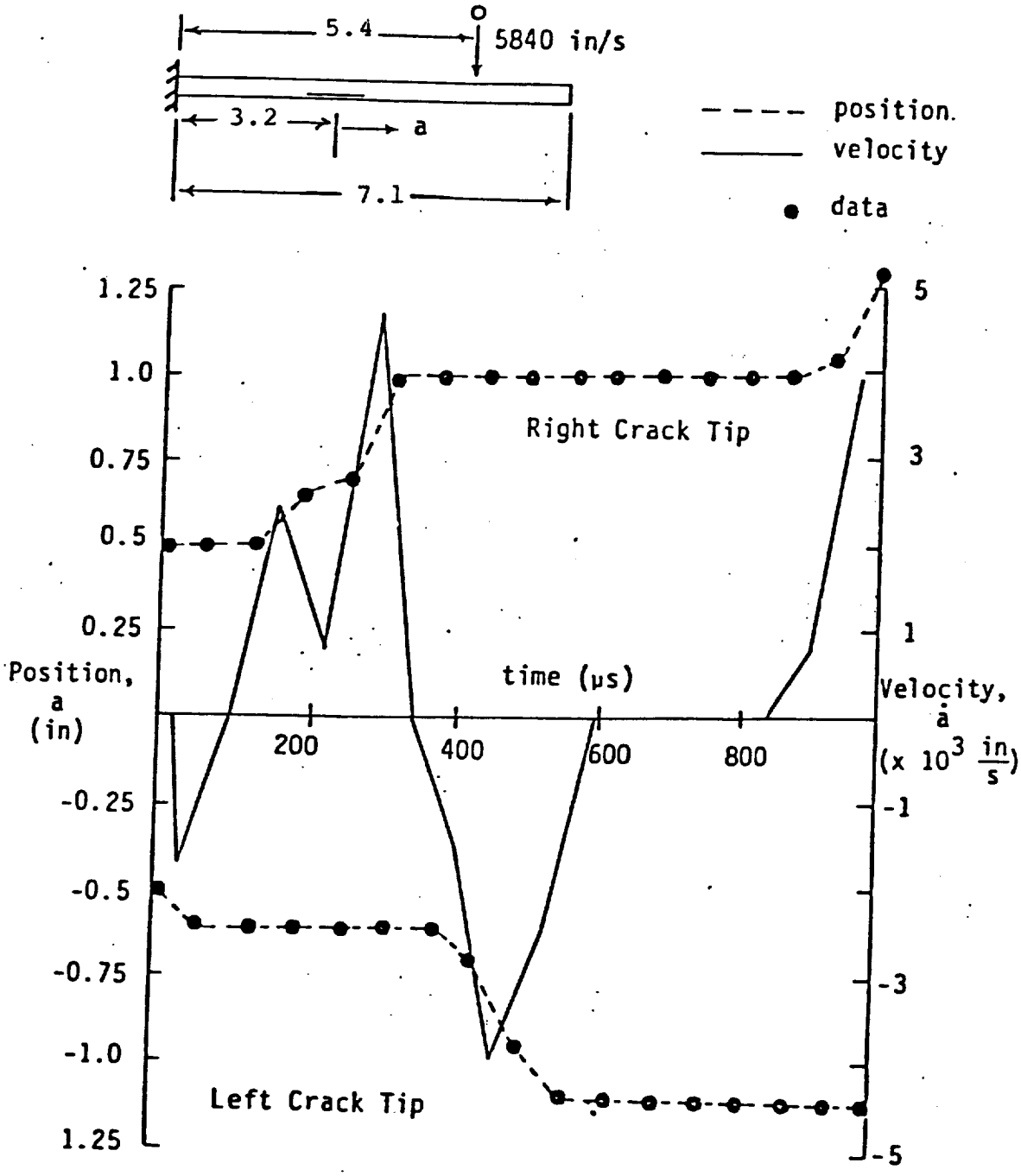

Figure 3.19 Crack Propagation History in Specimen C7

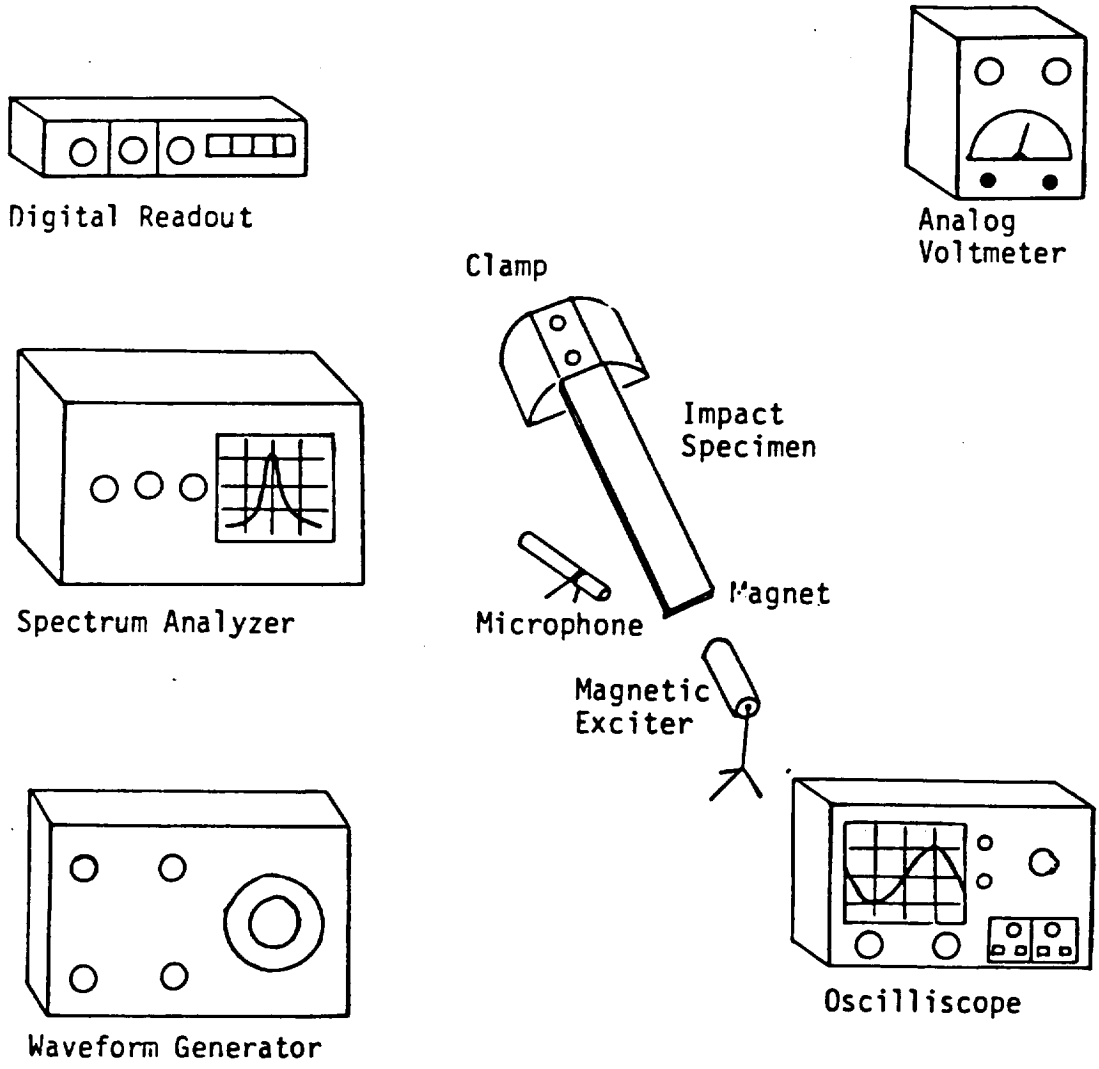

Figure 3.20 Vibration Test Set-Up

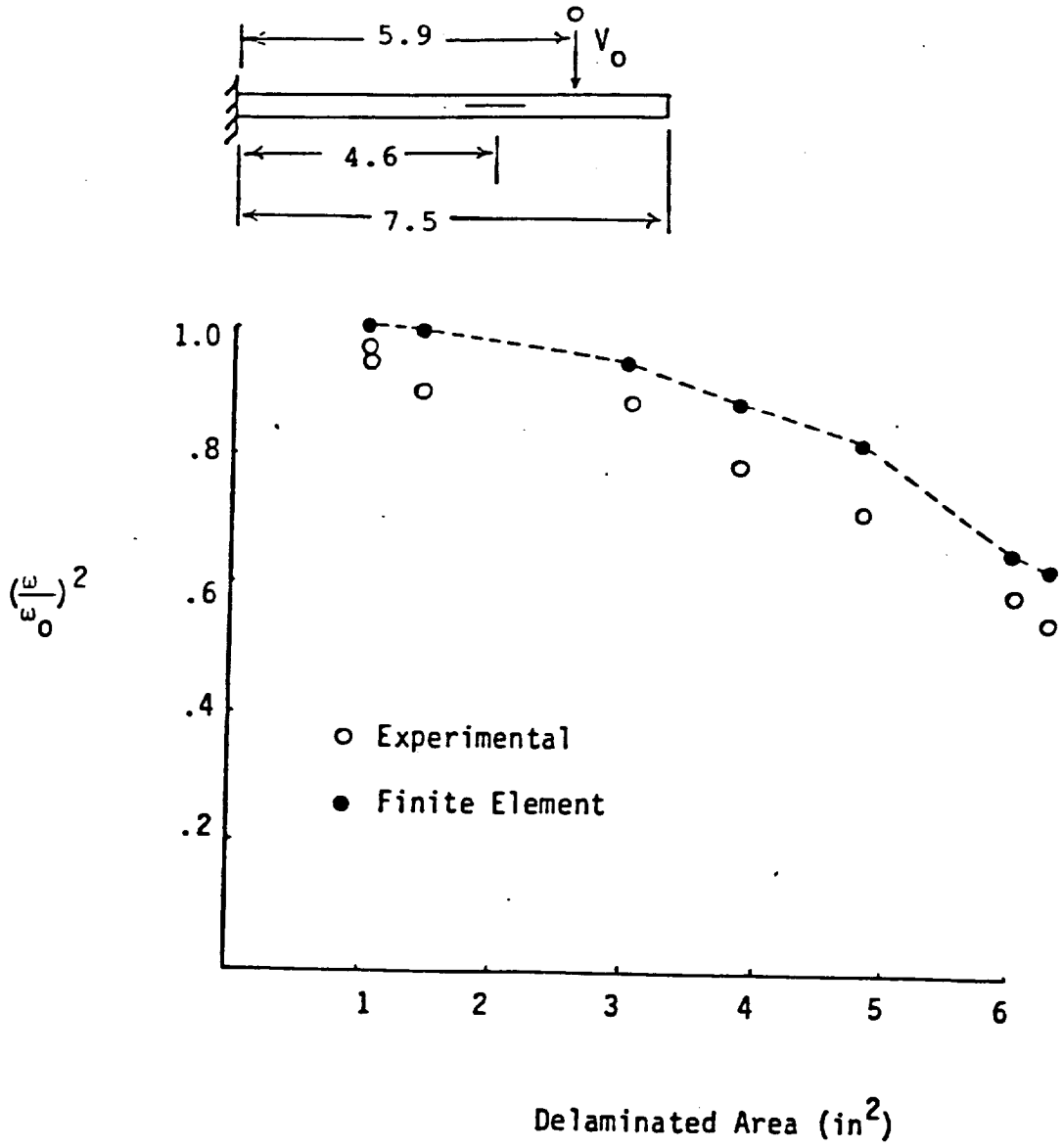

Figure 3.21 Natural Frequency Versus Delaminated Area for First Bending Mode

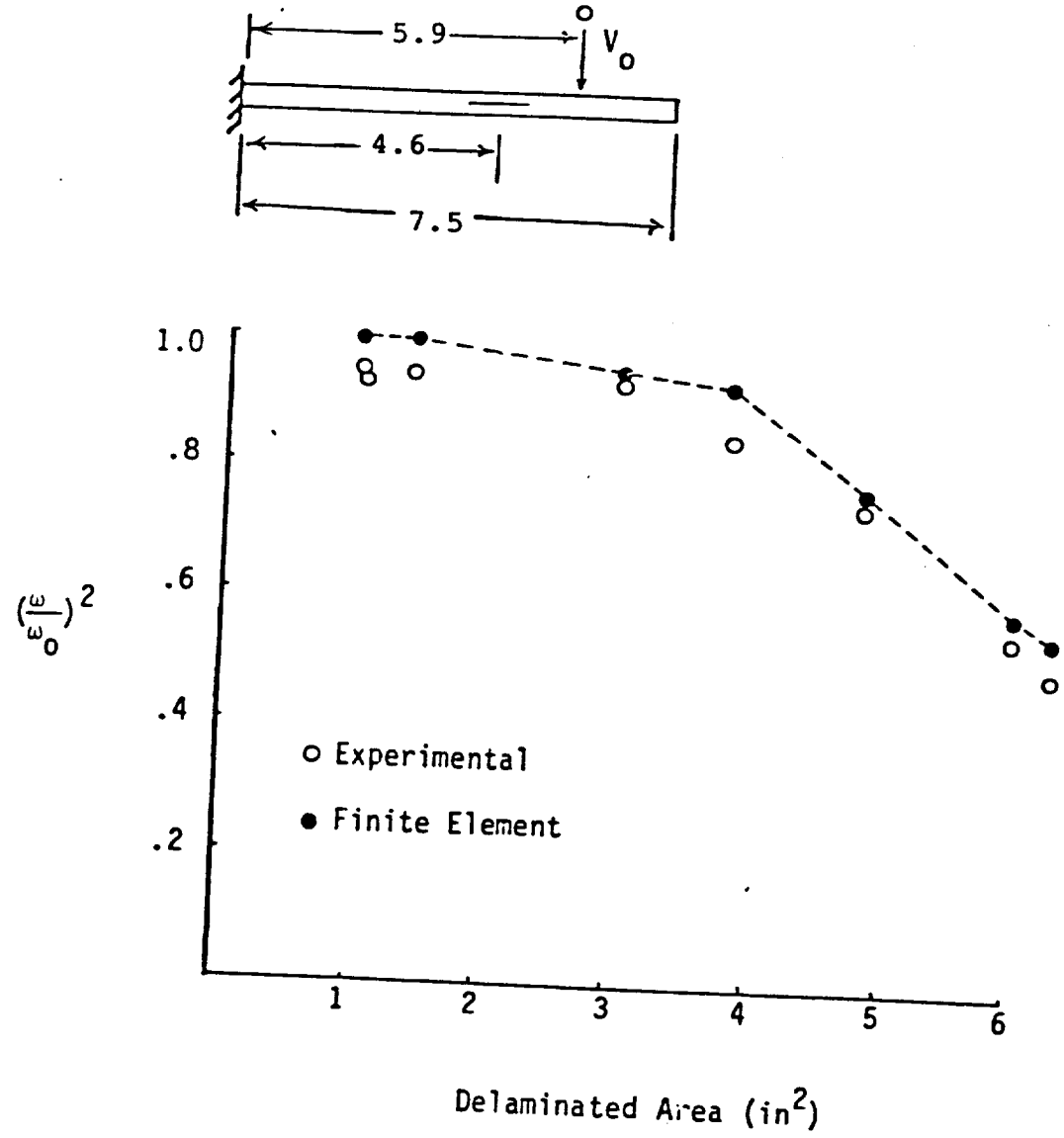

Figure 3.22 Natural Frequency Versus Delaminated Area for Second Bending Mode

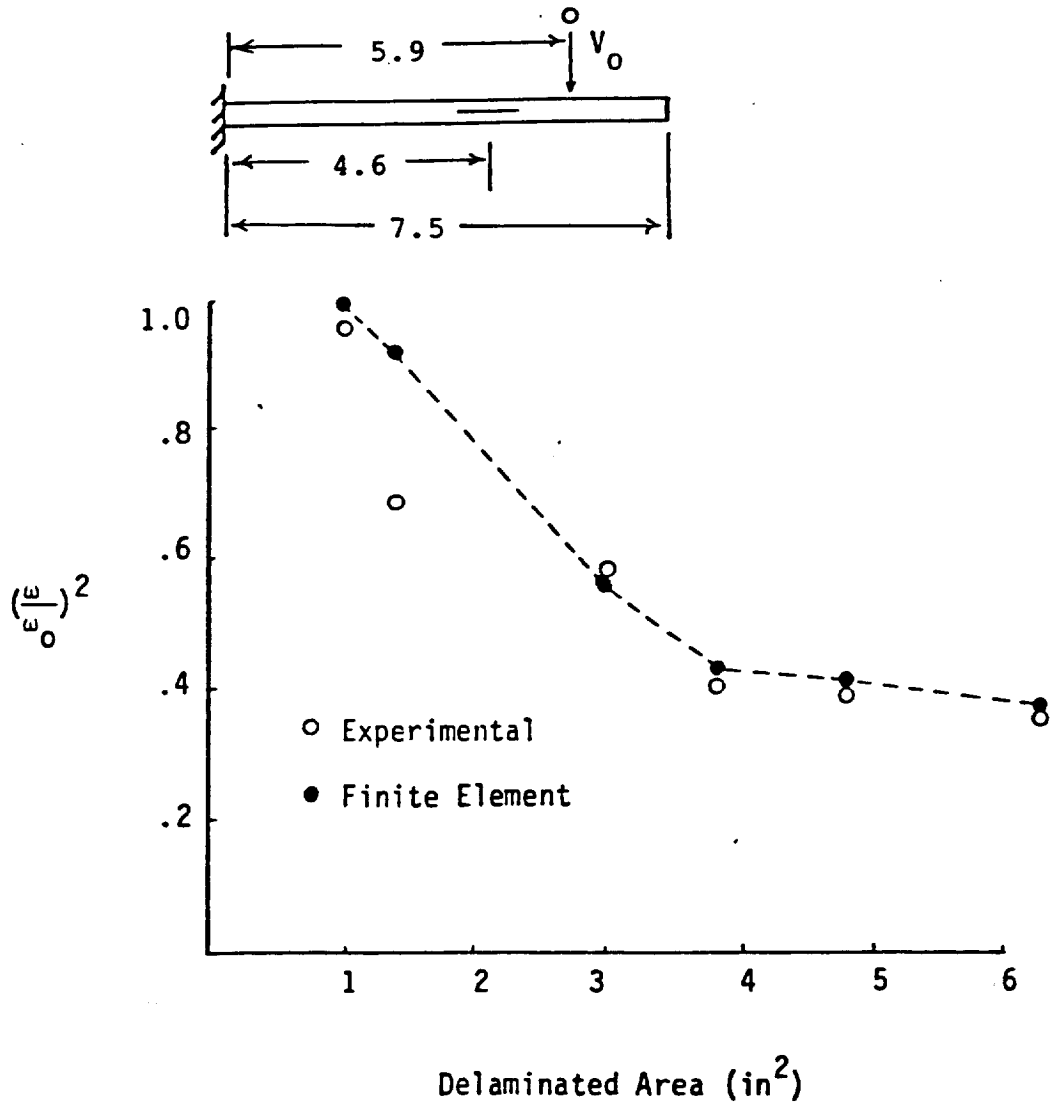

Figure 3.23 Natural Frequency Versus Delaminated Area for Third Bending Mode

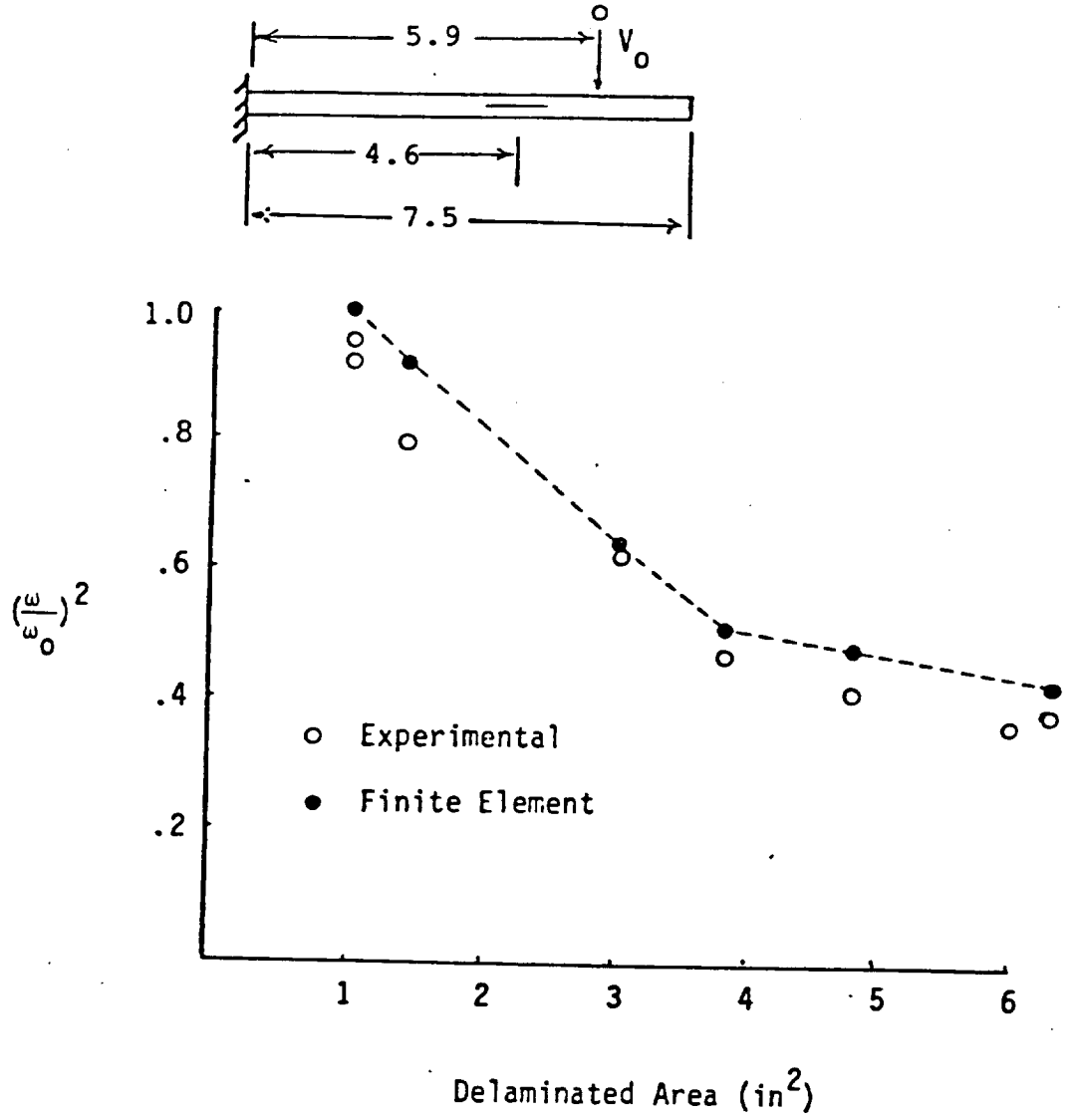

Figure 3.24 Natural Frequency Versus Delaminated Area for Fourth Bending Mode

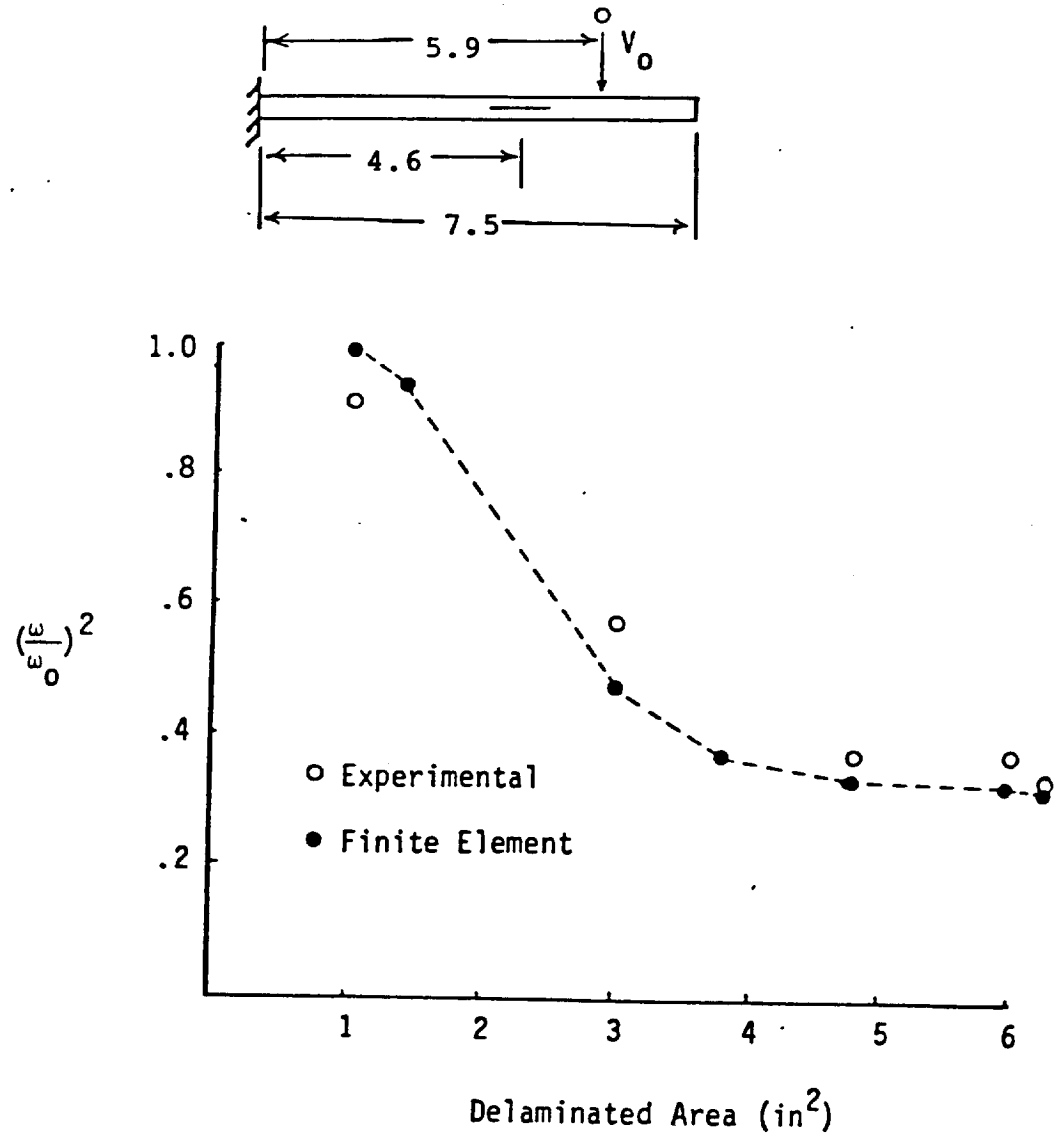

Figure 3.25 Natural Frequency Versus Delaminated Area for Fifth Bending Mode

4. MODELING THE IMPACT FORCE

In order to perform a finite element analysis of the impacted composite specimen, the dynamic force history due to the impact must be determined. In lieu of a direct measurement of the contact force between the impactor and the target specimen, several methods were used to estimate the actual force history. These will be described here.

4.1 Model 1 - Preliminary Model

Daniel et al. [37] conducted an impact experiment on boron/epoxy and graphite/epoxy composite laminates using a 0.3125 in. diameter silicon rubber ball as impactor. Although the contact force was not measured, they were able to determine the contact area as a function of time. The contact area versus time curve was approximated by a sine function. Although the exact relation between the contact force and contact area is still unknown, it seems reasonable to assume that the contact force can also be approximated by a sine curve as

$$\begin{aligned} F(t) &= F_0 \sin\left(\frac{\pi t}{T}\right) && 0 < t < T \\ &= 0 && t > T \end{aligned} \tag{4.1}$$

where T is the contact duration. To determine the unknown coefficients F_0 and T the following experiment was performed.

An uncracked cantilever beam specimen, shown schematically in Fig. 4.1, was impacted with the half-inch diameter silicon rubber ball at the velocity of 1166 in/sec. Two strain gages (Micro Measurements ED-DY-031CF-350, S_g = 3.25) were mounted on the back side of the specimen to measure the bending strain history. One of the gages was mounted directly opposite the impact point, and the other gage was placed at 2.0 inches away from the first gage. The strain histories measured by these two gages are presented in Figs. 4.1 and 4.2.

A finite element model using 4-node isoparametric plane strain finite elements was then used to model the impacted beam and calculate the strains at the two gage locations. A uniform mesh of 1200 elements (2800 d.o.f.) was found to yield a converged solution and was used to find the values of F_o and T that best matched the experimental results. A detailed description of the finite element modeling procedure used is given in the next chapter. The finite element results shown by the dashed line in Figs. 4.1 and 4.2 were obtained with F_o = 44 lb. and T = 225 μs. In fitting these values, it was found more convenient to vary T to fit the time-phase and then determine the force amplitude F_o, as the strain is linearly proportional to the amplitude.

4.2 Model 2 - Experimental Model

The dynamic response of the impact specimen will be predicted more accurately if the estimate of the force history is improved. The actual force history from the impact of the rubber impactor was therefore determined experimentally.

4.2.1 Impact of a Longitudinal Bar

Longitudinal stress waves propagate nondispersively in a uniform thin bar. An instrumented bar is therefore well suited to determining the force history due to longitudinal impact [10, 38]. It is conceivable, if the deflection of the target does not significantly affect the contact force, that the force history determined from the impact of the longitudinal bar would be nearly the same as that experienced by the composite laminate under the same impact conditions.

The experimental set-up used is shown schematically in Fig. 4.3. The equipment used is similar to that used for the impact of the cracked laminates with the addition of the apparatus needed for measuring the strain history. As the strain pulse passes the gage, the measured change in voltage output is amplified by the pre-amp. The resulting strain history is stored in the Biomation waveform recorder and displayed on the oscilloscope. If necessary, the strain history can be plotted on paper using the X-Y plotter. The force history can be calculated directly from the measured strain.

4.2.1.1 Hertzian Contact Law - Analysis of Low Speed Longitudinal Impact of a Bar

Hertz [39, 40] derived the force-indentation relation for the general case of two spherical elastic masses coming in contact with each other. To summarize the Hertzian contact law, we have

$$F = K\alpha^n \tag{4.2}$$

where

F = contact force between spheres

α = relative indentation between spheres (v_1-v_2)

$n = 1.5$

and

$$K = \frac{4}{3}\sqrt{\frac{R_1R_2}{R_1+R_2}}\left(\frac{k_1k_2}{k_1+k_2}\right) \tag{4.3}$$

where

R_i = radii of spheres

$$k_i = \frac{E_i}{1-\nu_i^2}$$

and E_i, ν_i are the respective elastic constants. A special case that is of interest here occurs when the target is flat ($R_2 = \infty$) in which case eq. (4.3) simplifies to

$$K = \frac{4}{3}\sqrt{R_1}\left(\frac{k_1k_2}{k_1+k_2}\right) \tag{4.4}$$

Before proceeding to the more complicated problem of the high speed impact of the rubber ball, a preliminary analysis of the low speed impact of a steel ball on the aluminum bar was performed. A finite element program was developed to analyze the longitudinal impact of a bar. Four degree-of-freedom truss elements [41] were used to model the bar.

The equations of motion for a structure subjected to a time dependent force F(t) are

$$\{F(t)\} = [K]\{\delta\} + [M]\{\ddot{\delta}\} \tag{4.5}$$

where $[K]$ is the stiffness matrix,

$[M]$ is the mass matrix,

$\{\delta\}$ is the displacement vector, and

$\{\ddot{\delta}\}$ is the acceleration vector.

In the formulation of this element, both the displacements and the strains at each nodal point are used as degrees of freedom. For the truss element, then, we have

$$\{\delta\}^T = [u_1, (\partial u/\partial x)_1, u_2, (\partial u/\partial x)_2] \tag{4.6}$$

and

$$[K] = EA \begin{bmatrix} 6/5L & & & \text{sym.} \\ 1/10 & 2L/15 & & \\ -6/5L & -1/10 & 6/5L & \\ 1/10 & -L/30 & -1/10 & 2L/15 \end{bmatrix} \tag{4.7}$$

and

$$[M] = \frac{\rho AL}{420} \begin{bmatrix} 156 & & & \text{sym.} \\ 22L & 4L^2 & & \\ 54 & 13L & 156 & \\ -13L & -3L^2 & -22L & 4L^2 \end{bmatrix}$$

where u_i are the nodal displacements,

EA is the axial stiffness of the element,

ρA is the mass per unit length, and

L is the length of the element

A detailed derivation of the equations of motion for this high-order truss element is given in [41].

The only non-zero term in the force vector {F(t)} is that corresponding to the displacement at the impact point on the bar. The contact behavior between relatively hard materials such as steel and aluminum is well described by the Hertzian law. The Hertzian contact law was therefore incorporated into the longitudinal bar finite element program to perform the low speed longitudinal impact analysis.

The Hertzian impact force is given by eq. (4.2). In this case the indentation is

$$\alpha = x-u \tag{4.8}$$

where

x = displacement of the impactor

u = bar displacement at the impact point

The equation of motion for the center of mass of the impactor is

$$F = m\ddot{x} \tag{4.9}$$

where F is the impact force given in eq. (4.2) and m is the mass of the impactor.

Equation (4.9) must be solved simultaneously with the equations of motion for the bar to determine the dynamic force history. The initial conditions are given as

$$x(o) = \ddot{x}(o) = u(o) = F(o) = 0, \; \dot{x}(o) = v \tag{4.10}$$

where v is the impact velocity. The following algorithm was used to determine the impact force.

$$x_{i+1} = x_i + \dot{x}_i \, \Delta t + \ddot{x}_i \, \frac{(\Delta t)^2}{2} \tag{4.11}$$

$$F_{i+1} = k \, (x_{i+1} - u_i)^n \tag{4.12}$$

$$\ddot{x}_{i+1} = -F_{i+1}/M \tag{4.13}$$

$$\dot{x}_{i+1} = \dot{x}_i + \ddot{x}_i \, \Delta t \tag{4.14}$$

where Δt is the integration time step and the notation $x_i = x(t = i\Delta t)$ has been used. Equation (4.12) is only an estimate of F_{i+1} because the displacement u_{i+1} at the impact point has been estimated by u_i from the previous time step.

The experimental set up for the low speed impact tests is identical to that shown in Fig. 4.3 with the exception that the steel impactor was suspended as a pendulum and dropped, instead of being fired ballistically with the air gun. Figure 4.4 compares the measured force history with that obtained using a 39-element (80 d.o.f.) model of the bar and an integration time step Δt of 0.5 μsec in the finite element program. Figure 4.5 shows the strain history measured at a

single gage location on the bar compared to the finite element result. These results seem to verify that the longitudinal bar finite element program accurately predicts the strain history due to a Hertzian impact. Figure 4.6 shows the propagation and reflection of the strain pulse along the bar as calculated by the finite element program. The boundary conditions of the bar are free-free, so the compressive incident pulse reflects from the distal end of the bar as a tensile pulse of identical shape.

4.2.1.2 High Speed Longitudinal Impact of a Bar

The ballistic impact set up shown in Fig. 4.3 was used to measure the strain history resulting from impact of the rubber ball on the aluminum bar. The force history can be calculated directly from the measured strain.

Figure 4.7 shows a typical measured impact force versus time behavior for the impact of the half-inch diameter ball. A simple approximation can be used to describe the curve:

$$F(t) = \begin{cases} F_o \sin\left(\frac{\pi t}{2t_{F_o}}\right) & o < t < t_{F_o} \\ F_o \cos\frac{\pi(t-t_{F_o})}{2(T-t_{F_o})} & t_{F_o} < t < T \\ 0 & t > T \end{cases} \qquad (4.15)$$

where F_o is the maximum force, t_{F_o} is the time when the maximum force occurs, and T is the contact duration. Each of these three parameters used in describing the approximate force history can be read directly

from a three-parameter estimate of the actual force history such as that shown in Fig. 4.7.

A series of tests was performed to determine how the force history varied with impact velocity. Figures 4.8-4.10 show the variation in shape and amplitude of the force history resulting from impact of the half-inch ball on the bar. Figure 4.8 shows that the amplitude of the force varies in proportion to v^2, which is in contrast to the linear behavior predicted by the simple spring-mass single-dof impact model [42]. Figure 4.9 shows that the contact time varies inversely with the impact velocity, which is also in contrast to the spring-mass model, which predicts that the two are independent. Figure 4.11 shows that the impulse measured from the experimental data varies linearly with impact velocity.

A second series of tests was conducted with a smaller (3/8 inch diameter) ball of the same material in order to further characterize the impactor. The results presented in Figs. 4.12-4.15 show that the trends followed by the data are similar to those observed for the impact of the larger ball. The maximum force varies in proportion to v^2, the contact duration varies inversely with v, and the shape t_{F_o}/T of the force history is approximately constant over the velocity range tested.

4.2.2 High Speed Transverse Impact of a Laminated Beam

The impact force history for the specimen shown in Fig. 4.1 is adequately approximated by eq. (4.15) with the parameters F_o = 42 lb., t_{F_o} = 35 μsec, and T = 415 μsec. The calculated strain response is compared with the measured values in Figs. 4.1 and 4.2. There is a

significant improvement over the results obtained with the two-parameter approximation in eq. (4.1). Therefore, in all subsequent impact analyses, the force history used will be of the form given in eq. (4.5).

To establish Force History versus Impact Velocity relations for the beam specimen analogous to those shown in Figs. 4.8-4.10 for the bar, a further series of experiments was conducted with composite laminates of geometry and lay-up similar to those used in the crack initiation studies. The notable differences in these specimens were that they had no initial delamination, and two strain gages (MM ED-DY-031CF-350, S_g = 3.25) were mounted on each of them as shown schematically in Fig. 4.16. Two specimens of different lengths were tested in order to see the effect of the specimen size on the force history. The strain history at both gage locations was recorded up to approximately 1000 μs after impact with the equipment shown in Fig. 4.3. Strain histories were obtained for impact velocities ranging from 1000 to 4000 inches per second.

The composite laminate was modeled with plane strain finite elements. A uniform mesh of 1200 elements and 2800 total degrees of freedom was found to yield a converged solution which adequately modeled the dynamic response of the laminate. A more detailed description of the finite element modeling procedure is given in Chapter 5. The three parameters in the assumed force history given in eq. (4.5) were varied in the finite element analysis to match the measured strain response. Comparisons of the measured and numerically obtained strains are shown in Figs. 4.16-4.23 for the shorter specimen

and in Figs. 4.24-4.31 for the longer specimen. The different parameters used in the force histories for these analyses are given in Tables 4.1 and 4.2. The variation of each of the three parameters with impact velocity is shown graphically in Figs. 4.32-4.34. Figures 4.32 and 4.33 indicate that the contact force is lower and the total contact time is longer in the shorter specimen, for a given impact velocity. This indicates that the flexural wave reflections from the boundaries have a significnat effect on the force history. If the effect of the wave motion was not considered, and a single degree of freedom spring-mass model based on the static stiffness of the respective laminates was used to anticipate these trends in the force history, the opposite behavior would be predicted. Indeed, the shape of the force history varies with the length of the target as shown in Fig. 4.34. Comparing these results with those obtained from the longitudinal bar experiment shown in Figs. 4.8-4.10, it is apparent that the relationships between the impact velocity and the three parameters describing the force history are similar. That is, the maximum force varies in proportion to V^2, the contact duration varies inversely with V, and the ratio t_{F_o}/T is relatively constant over the velocity range tested. Although both sets of data follow similar trends, it is also apparent that the different dynamic response of the targets significantly affects the variation of the force history with impact velocity. For this reason, the contact force measured in the bar experiment cannot be applied directly to the impact analysis of the laminates. For laminates of the specific dimensions tested, the data presented in Figs. 4.32-4.34 give more accurate estimates of the actual impact force history.

4.3 Contact Area and Impact Force

It is evident from Fig. 3.7 that a large amount of deformation occurs in the rubber impactor while it is in contact with the composite laminate. This deformation spreads the load due to contact over a larger area than would occur with a more rigid impactor. In calculating the loading used in the finite element model, this force distribution must be accounted for if accurate predictions of the strain near the impact point are needed.

For the purpose of modeling the variation of contact area with time, it is assumed that

$$\frac{A(t)}{A_o} = \frac{F(t)}{F_o} \tag{4.16}$$

where $A(t)$, $F(t)$ are contact area and contact force, respectively, and A_o, F_o are their maximum values. The actual circular contact area of radius r is approximated by a rectangular strip of dimension 2r x 1. Thus,

$$r(t) = r_o\sqrt{\frac{F(t)}{F_o}} \tag{4.17}$$

where $r(t)$, r_o are the contact length and its maximum value. The maximum contact area can be measured from the imprint left by the impactor on the laminate. It is further assumed that the spatial force distribution $f(r)$ over the contact length at any given time is as shown in Fig. 4.35. Hence,

$$f(r) = F_{max} \cos\left(\frac{\pi}{2} \frac{r}{r_o}\right), \quad r < r_o \tag{4.18}$$

The specific nodal force distribution is shown schematically in Fig. 4.35 and is written as

$$f_i = \int_{r_i - \Delta r/2}^{r_i + \Delta r/2} f(r)\, dr \tag{4.19}$$

After imposing the condition

$$\int_{-r_o}^{+r_o} f(r)\, dr = F \tag{4.20}$$

where F is the total force at the given time, (4.5) becomes

$$f_i = \frac{F}{2} \left[\sin \frac{\pi}{4r_o} (2r_i + \Delta r) - \sin \frac{\pi}{4r_o} (2r_i - \Delta r)\right] \tag{4.21}$$

TABLE 4.1 Force Histories Used in Analysis of Impact on Short Composite Beam Specimen

Force History	V(in/s)	F_o(lb)	t_{F_o} (μs)	T(μs)	r_o(in)
1	1166	42	35	415	0.25
2	1981	84	20	310	0.25
3	2994	170	13	205	0.30
4	4049	245	10	155	0.35

TABLE 4.2 Force Histories Used in Analysis of Impact on Long Composite Beam Specimen

Force History	V(in/s)	F_o(lb)	t_{F_o} (μs)	T(μs)	r_o(in)
1	1166	44	30	355	0.25
2	1932	90	21	250	0.25
3	3058	215	13	158	0.3
4	4026	325	10	120	0.35

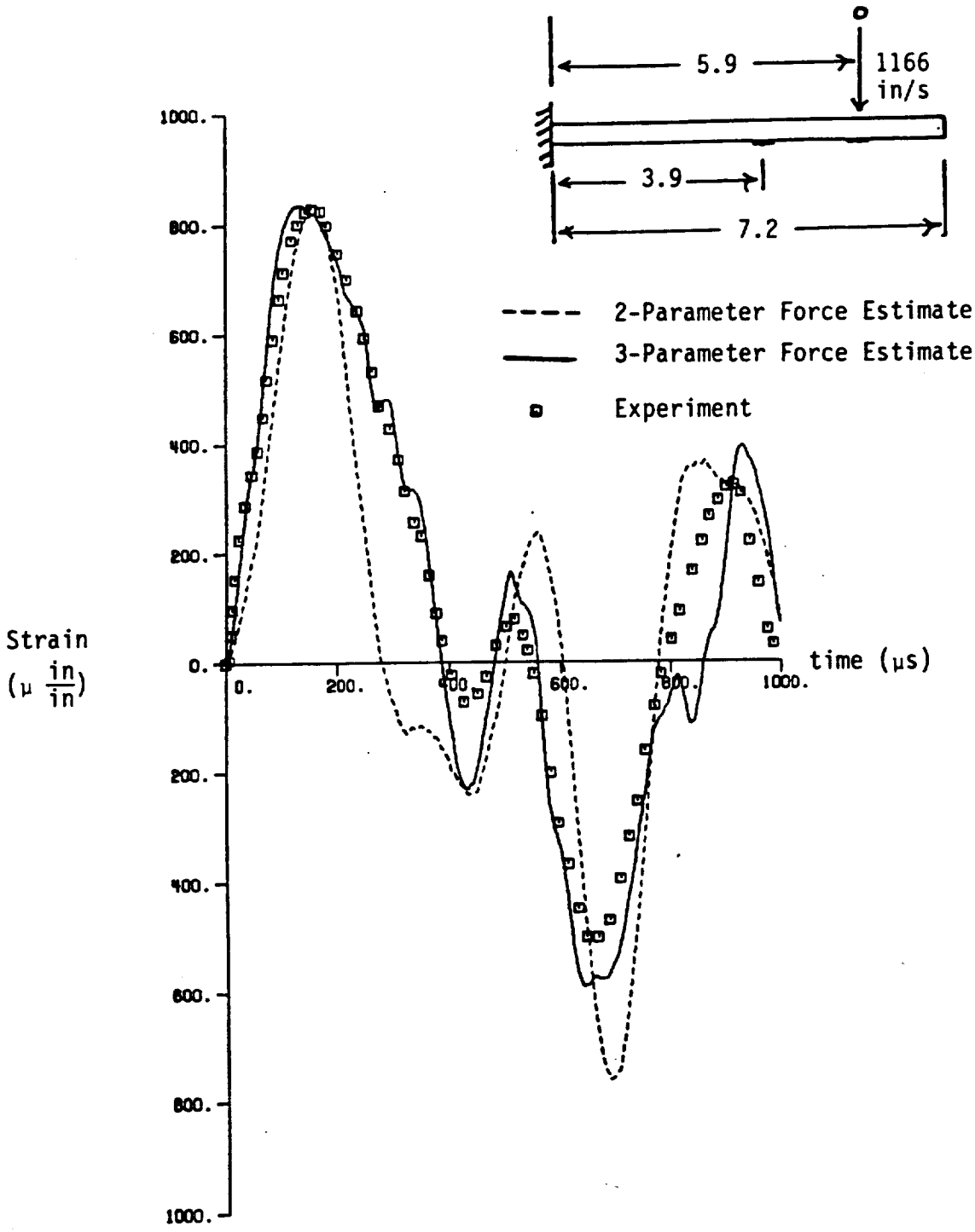

Figure 4.1 Strain History at Impact Point of Beam Subjected to 1166 in/s Impact with Half-Inch Diameter Impactor

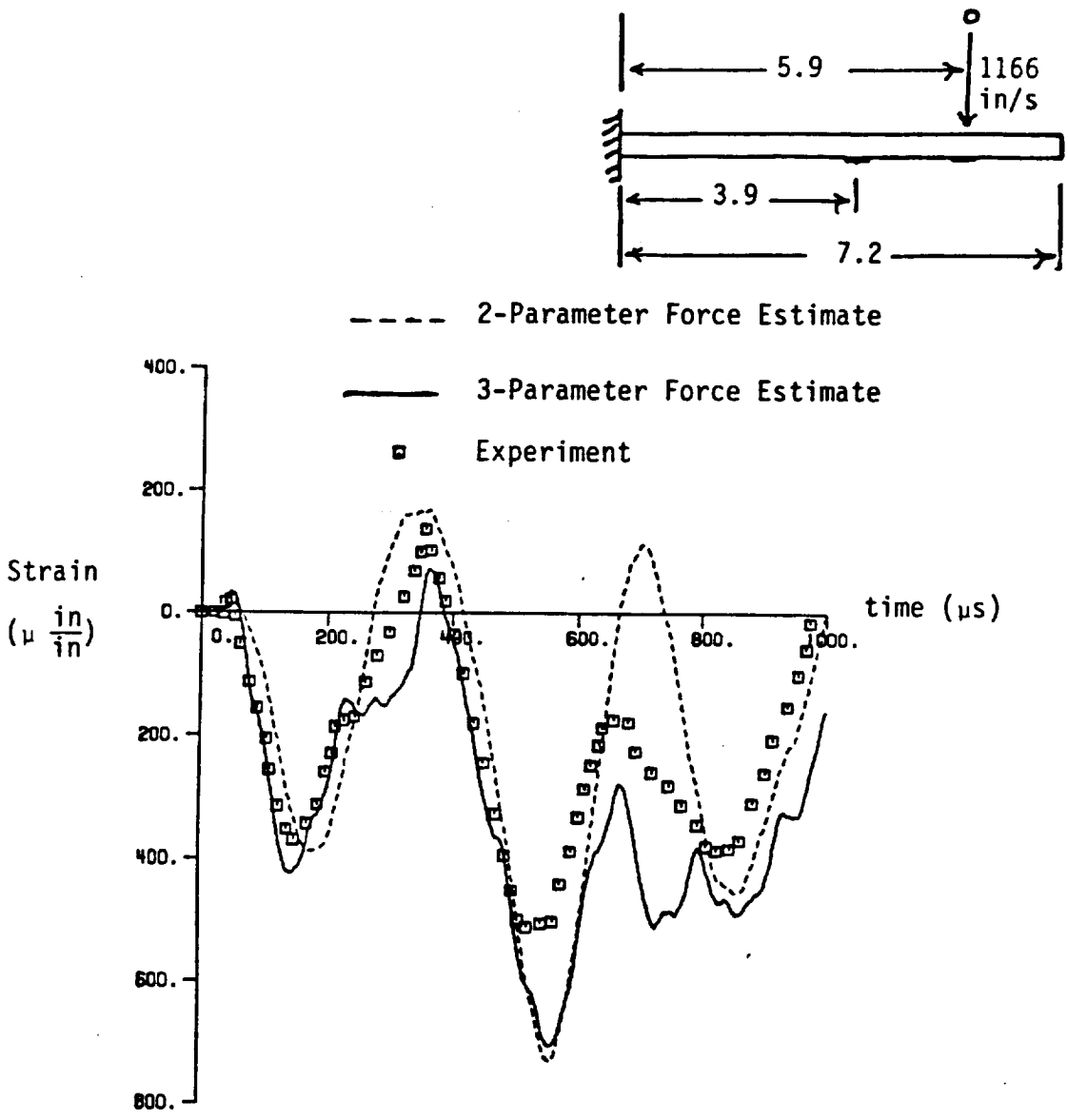

Figure 4.2 Strain History 2.0 Inches From Impact Point of Beam Subjected to 1166 in/s Impact with Half-Inch Diameter Rubber Impactor

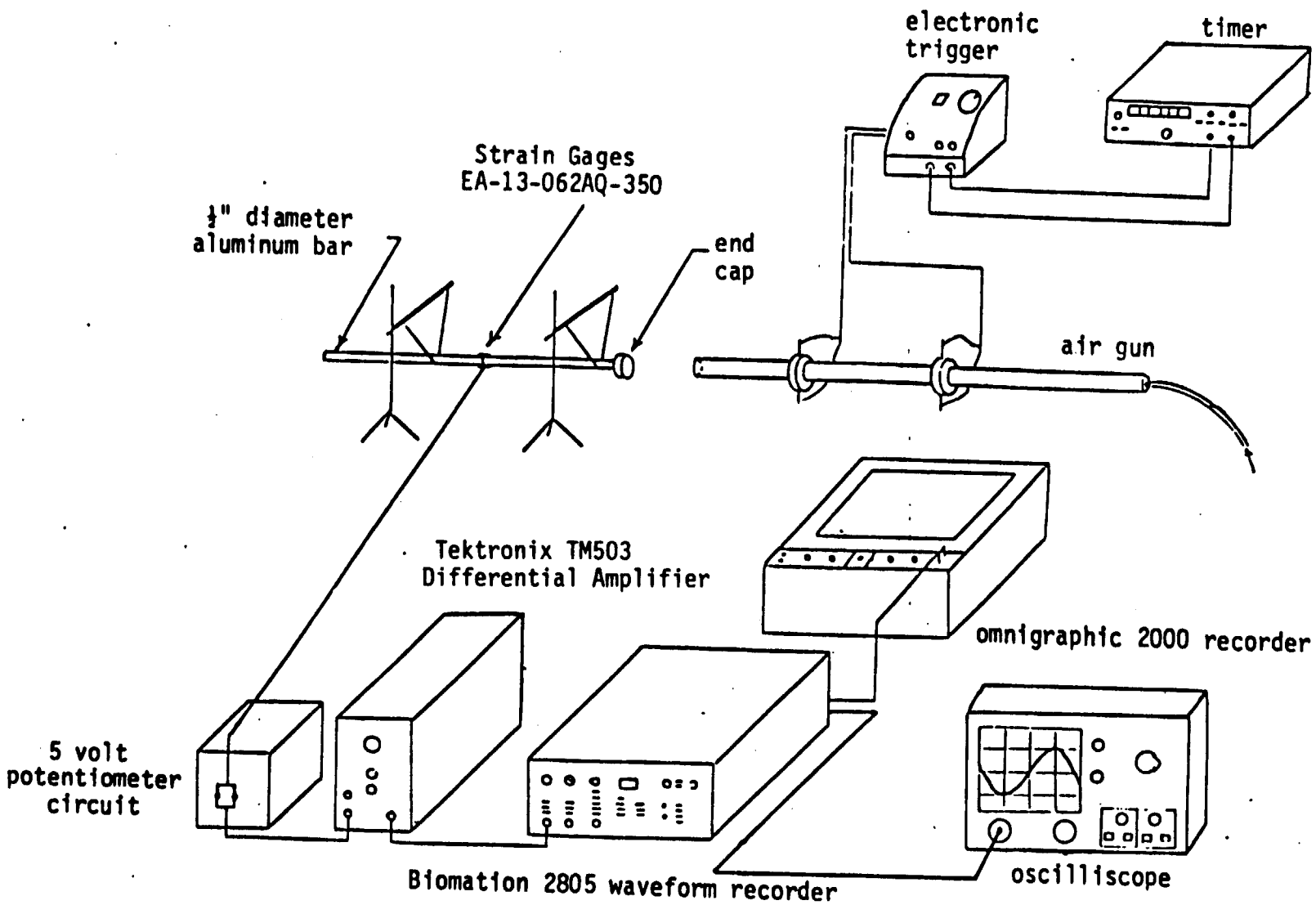

Figure 4.3 Longitudinal Bar Experimental Set-Up

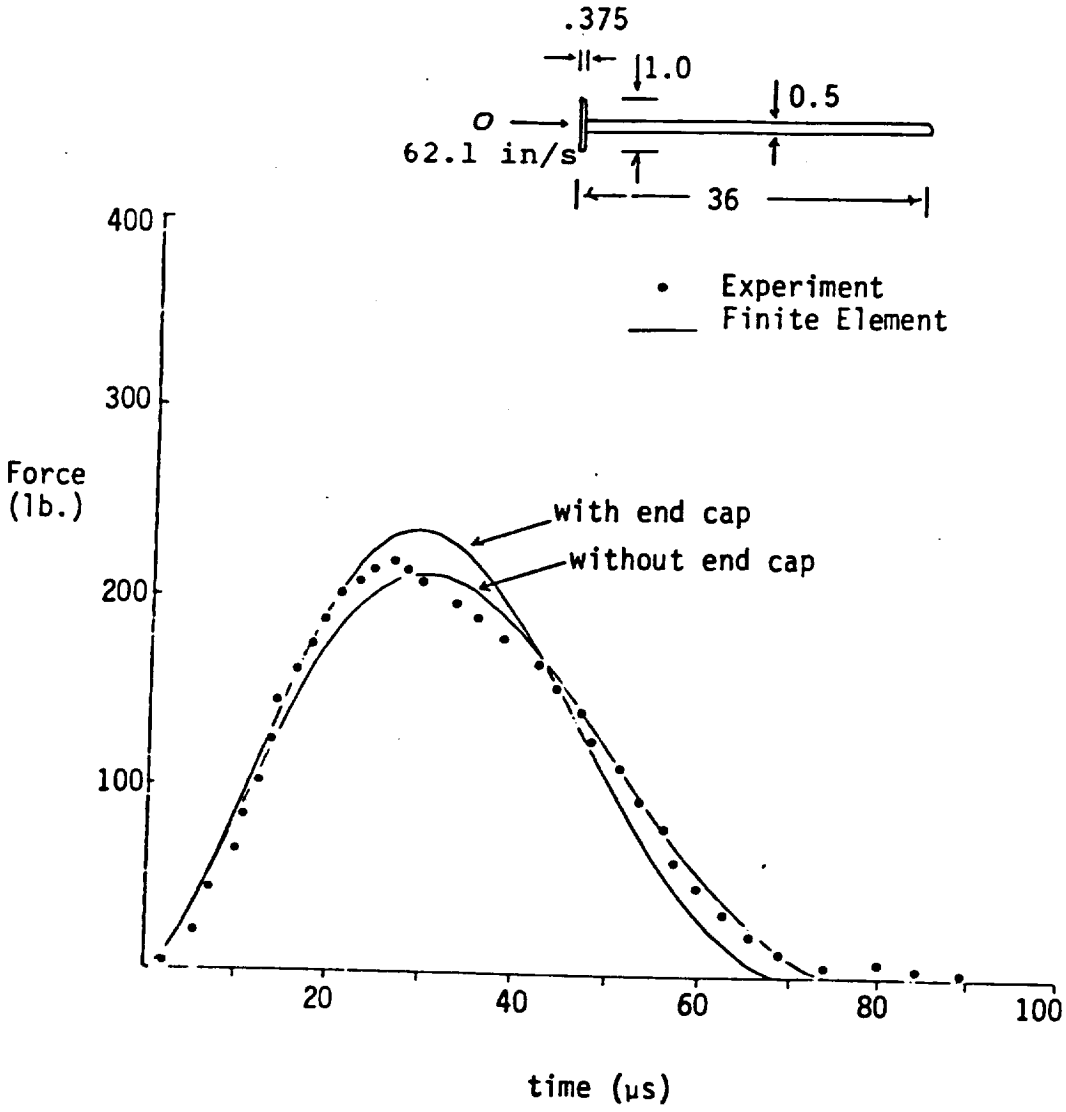

Figure 4.4 Force History From 62.1in/s Impact of 5/8 Inch Diameter Steel Ball on Aluminum Bar

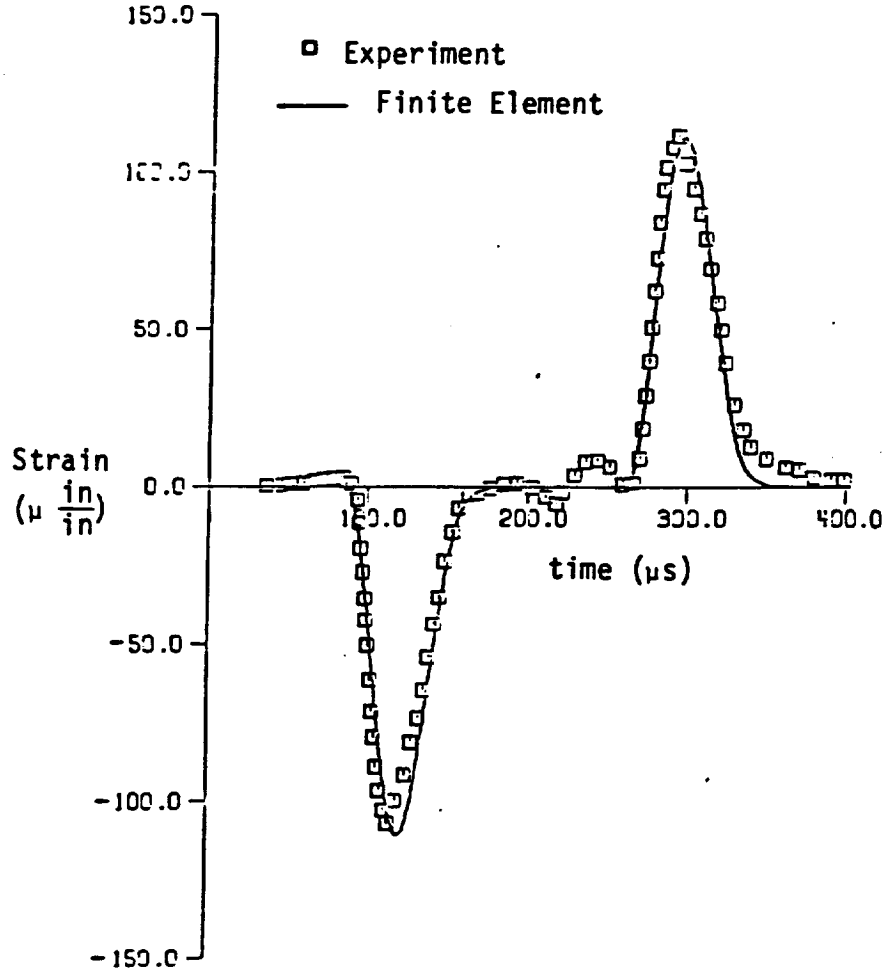

Figure 4.5 Strain History at Midpoint of Bar From 62.1 in/s Impact of 5/8 Inch Diameter Steel Ball

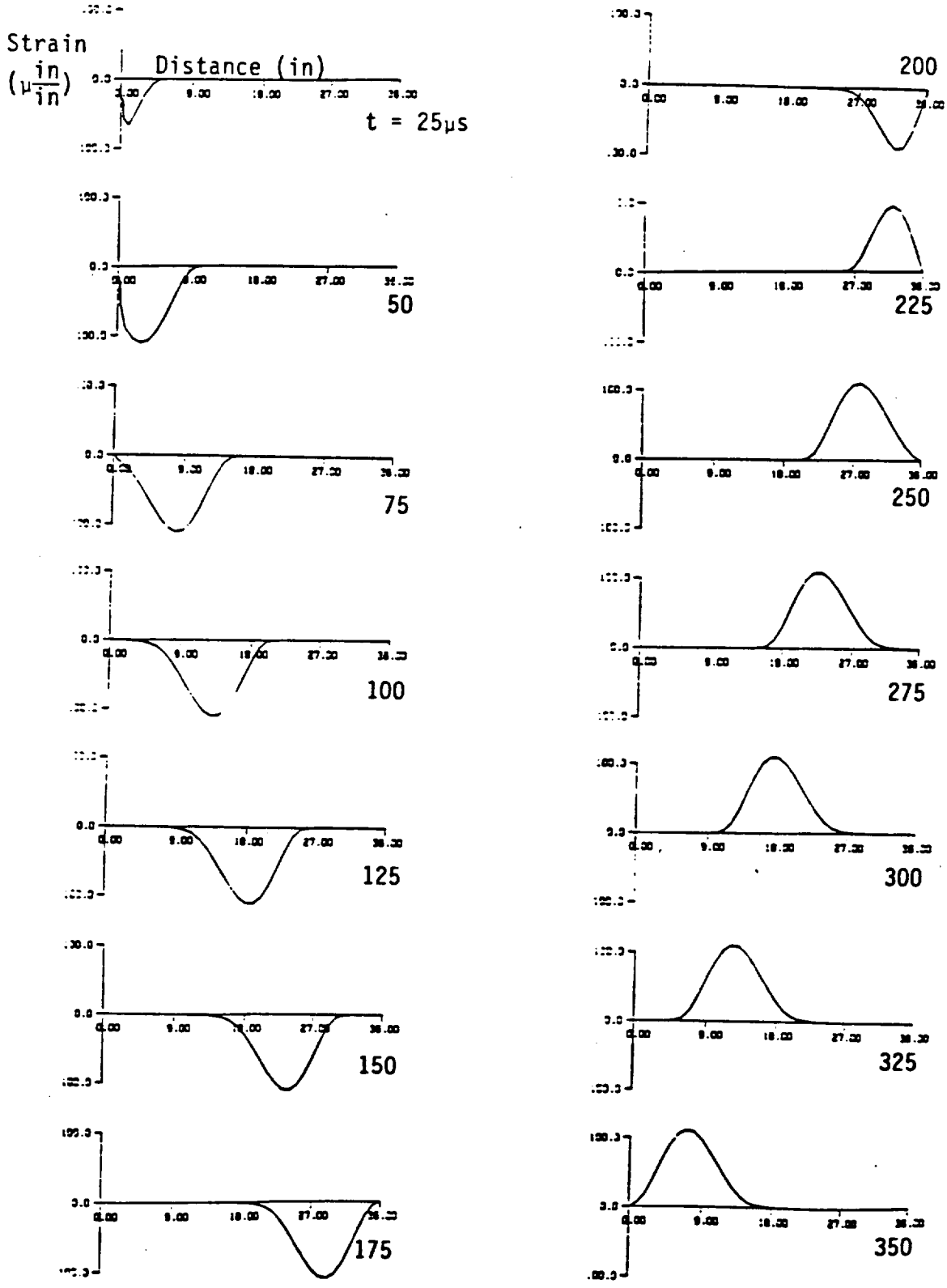

Figure 4.6 Propagation and Reflection of Longitudinal Strain Pulse From 62.1 in/s Impact of 5/8 Inch Diameter Steel Ball

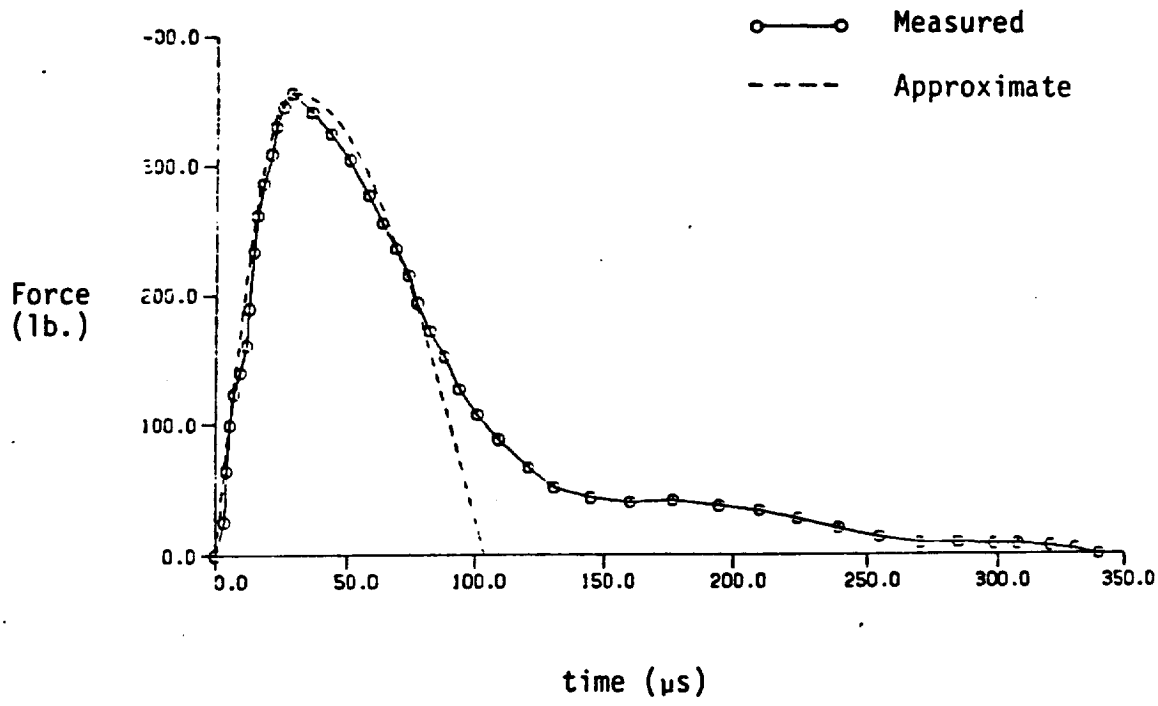

Figure 4.7 Force History Measured From 3500 in/s Impact of Half-Inch Diameter Impactor

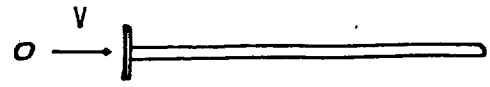

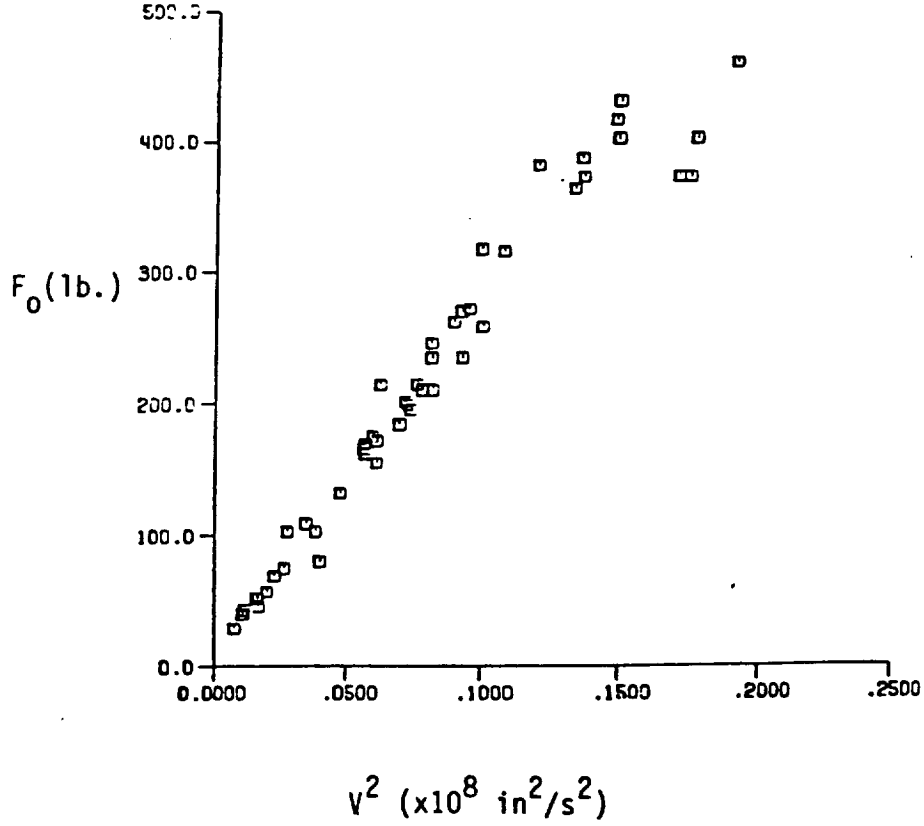

Figure 4.8 Force Amplitude Versus V^2 for Half-Inch Diameter Impactor

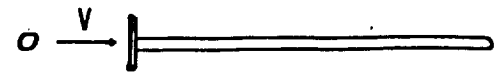

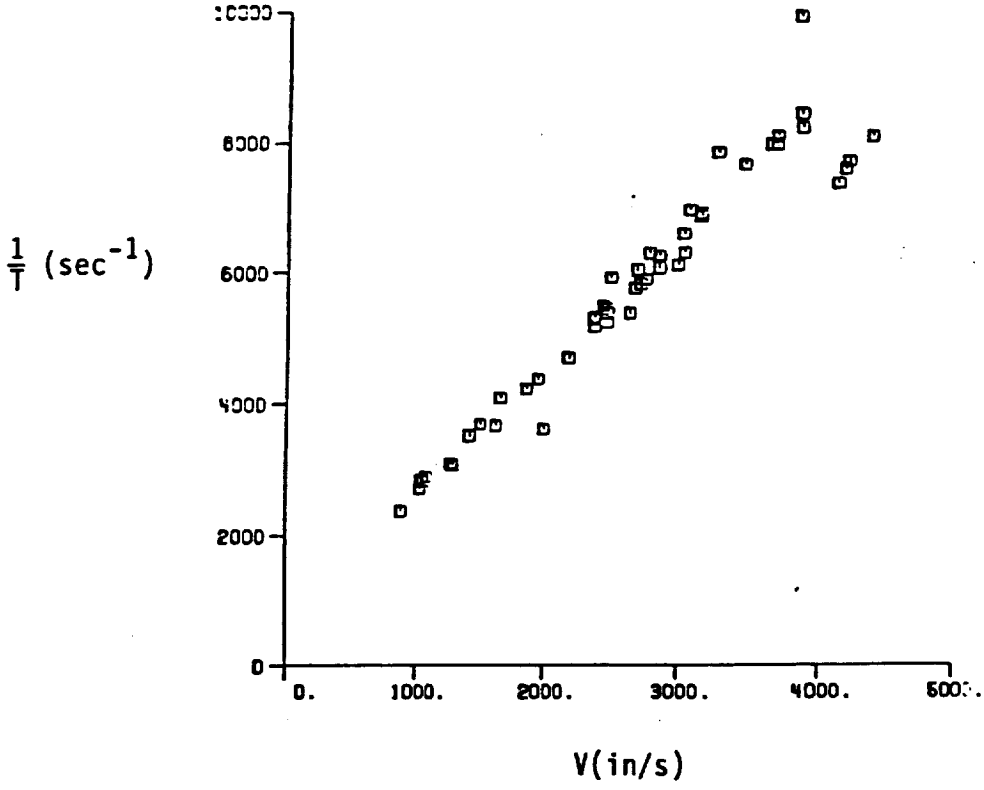

Figure 4.9 Inverse Contact Time Versus Impact Velocity for Half-Inch Diameter Impactor

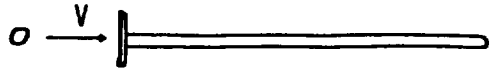

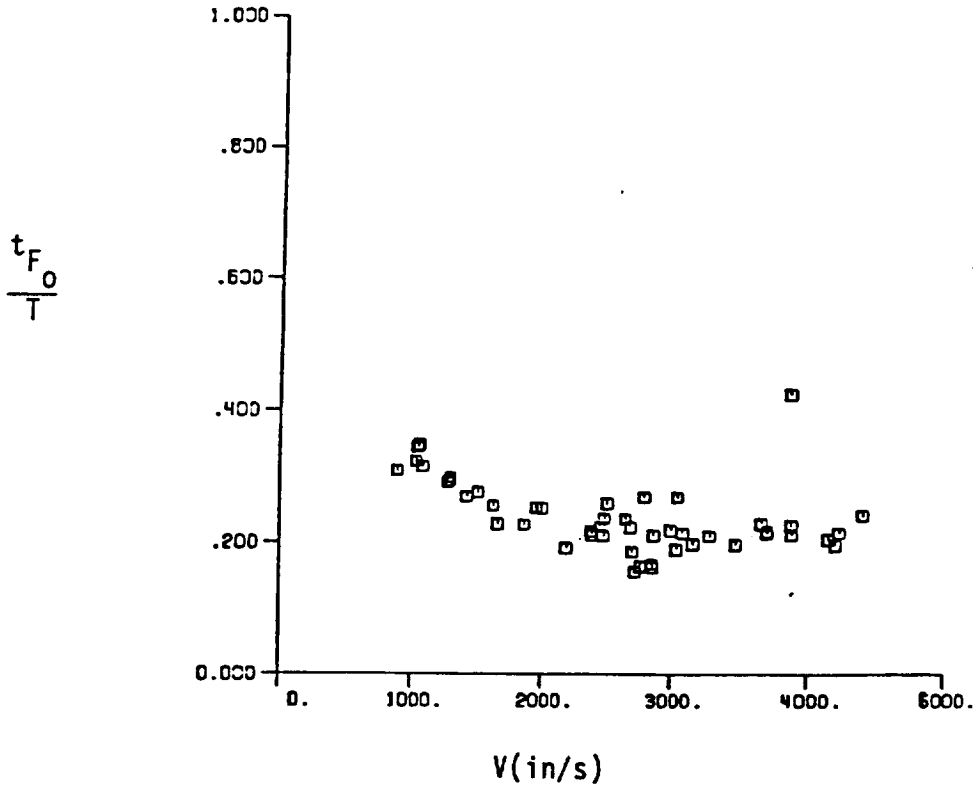

Figure 4.10 t_{F_0}/T Versus Impact Velocity for Half-Inch Diameter Impactor

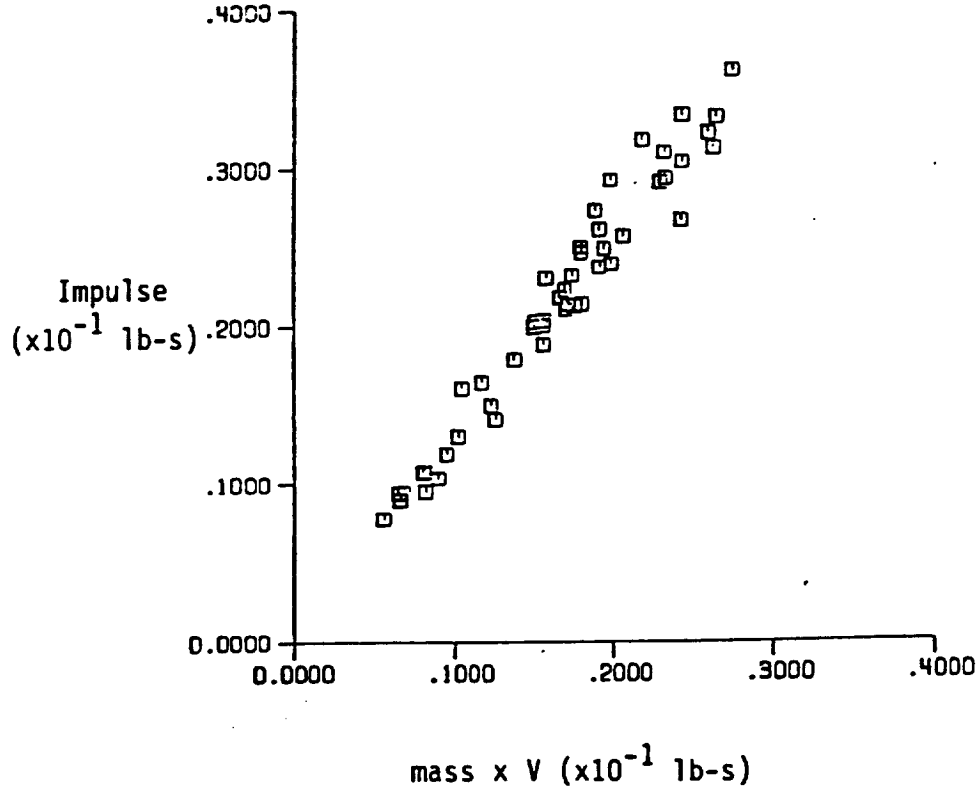

Figure 4.11 Measured Impulse Versus Incident Momentum for Half-Inch Diameter Impactor

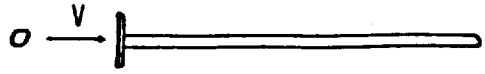

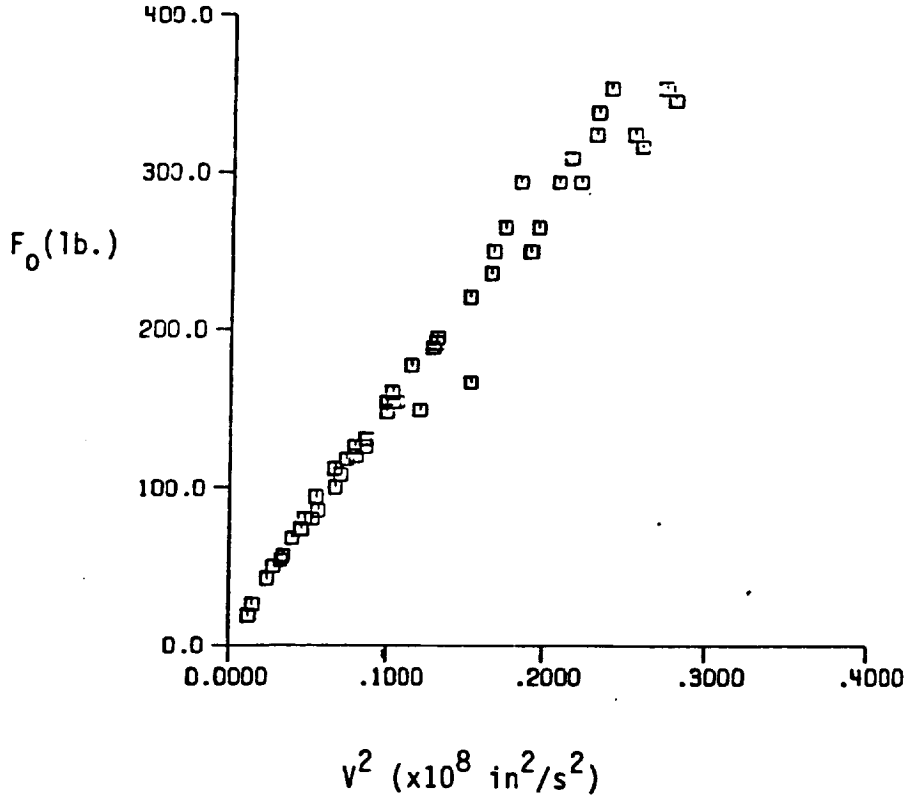

Figure 4.12 Force Amplitude Versus V^2 for 3/8 Inch Diameter Impactor

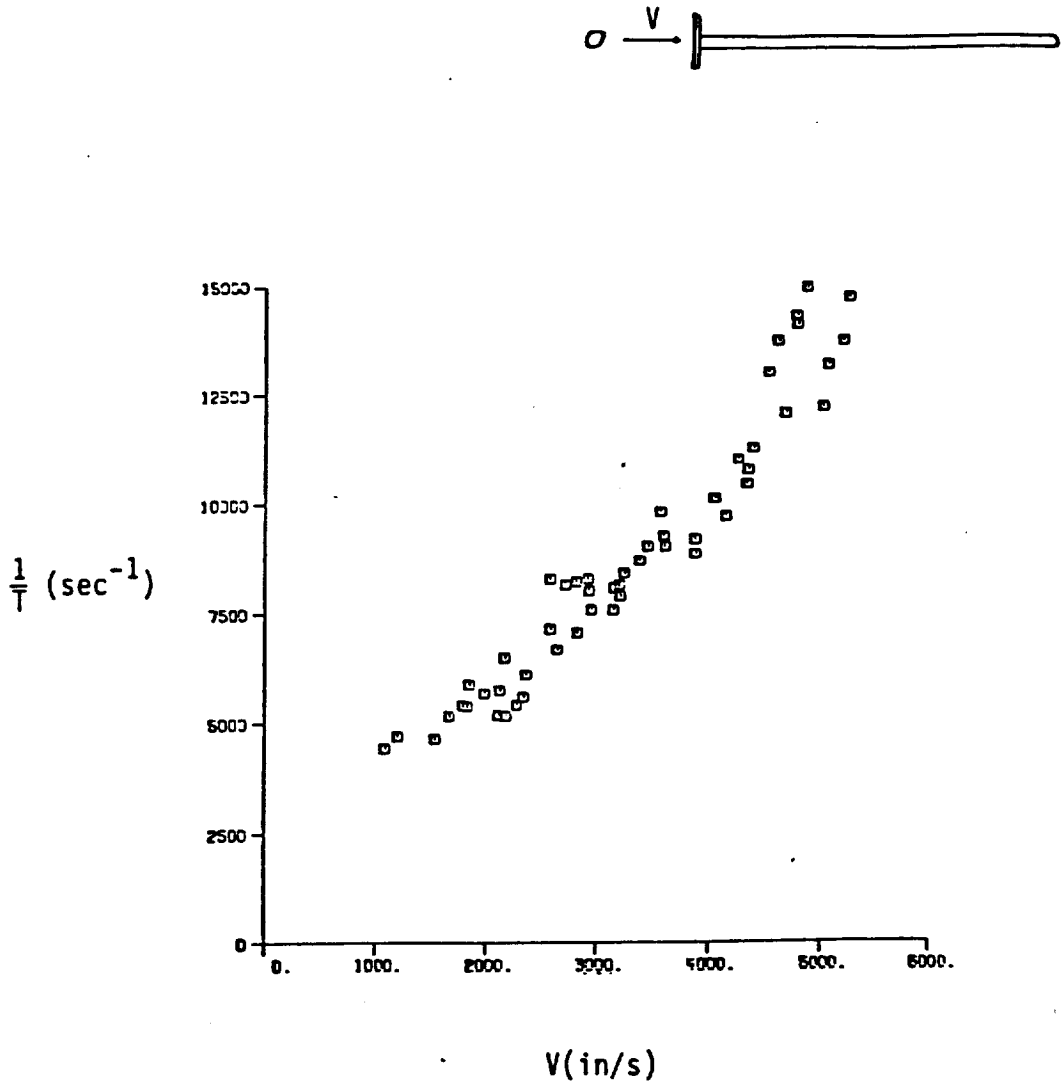

Figure 4.13 Inverse Contact Time Versus Impact Velocity for 3/8 Inch Diameter Impactor

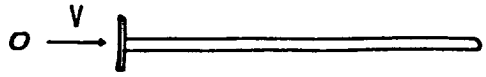

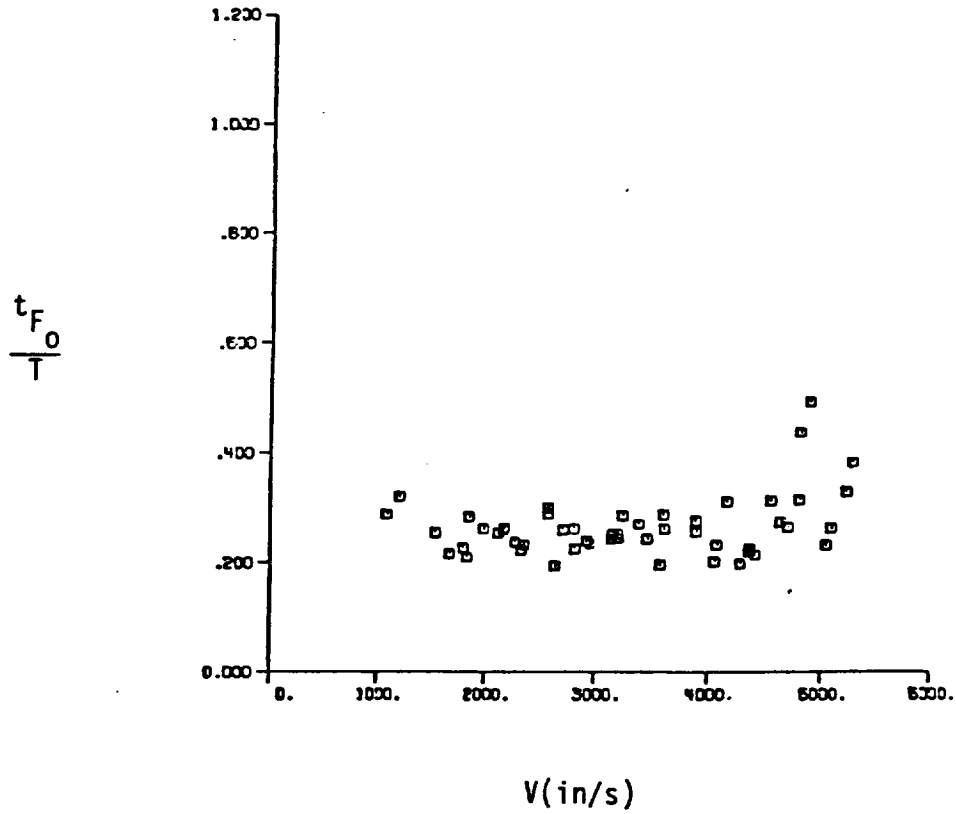

Figure 4.14 t_{F_o}/T Versus Impact Velocity for 3/8 Inch Diameter Impactor

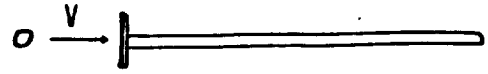

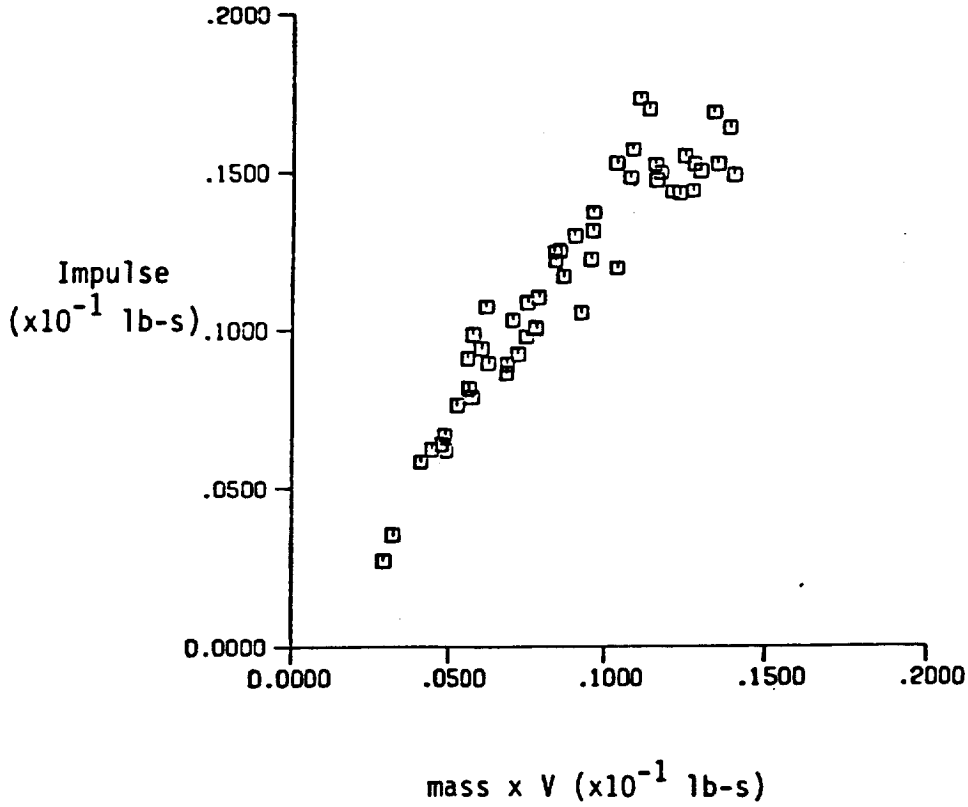

Figure 4.15 Measured Impulse Versus Incident Momentum for 3/8 Inch Diameter Impactor

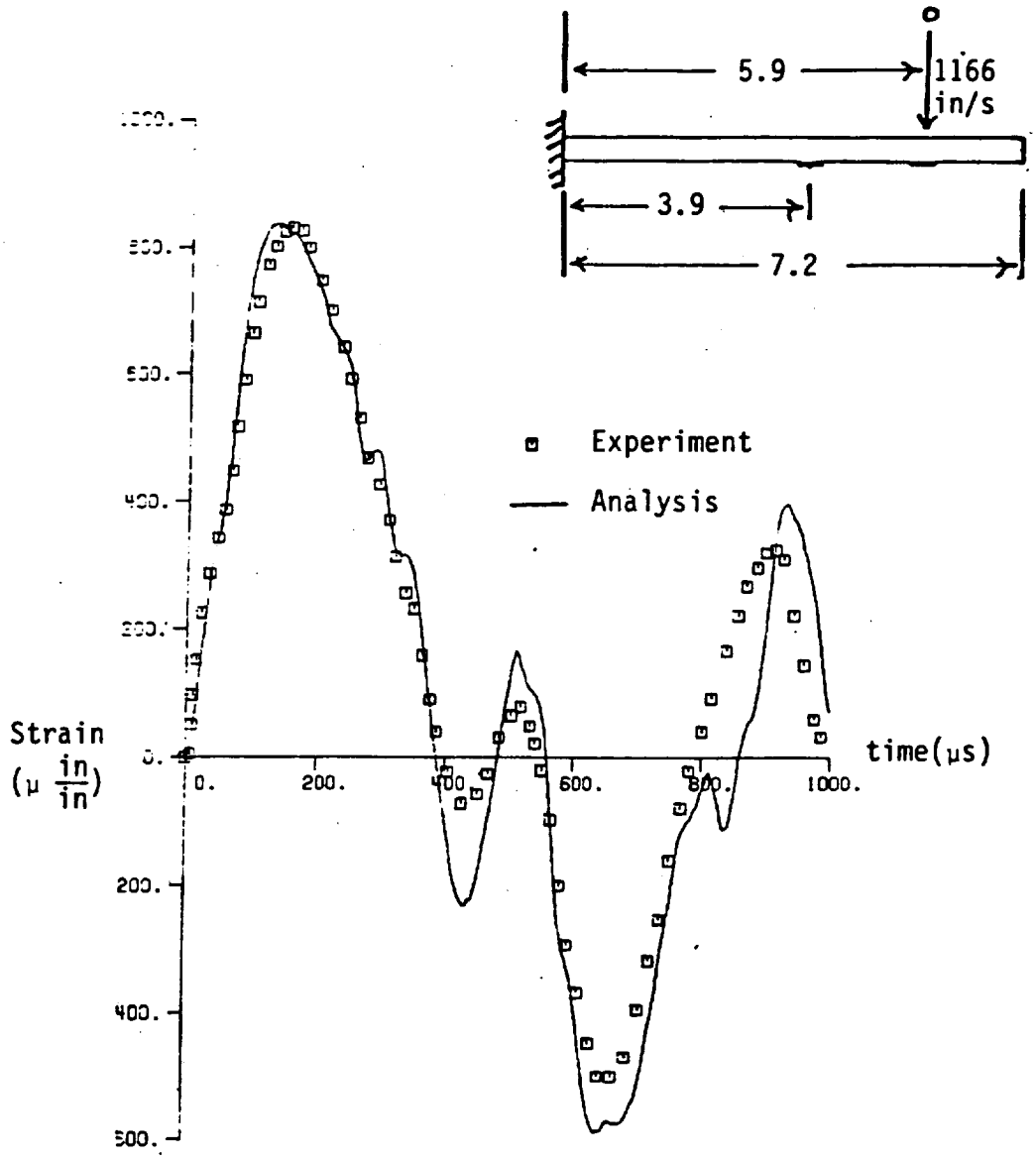

Figure 4.16 Strain History at Gage 1 in Short Beam Specimen Using Force History No. 1.

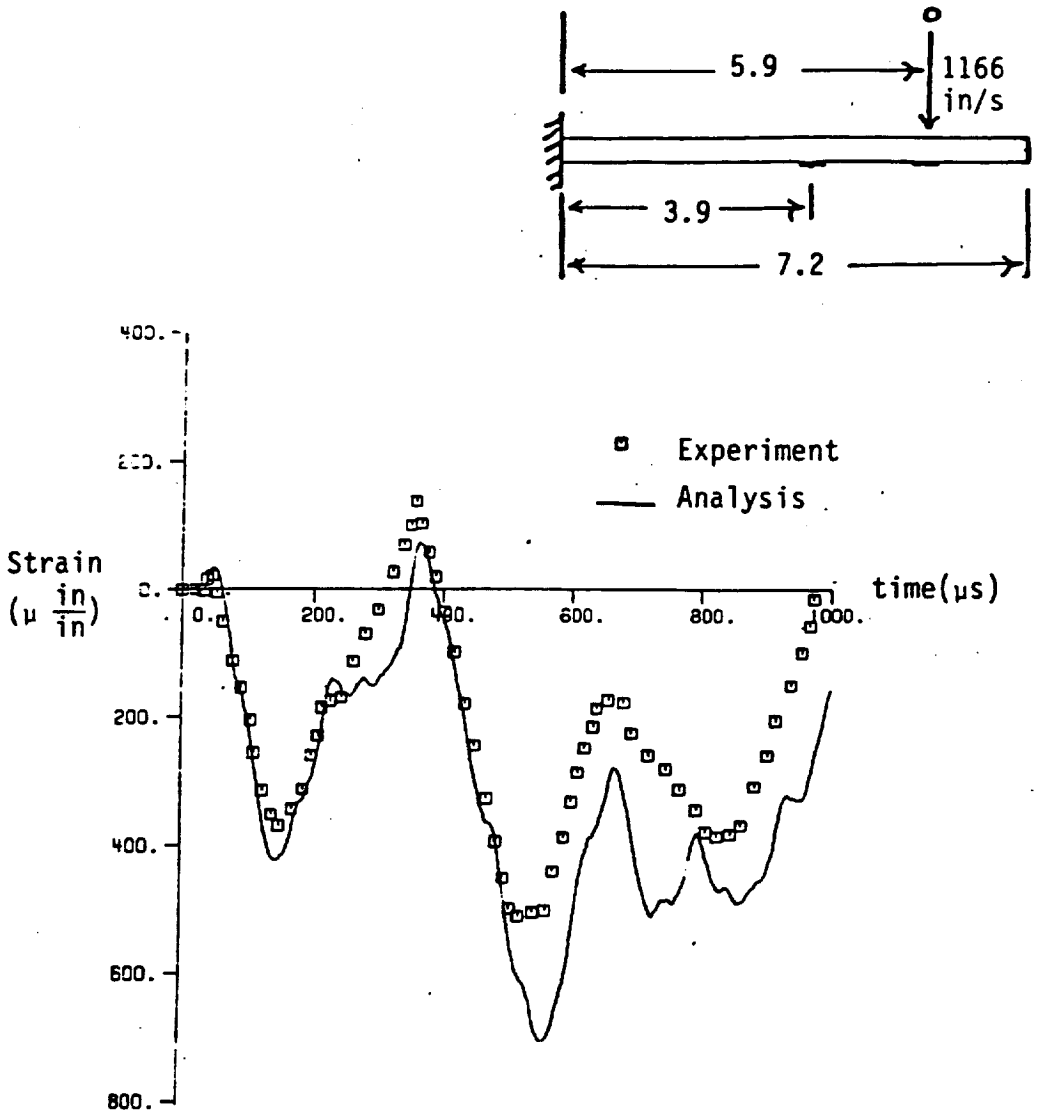

Figure 4.17 Strain History at Gage 2 in Short Beam Specimen Using Force History No. 1.

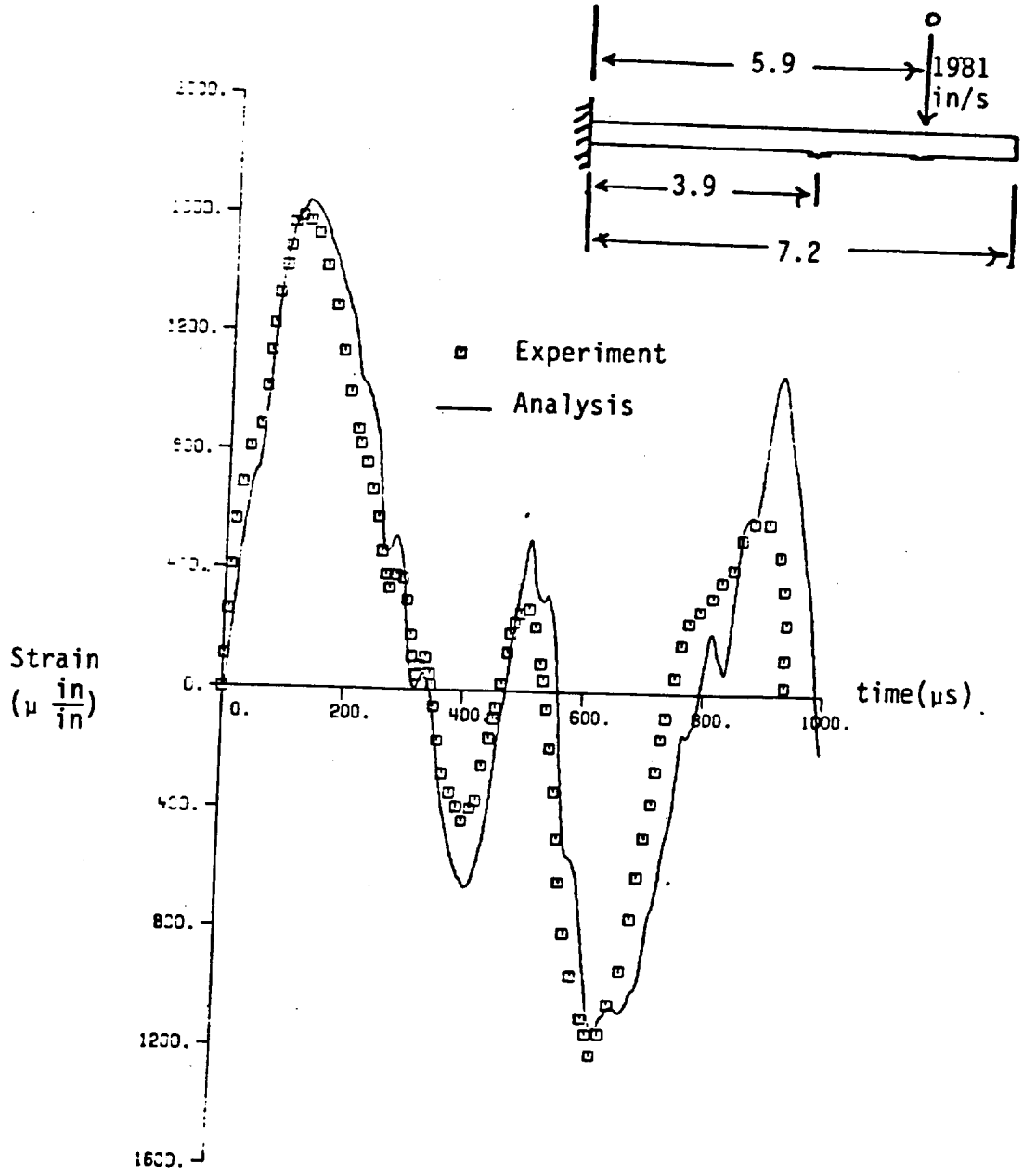

Figure 4.18 Strain History at Gage 1 in Short Beam Specimen Using Force History No. 2.

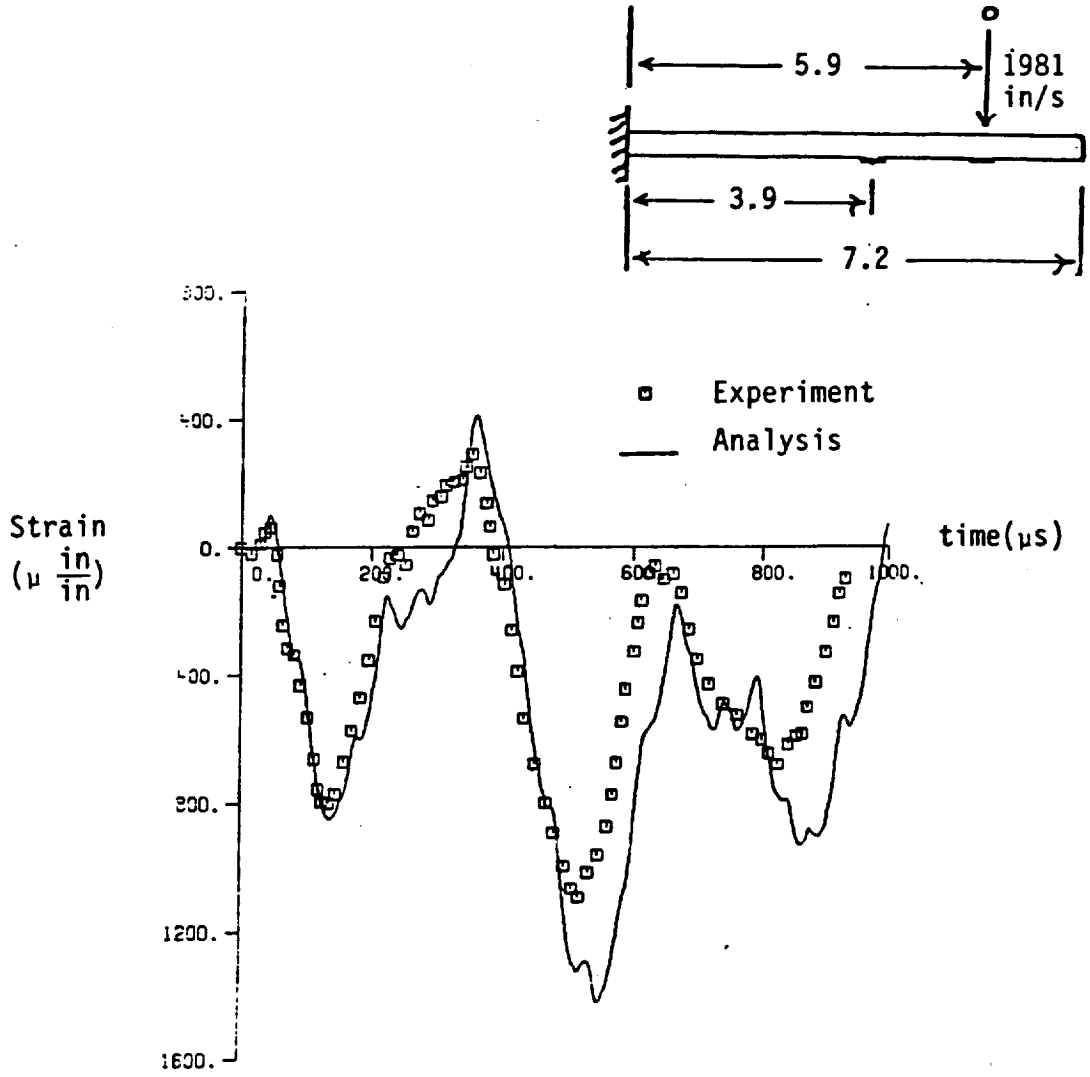

Figure 4.19 Strain History at Gage 2 in Short Beam Specimen Using Force History No. 2.

C-2

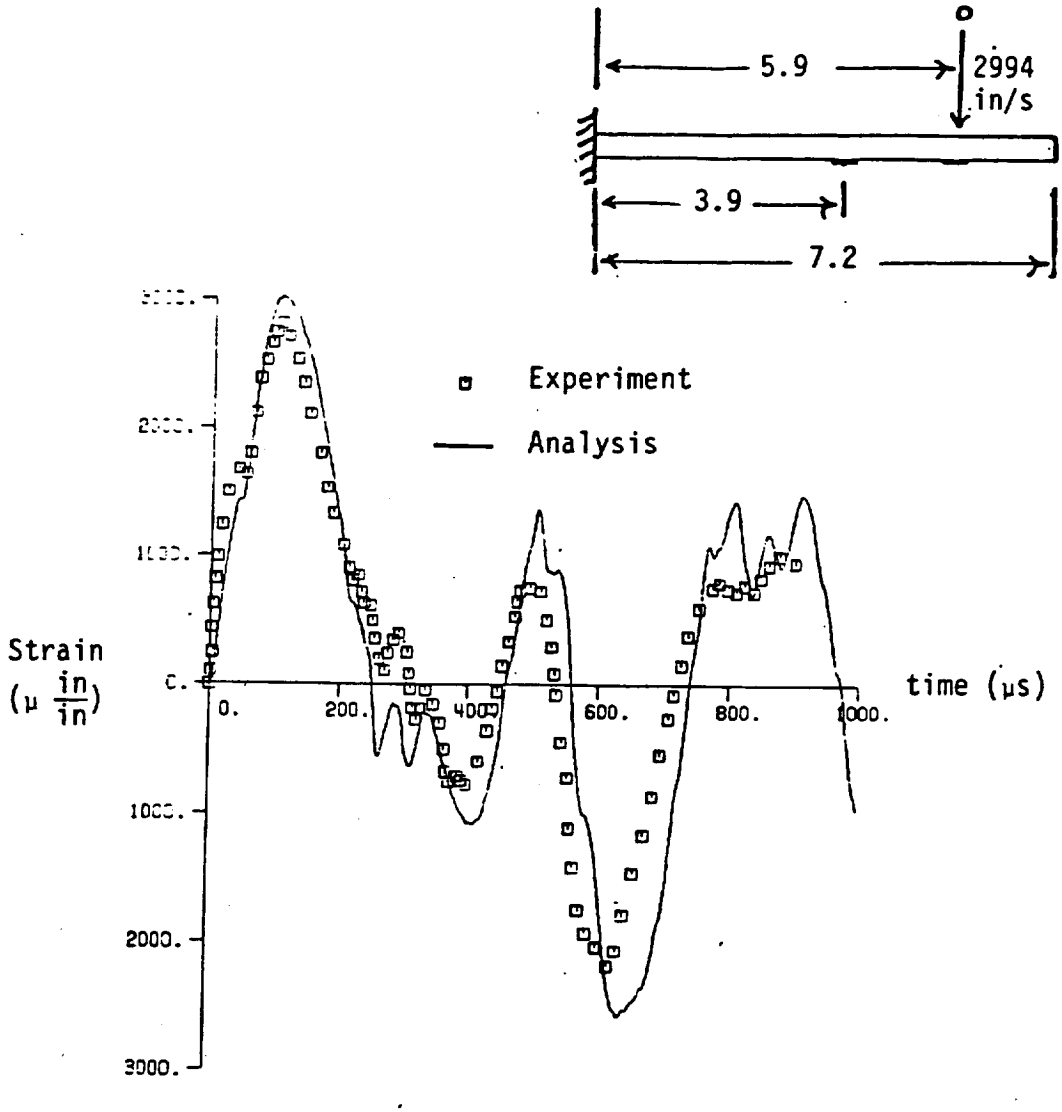

Figure 4.20 Strain History at Gage 1 in Short Beam Specimen Using Force History No. 3.

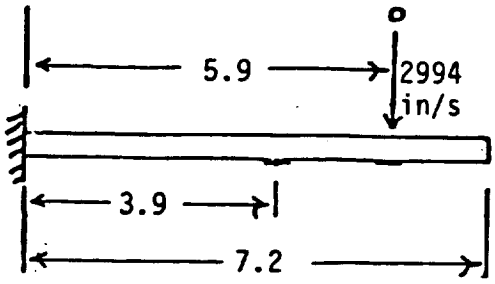

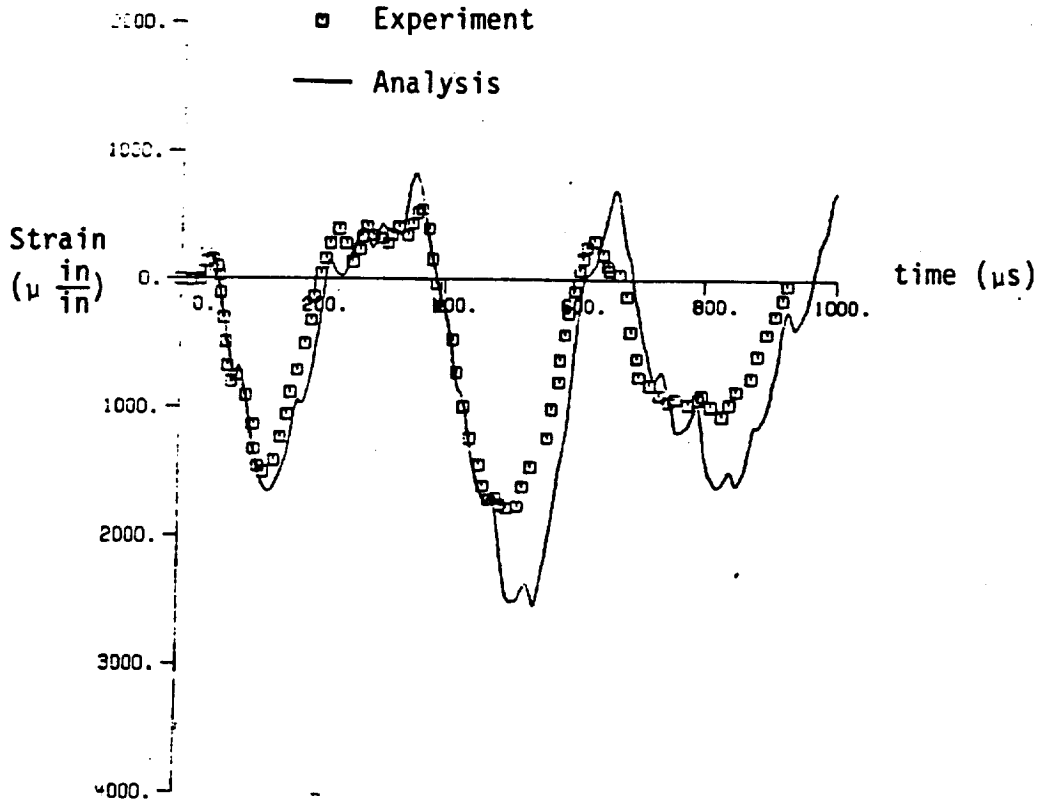

Figure 4.21 Strain History at Gage 2 in Short Beam Specimen Using Force History No. 3.

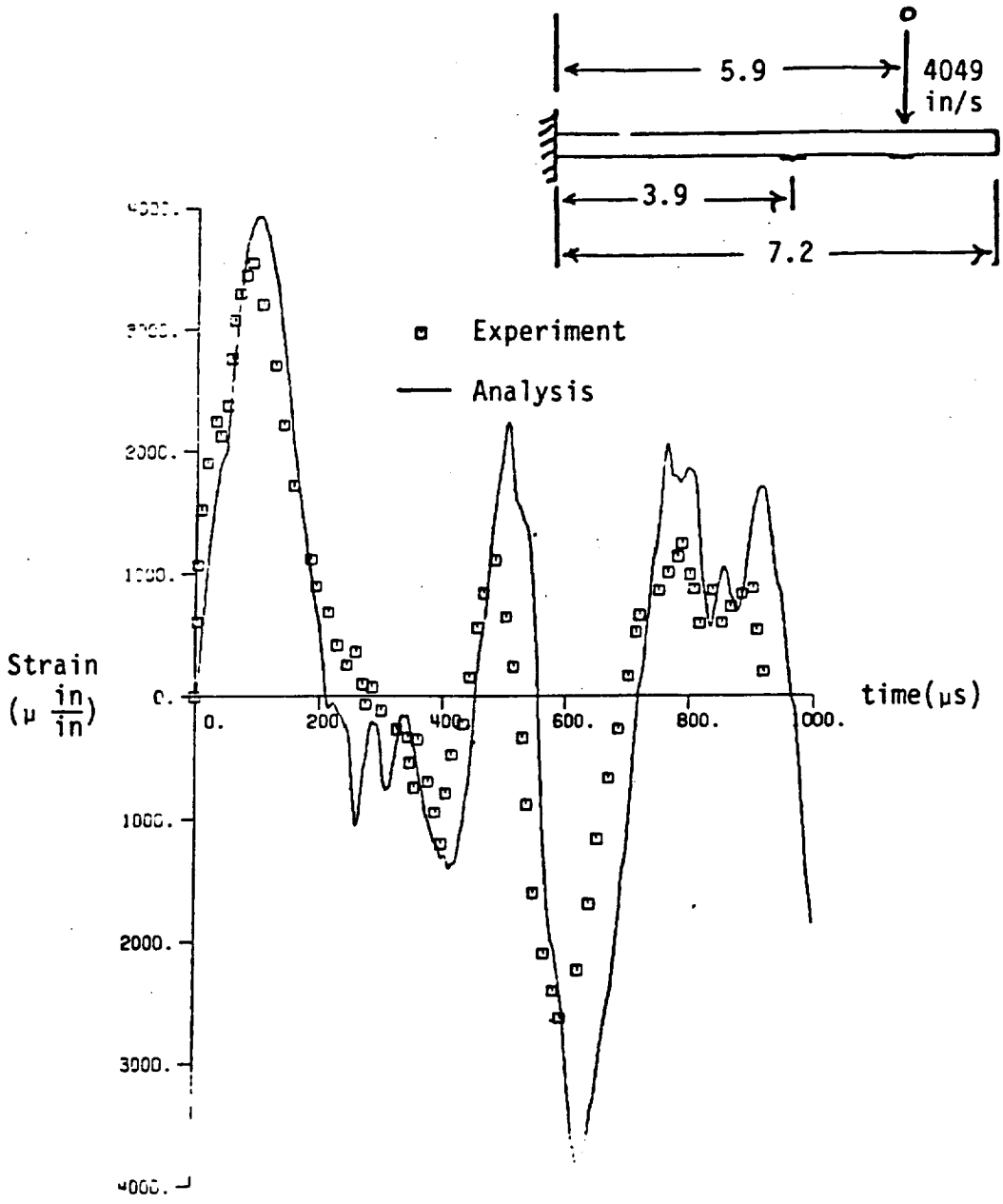

Figure 4.22 Strain History at Gage 1 in Short Beam Specimen Using Force History No. 4.

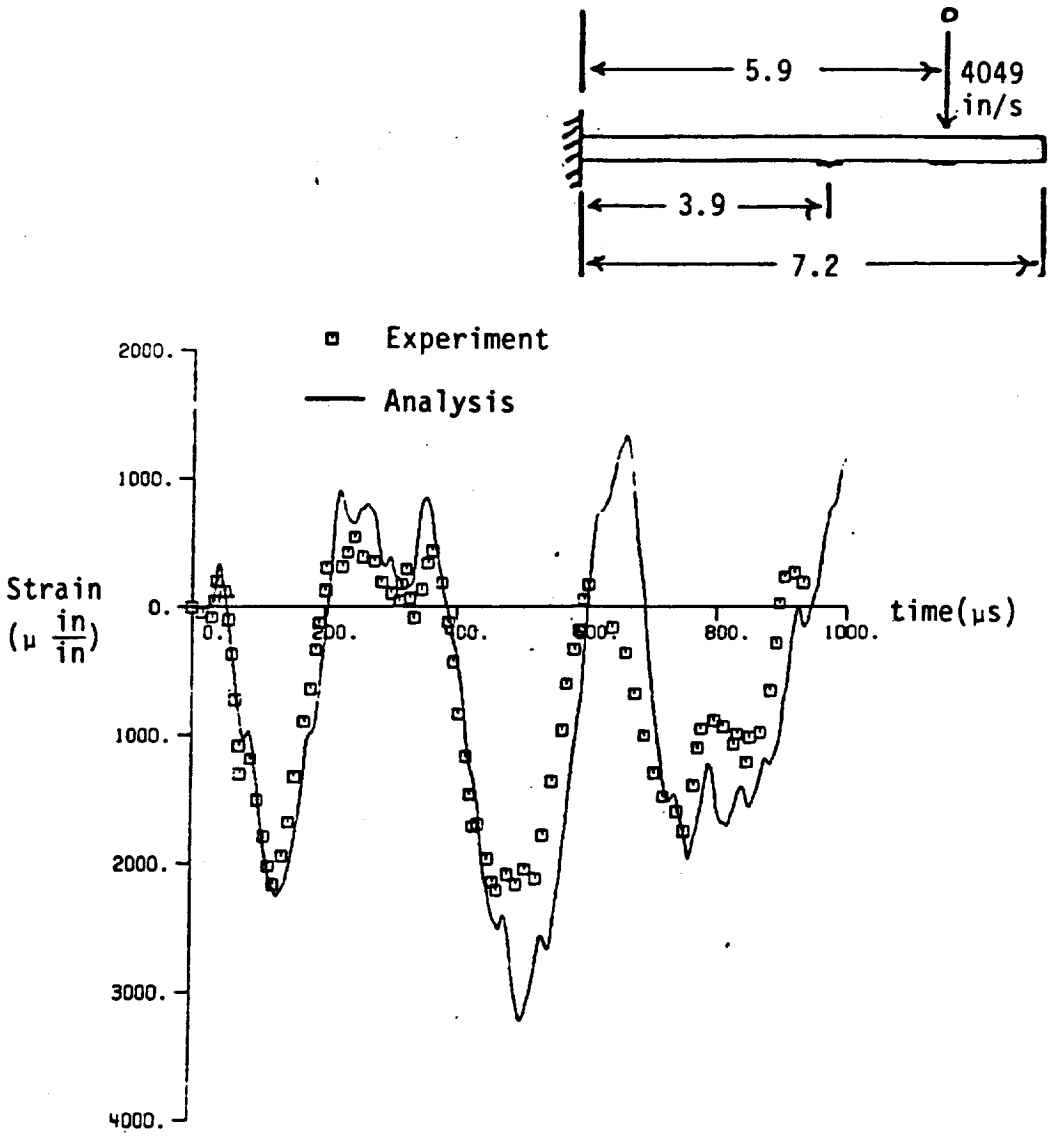

Figure 4.23 Strain History at Gage 2 in Short Beam Specimen Using Force History No. 4.

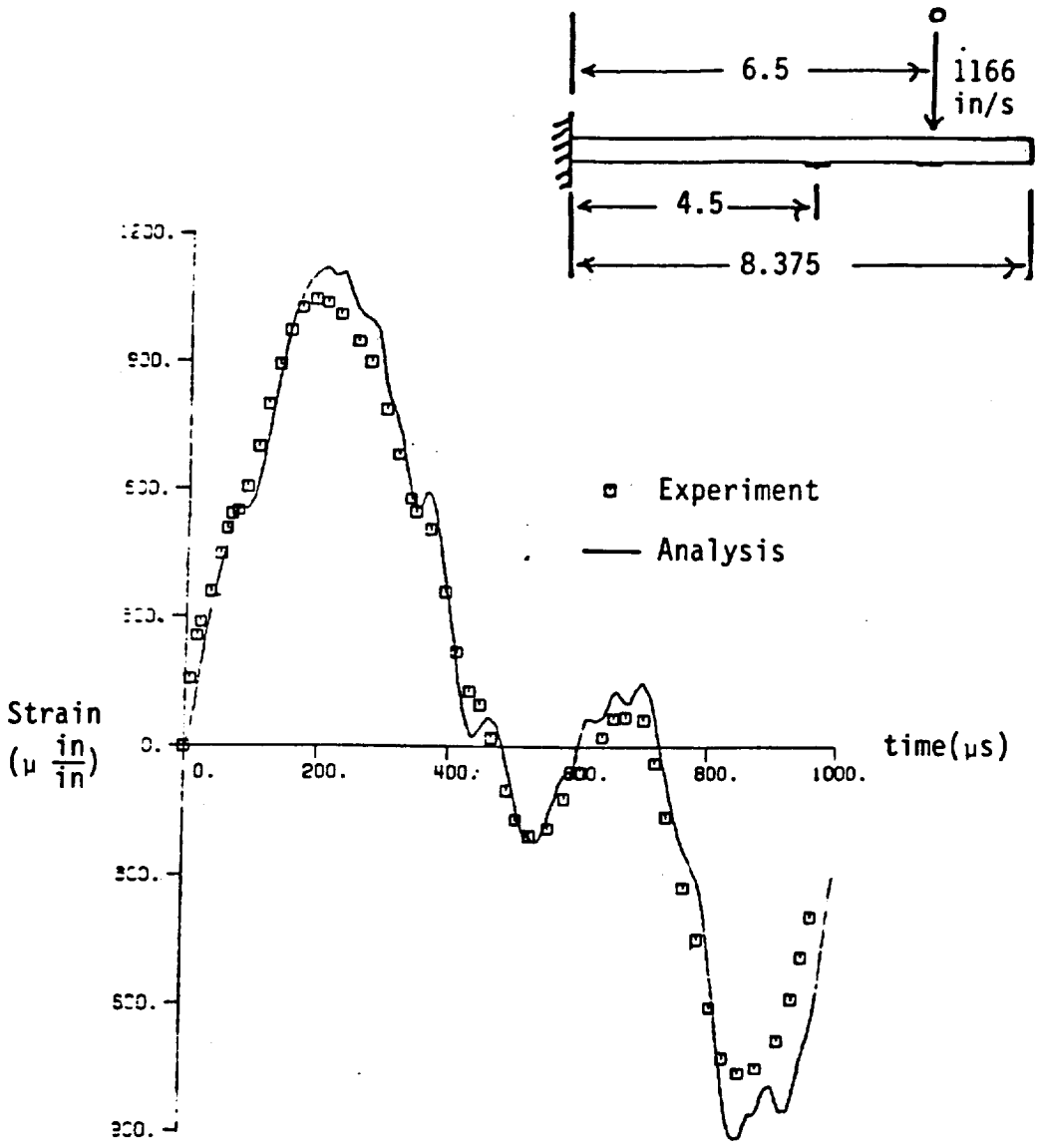

Figure 4.24 Strain History at Gage 1 in Long Beam Specimen Using Force History No. 1.

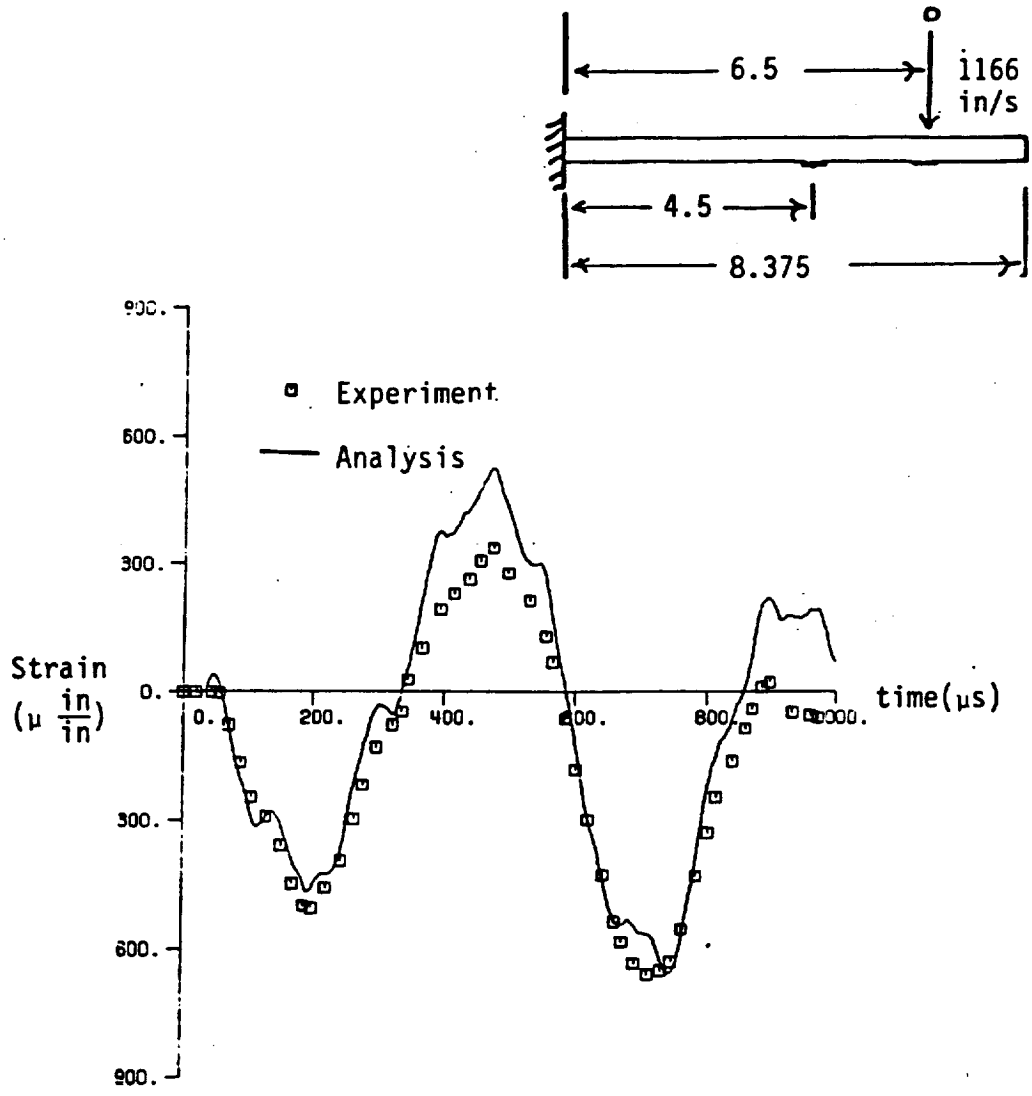

Figure 4.25 Strain History at Gage 1 in Long Beam Specimen Using Force History No. 1.

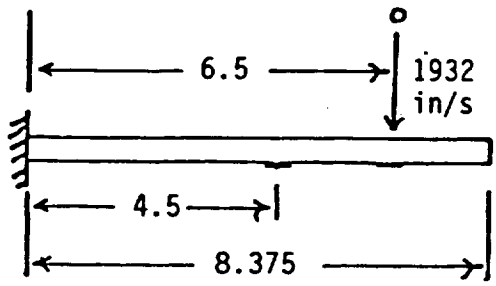

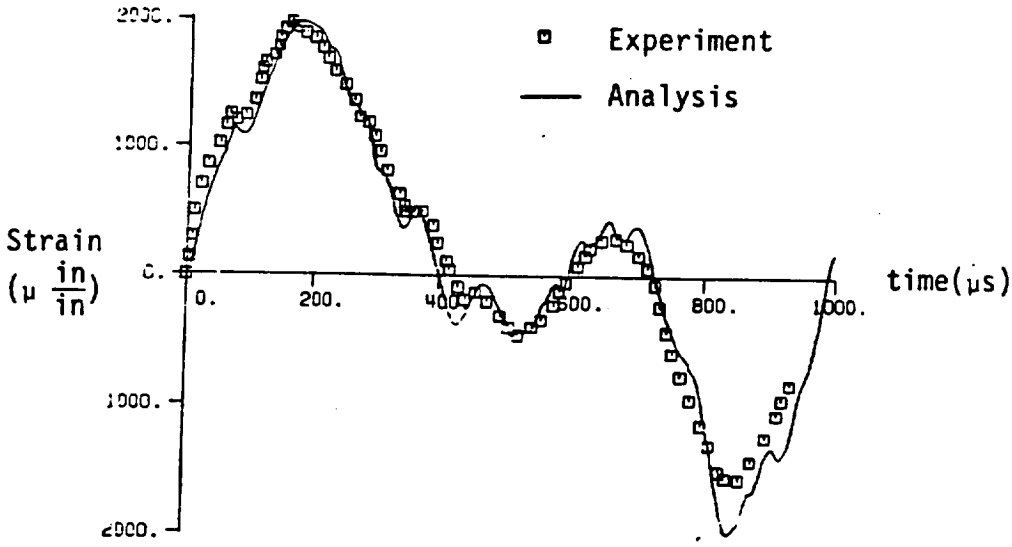

Figure 4.26 Strain History at Gage 1 in Long Beam Specimen Using Force History No. 2.

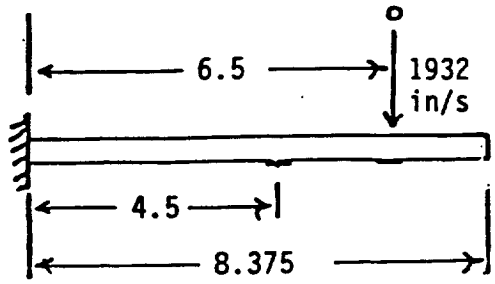

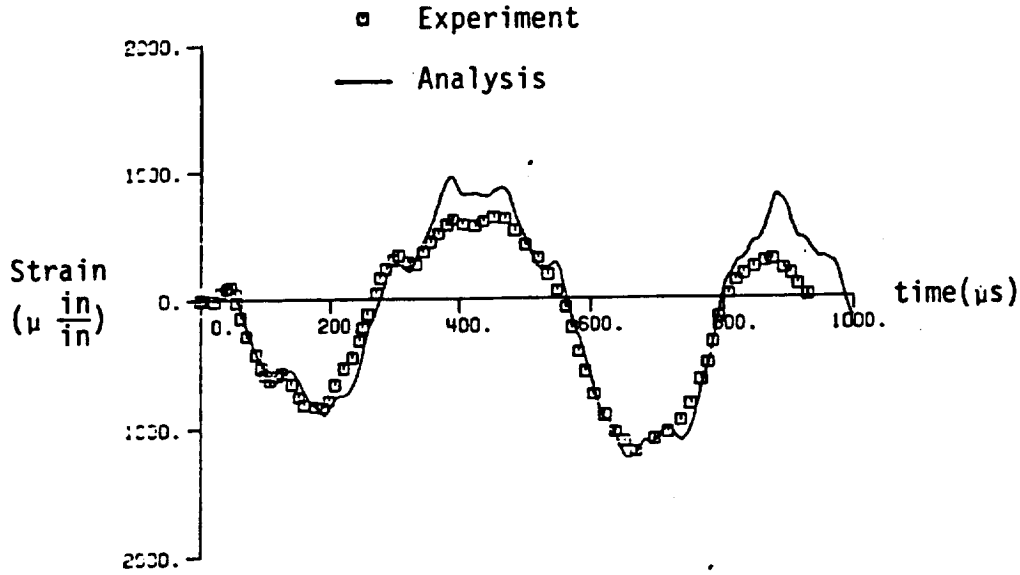

Figure 4.27 Strain History at Gage 2 in Long Beam Specimen Using Force History No. 2.

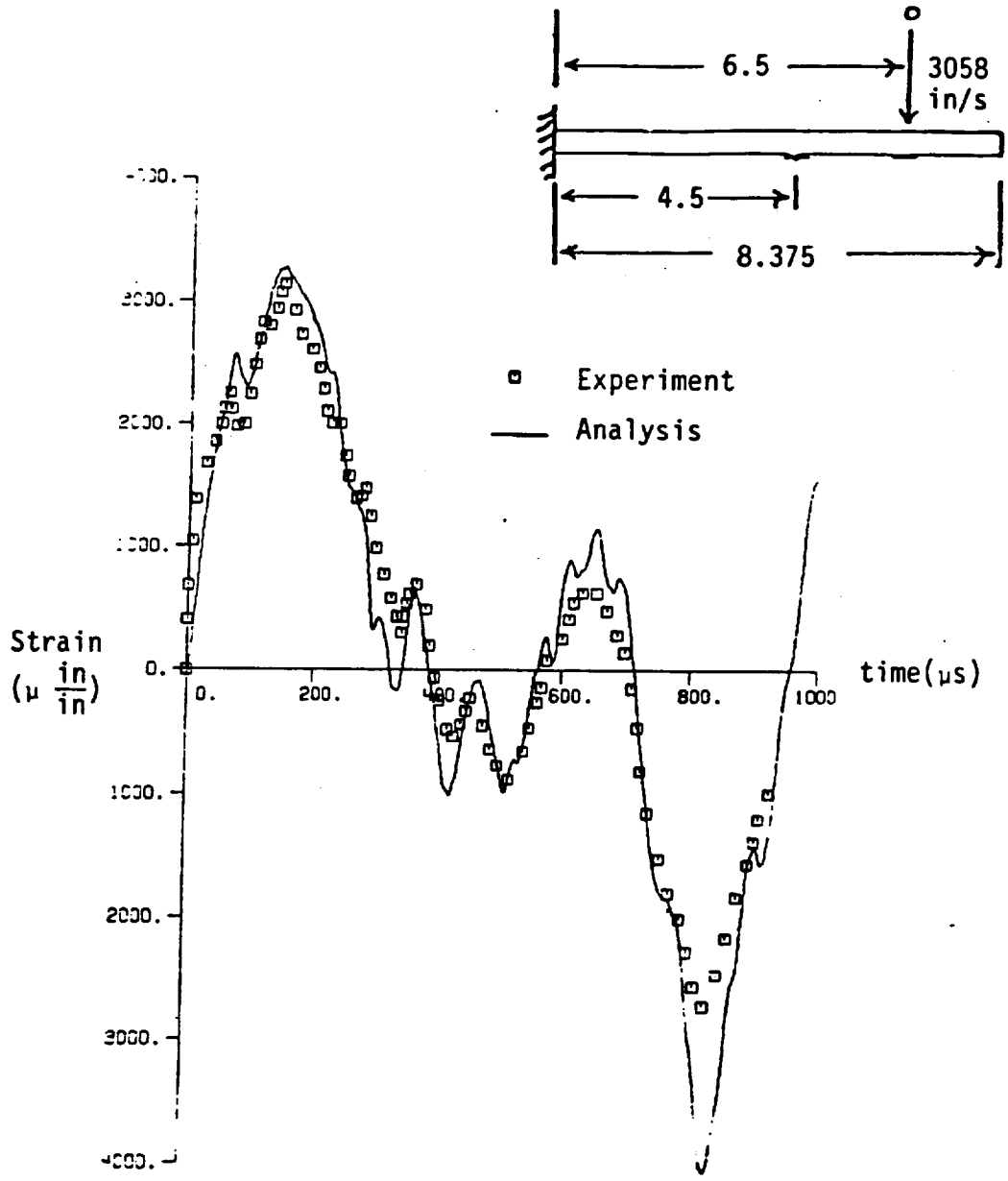

Figure 4.28 Strain History at Gage 1 in Long Beam Specimen Using Force History No. 3.

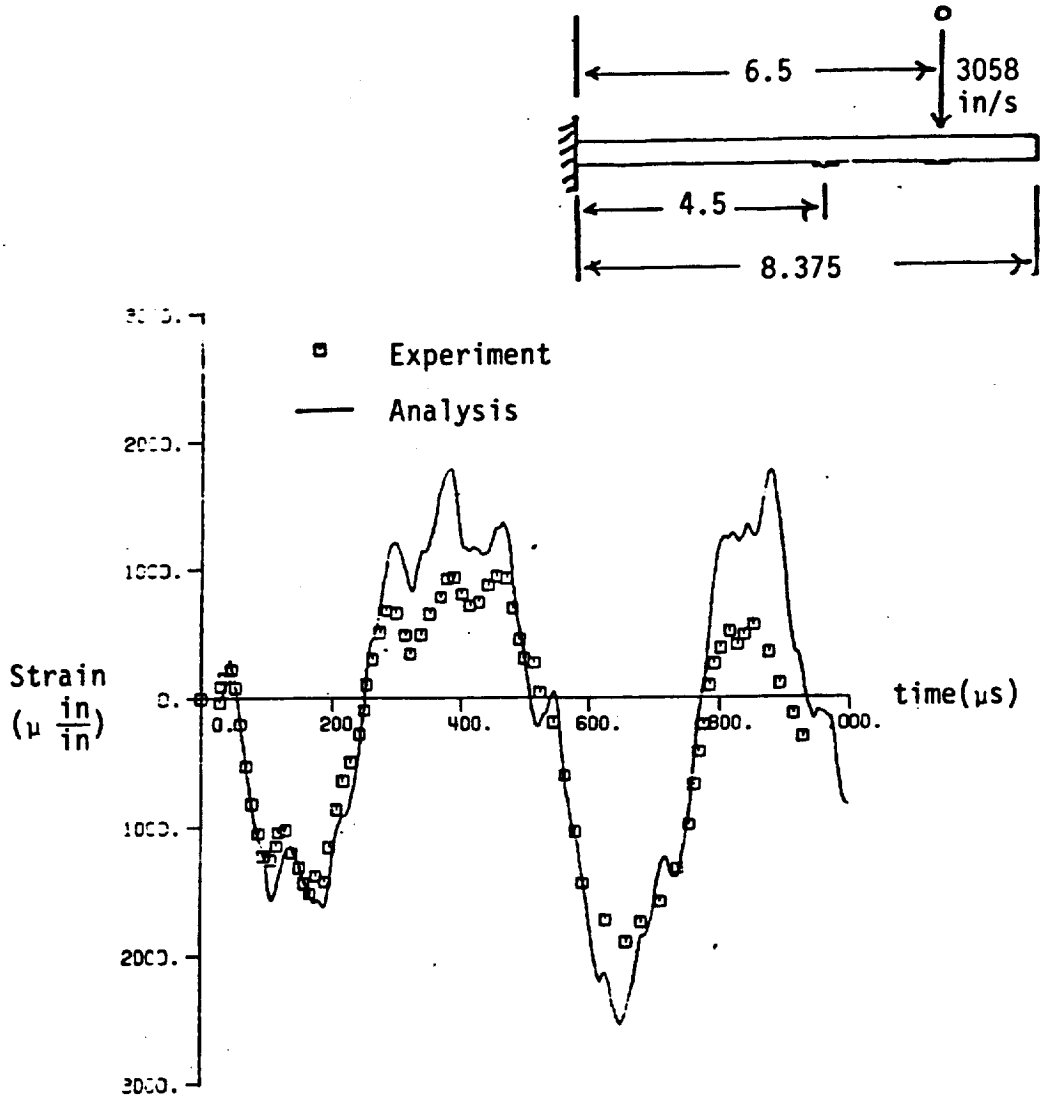

Figure 4.29 Strain History at Gage 2 in Long Beam Specimen Using Force History No. 3.

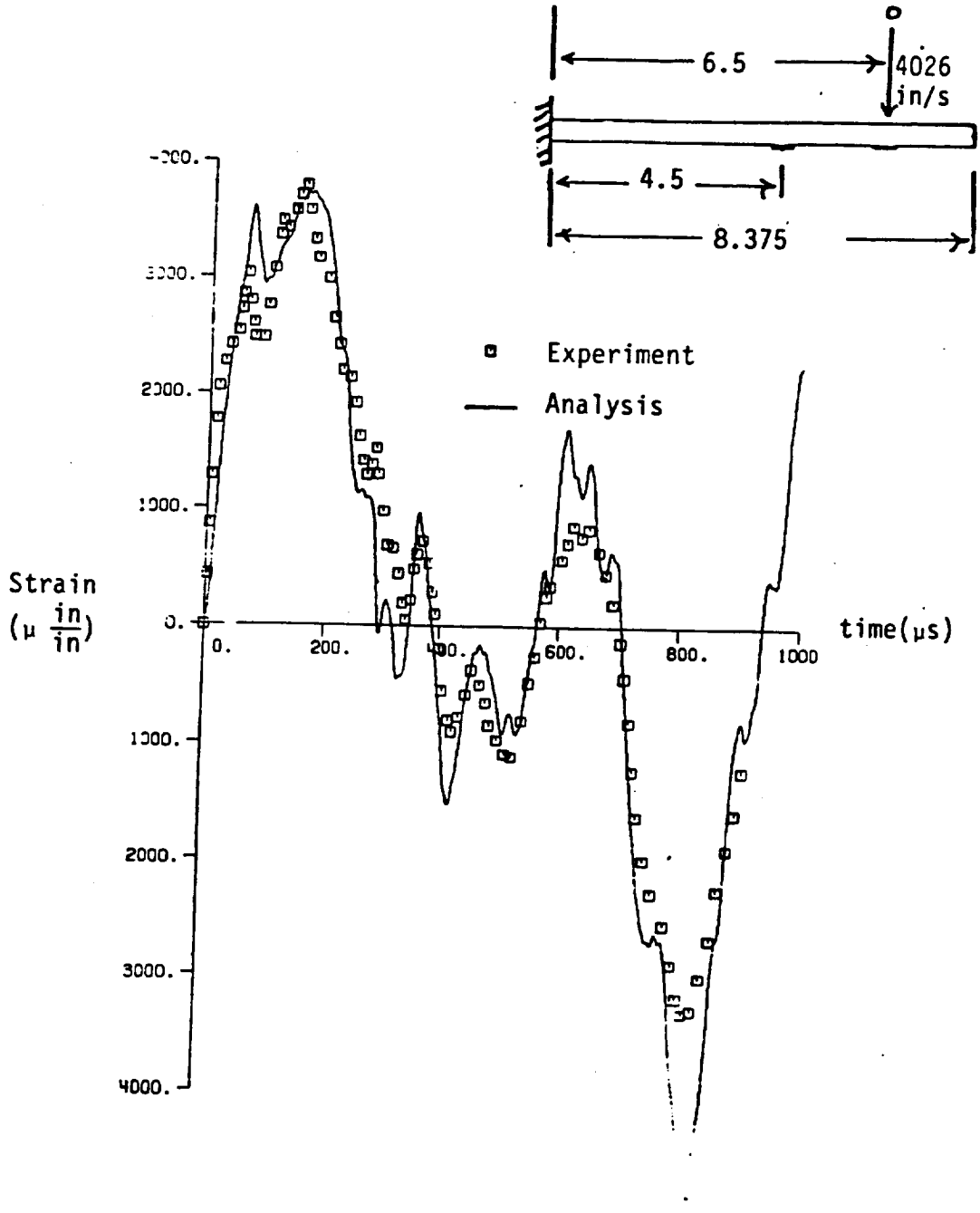

Figure 4.30 Strain History at Gage 1 in Long Beam Specimen Using Force History No. 4.

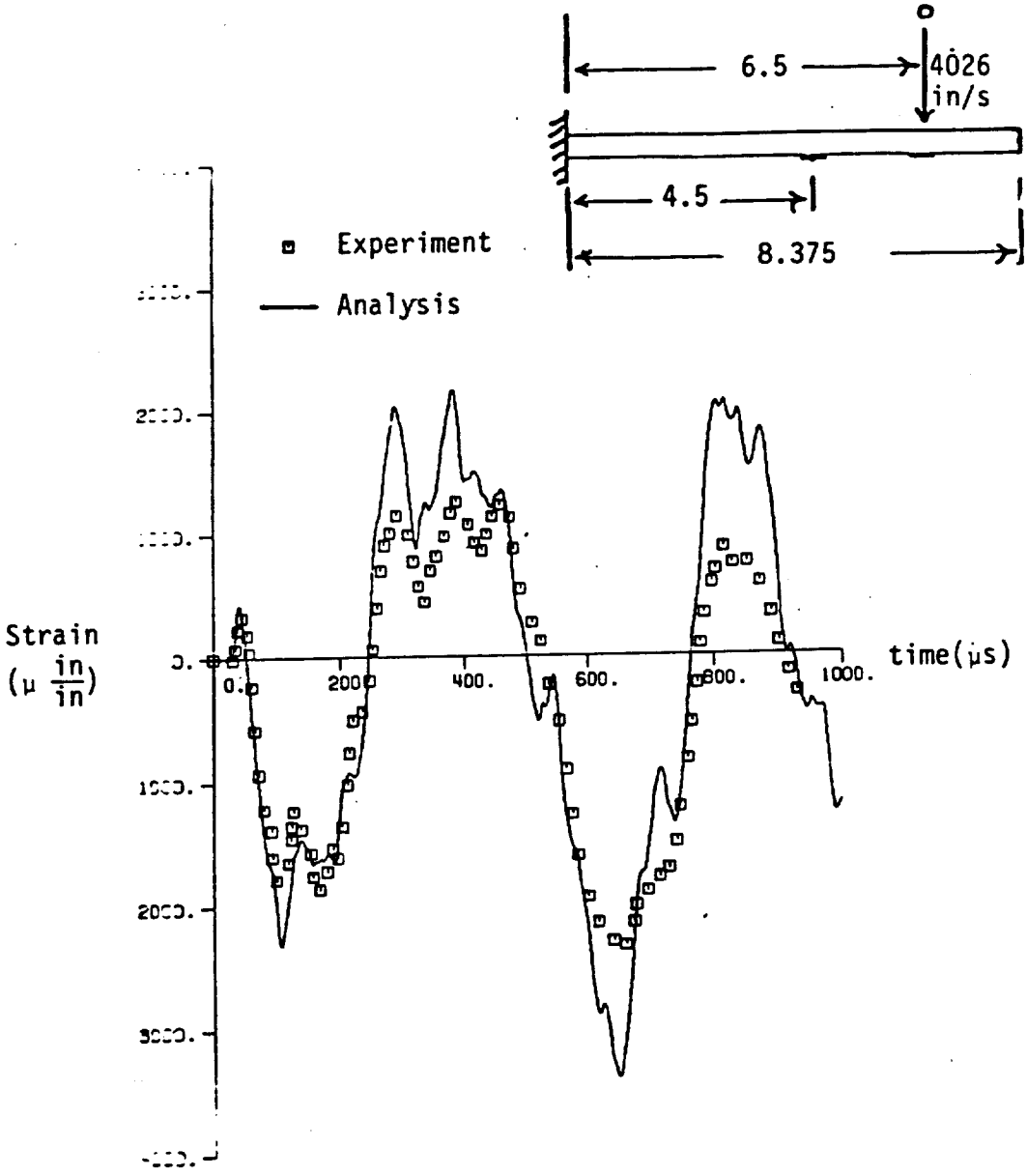

Figure 4.31 Strain History at Gage 2 in Long Beam Specimen Using Force History No. 4.

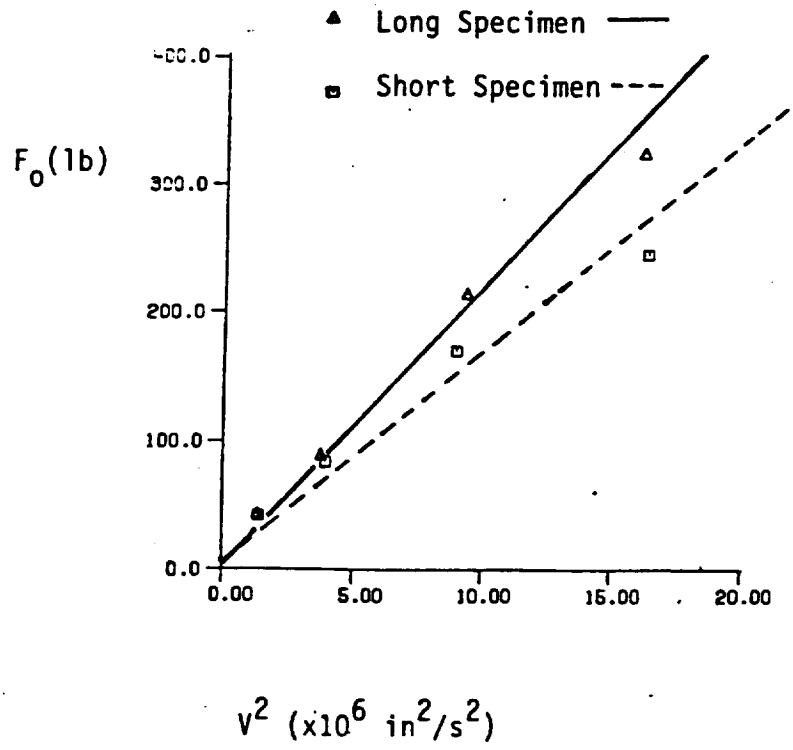

Figure 4.32 Force Amplitude Versus V^2 for Impact on Composite Laminates.

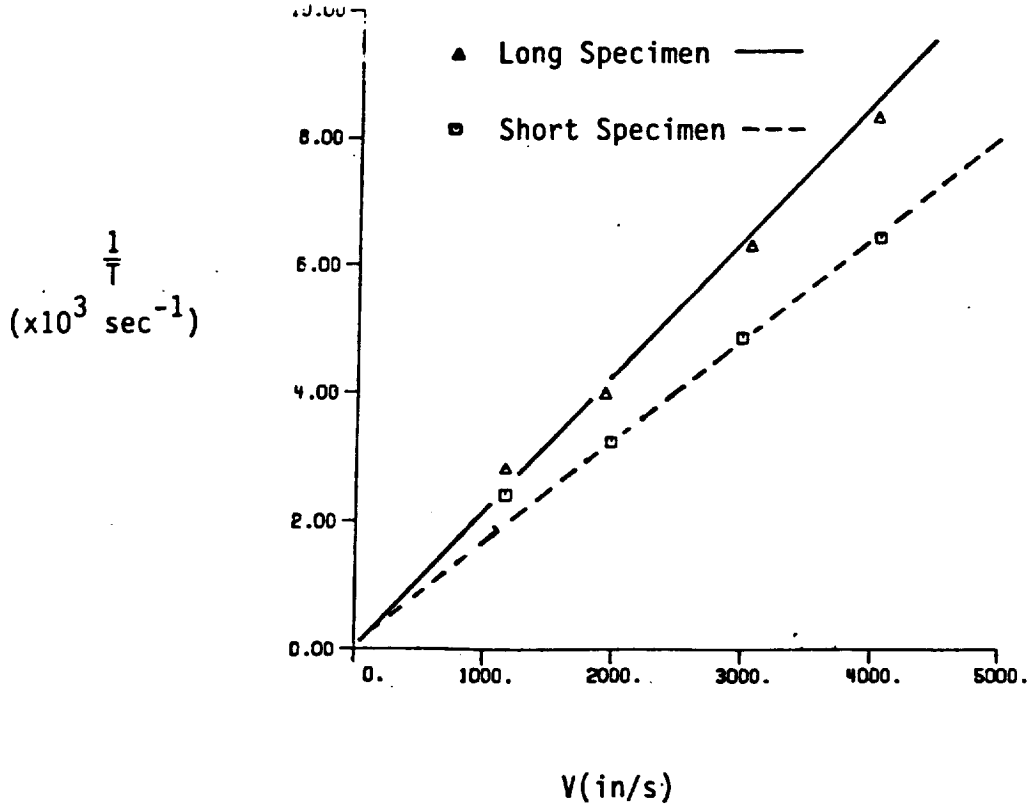

Figure 4.33 Inverse Contact Time Versus Impact Velocity for Impact on Composite Laminates.

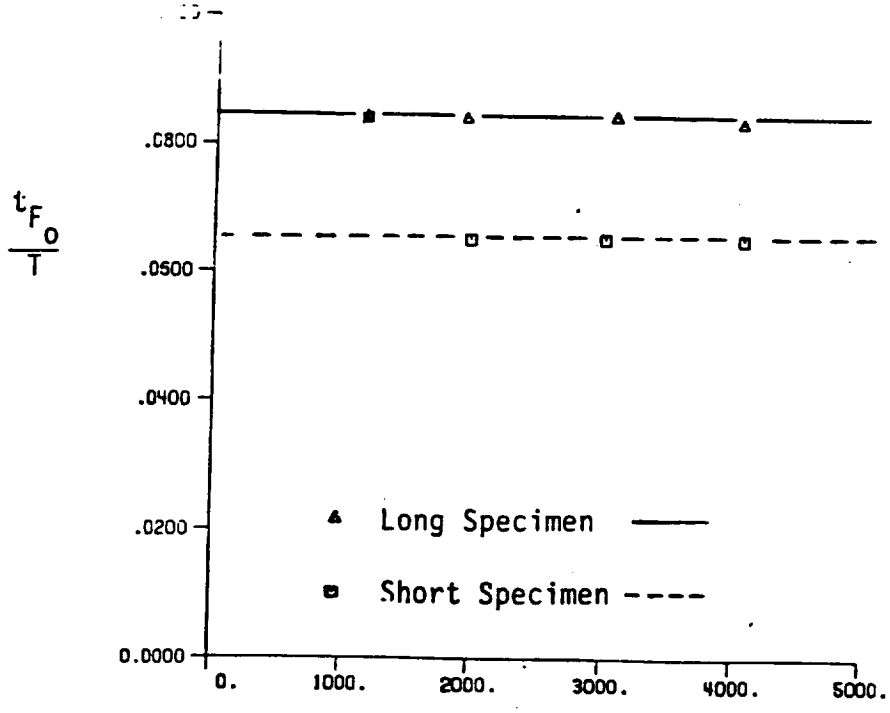

Figure 4.34 t_F /T Versus Impact Velocity for Impact on ^{0}Composite Laminates.

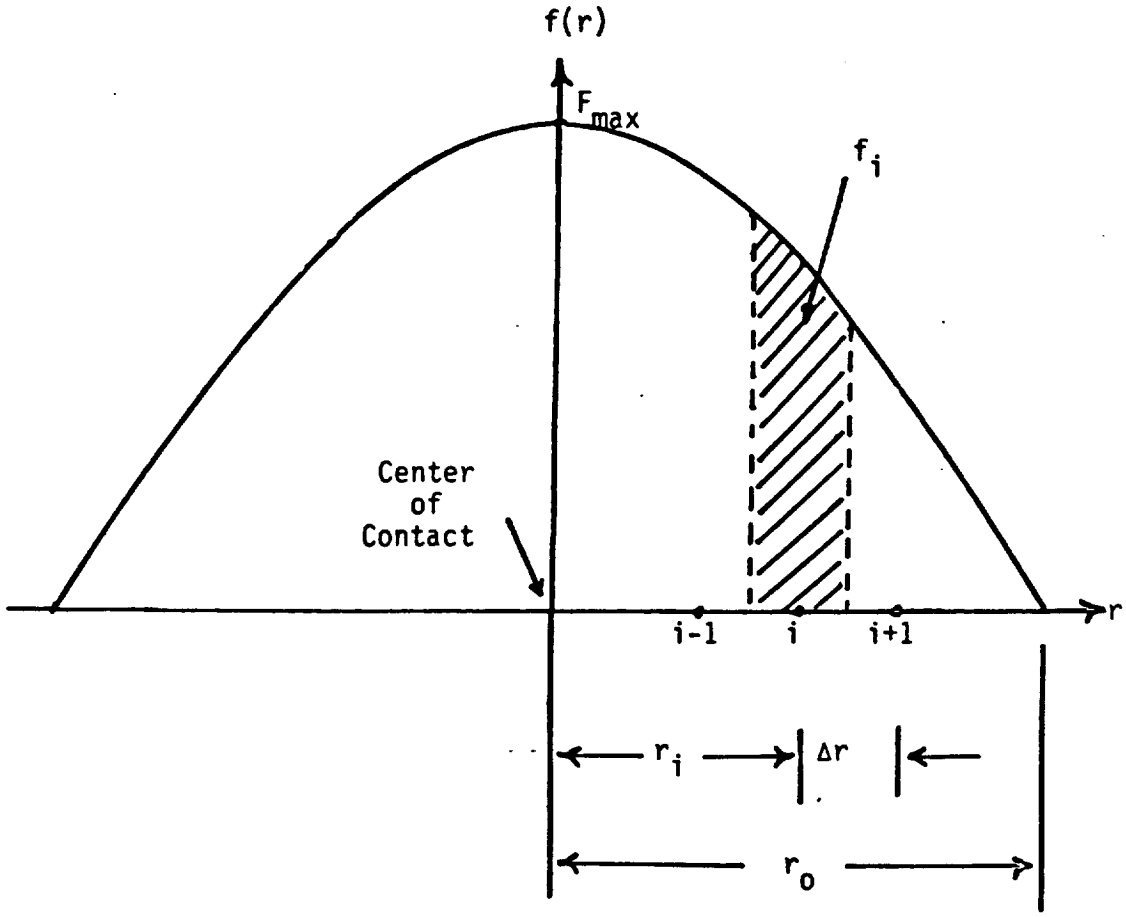

Figure 4.35 Nodal Force Distribution at a Fixed Instant in Time

5. INSTABILITY OF DELAMINATION CRACKS - CRITICAL STRAIN ENERGY RELEASE RATE

Strictly speaking, the impact problem we are concerned with is a three-dimensional problem. However, photographs taken by the high speed camera indicate that the impactor deformation covered almost the whole width of the composite beam specimen. Moreover, due to the small dimension in width, the specimen behaved like a beam except during the initial period of contact. In view of the foregoing, the laminate specimen was approximated as a two-dimensional body and a two-dimensional linear elastic finite program was used to perform the dynamic analysis. The impact load was taken to be uniform across the width of the specimen, and a state of plane strain parallel to the longitudinal cross-section was assumed. This cross-section was then modeled by regular four-node quadrilateral isoparametric finite elements.

5.1 Equivalent Moduli

Ideally, each lamina should be modeled with a number of finite elements to ensure the best accuracy. However, such a procedure would lead to a formidably large number of elements for the 20-plied laminate. For this reason, the $[90/0]_{5s}$ laminate was transformed into an equivalent homogeneous plate with a set of effective moduli obtained by

using appropriate constant strain and constant stress assumptions [43]. The equivalent material properties derived below are used to model the laminate in regions remote from the crack tip.

The material properties for the individual orthotropic lamina are defined relative to the coordinate system shown in Fig. 5.1 and are defined as

$$
\begin{aligned}
E_i &= \text{Young's Modulus in the 'i' direction} \\
&\quad i = 1, 2, 3 \\
G_{ij} &= \text{Shear Modulus in the i-j plane} \qquad G_{ij} = G_{ji} \\
&\quad i, j = 1, 2, 3 \\
\nu_{ij} &= -e_j/e_i \quad \text{for uniaxial stress } \sigma_{ii} = \sigma \\
&\quad \text{all other stresses are zero} \\
&\quad i, j = 1, 2, 3 \text{ and} \\
&\qquad \frac{\nu_{ij}}{E_i} = \frac{\nu_{ji}}{E_j}
\end{aligned}
\tag{5.1}
$$

The equivalent material properties for the [0/90] laminate with reference axes defined as shown in Fig. 5.2 will be given the corresponding notation $\bar{E}_{ij}$, $\bar{G}_{ij}$, and $\bar{\nu}_{ij}$ and are derived as follows.

Assume the laminate in Fig. 5.2 is subjected to a uniaxial stress σ_{11} in the 1-direction, and that it will undergo a resultant uniform extension in the two plies

$$e_{11} = e_{11}^{90} = e_{11}^{0} \tag{5.2}$$

where e_{ii} is the engineering strain in the 'i' direction of the laminate and e_{ii}^{θ} is the engineering strain in the 'i' direction of the θ-oriented ply.

Under this condition, the stress is not the same in both plies. The effective stress for the laminate is given by

$$\sigma_{11} = \frac{\sigma_{11}^{90} A^{90} + \sigma_{11}^{0} A^{0}}{A^{90} + A^{0}} \tag{5.3}$$

where

σ_{ii} is the laminate stress in the 'i' direction

σ_{ii}^{θ} is the stress in the θ-oriented ply in the laminate 'i' direction

and

A^{θ} is the cross sectional area of the θ-oriented ply.

Using the volume fractions

$$V_{90} = \frac{A^{90}}{A^{90} + A^{0}} \qquad V_{o} = \frac{A^{0}}{A^{90} + A^{0}} \tag{5.4}$$

eq. (5.3) can be written

$$\sigma_{11} = \sigma_{11}^{90} V_{90} + \sigma_{11}^{0} V_{0} \tag{5.5}$$

The effective Young's Modulus is defined by

$$\bar{E}_1 = \sigma_{11}/e_{11} \tag{5.6}$$

since

$$\sigma_{11}^{90} = E_2 e_{11}^{90} = E_2 e_{11} \tag{5.7}$$

and

$$\sigma_{11}^{0} = E_1 e_{11}^{0} = E_1 e_{11} \tag{5.8}$$

Using eqs. (5.7) and (5.8), eq. (5.5) becomes

$$\sigma_{11} = (E_2 V_{90} + E_1 V_0) e_{11} \tag{5.9}$$

so, from eq. (5.6)

$$\bar{E}_1 = E_2 V_{90} + E_1 V_0 \tag{5.10}$$

in this case, $V_{90} = V_0 = 1/2$, so

$$\bar{E}_1 = \frac{E_1 + E_2}{2} \tag{5.11}$$

for the [0/90] laminate. A similar procedure can be used to show $\bar{E}_2 = \bar{E}_1$.

Assume now that the laminate in Fig. 5.2 is subjected to a constant stress σ_{33} in the 3-direction. Assume

$$\sigma_{33}^{90} = \sigma_{33}^{0} = \sigma_{33} \tag{5.12}$$

Now

$$e_{33}^{90} = \sigma_{33}/E_3 \tag{5.13}$$

and

$$e_{33}^{0} = \sigma_{33}/E_3 \tag{5.14}$$

The strain in the laminate is given by

$$e_{33} = \frac{e_{33}^{90}\, t_{90} + e_{33}^{0} t_0}{t_{90} + t_0} \tag{5.15}$$

where t_0 is the thickness of the θ-oriented ply. Analogous to eq. (5.4), the volume fractions can be defined as

$$V_{90} = \frac{t_{90}}{t_{90} + t_0} \qquad V_o = \frac{t_0}{t_{90} + t_0} \tag{5.16}$$

so eq. (5.15) can be written

$$\begin{aligned} e_{33} &= e_{33}^{90}\, V_{90} + e_{33}^{0}\, V_0 \\ &= \tfrac{1}{2}\,(e_{33}^{90} + e_{33}^{0}) \end{aligned} \tag{5.17}$$

Using eqs. (5.13) and (5.14), eq. (5.17) becomes

$$e_{33} = \sigma_{33}/E_3 = \sigma_{33}/\bar{E}_3 \tag{5.18}$$

so

$$\bar{E}_3 = E_3 \tag{5.19}$$

for the [0/90] laminate.

Assume now that the laminate in Fig. 5.2 is subjected to a shearing stress τ_{13} on the 1-face and oriented in the 3-direction. The shear stress must be continuous at the ply interface, so

$$\tau_{13}^{90} = \tau_{13}^{0} = \tau_{13} \tag{5.20}$$

The shear strains are

$$\gamma_{13}^{90} = \frac{\tau_{13}}{G_{23}} \qquad \gamma_{13}^{0} \frac{\tau_{13}}{G_{13}} \tag{5.21}$$

Defining γ_{13} as the shear strain of the laminate,

$$\gamma_{13} = \frac{\gamma_{13}^{90} t_{90} + \gamma_{13}^{0} t_0}{t_{90} + t_0} \tag{5.22}$$

Using eqs. (5.16), eq. (5.22) becomes

$$\gamma_{13} = \gamma_{13}^{90} V_{90} + \gamma_{13}^{0} V_0 = \frac{1}{2} (\gamma_{13}^{90} + \gamma_{13}^{0}) \tag{5.23}$$

Using eqs. (5.21) and assuming

$$G_{23} = G_{13} \tag{5.24}$$

eq. (5.23) becomes

$$\gamma_{13} = \tau_{13}/G_{13} = \tau_{13}/\bar{G}_{13} \tag{5.25}$$

so

$$\bar{G}_{13} = G_{13} \tag{5.26}$$

for the [0/90] laminate.

Assume now that the laminate in Fig. 5.2 undergoes a uniform strain e_{11} in the 1-direction. Assume

$$e_{11}^{90} = e_{11}^{0} = e_{11} \tag{5.27}$$

The strain in the 90-degree ply is given by

$$e_{33}^{90} = -\nu_{23}\, e_{11} \tag{5.28}$$

and in the 0-degree ply is

$$e_{33}^{0} = -\nu_{13}\, e_{11} \tag{5.29}$$

The laminate strain is

$$e_{33} = \frac{e_{33}^{90}\, t_{90} + e_{33}^{0}\, t_0}{t_{90} + t_0} \tag{5.30}$$

Using eq. (5.16), eq. (5.30) becomes

$$e_{33} = e_{33}^{90} V_{90} + e_{33}^{0} V$$

$$= \frac{1}{2} (e_{33}^{90} + e_{33}^{0})$$

$$= - \frac{1}{2} (\nu_{23} + \nu_{13}) e_{11} \qquad (5.31)$$

Now

$$e_{33} = -\bar{\nu}_{13} e_{11} \qquad (5.32)$$

so

$$\bar{\nu}_{13} = \frac{1}{2} (\nu_{13} + \nu_{23}) \qquad (5.33)$$

for the [0/90] laminate

The mechanical properties of the T300/934 graphite epoxy lamina are given as

$$\begin{aligned} E_1 &= 19.5 \times 10^6 \text{ psi} \\ E_2 &= 1.5 \times 10^6 \text{ psi} \\ G_{12} &= 0.725 \times 10^6 \text{ psi} \\ \nu_{12} &= \nu_{13} = \nu_{23} = 0.33 \end{aligned} \qquad (5.34)$$

In addition it was assumed that

$$G_{23} = G_{13} = G_{12} \qquad (5.35)$$

and $E_3 = E_2$

in the numerical analysis. Corresponding effective Moduli derived previously are

$$\begin{aligned}
&\bar{E}_1 = \bar{E}_2 = 10.5 \times 10^6 \text{ psi} \\
&\bar{E}_3 = 1.5 \times 10^6 \text{ psi} \\
&\bar{G}_{13} = 0.725 \times 10^6 \text{ psi} \\
&\bar{\nu}_{13} = \bar{\nu}_{23} = 0.33 \text{ , } \bar{\nu}_{12} = .025 \\
&\rho = 1.49 \times 10^{-4} \text{ lb-s}^2/\text{in}^4
\end{aligned} \tag{5.36}$$

These equivalent moduli are used as the elastic constants of the finite elements in regions remote from the crack tip.

5.2 Finite Element Modeling

Four-node quadrilateral isoparametric elements [44] were used to model the composite laminates. A state of plane strain is assumed in the y-z plane so the displacement field is given by

$$\begin{aligned}
v &= v(y, z) \\
w &= w(y, z)
\end{aligned} \tag{5.37}$$

In the isoparametric formulation, the element shape functions are used to express the displacement field within the element in terms of the nodal displacements

$$v(y, z) = \sum_{i=1}^{4} N_i \, v_i \tag{5.38}$$

and

$$w(y, z) = \sum_{i=1}^{4} N_i w_i$$

where v_i, w_i are the nodal displacements, and N_i are the element shape functions, given by

$$\begin{aligned} N_1 &= \frac{1}{4}(1 - \xi)(1 - \eta) \\ N_2 &= \frac{1}{4}(1 + \xi)(1 - \eta) \\ N_3 &= \frac{1}{4}(1 + \xi)(1 + \eta) \\ N_4 &= \frac{1}{4}(1 - \xi)(1 + \eta) \end{aligned} \tag{5.39}$$

and ξ, η are the curvilinear coordinates used to define the element boundaries.

Using the ξ, η coordinate system, the rectangular coordinates x,y are written in terms of the nodal coordinates as

$$y = \sum_{i=1}^{4} N_i y_i$$

and

$$z = \sum_{i=1}^{4} N_i z_i \tag{5.40}$$

So the coordinates of nodes 1,2,3, and 4 of the quadrilateral element are (-1, -1), (1, -1), (1, 1) (-1, 1) respectively, when written in terms of the curvilinear coordinates (ξ, η).

The effective elastic constants calculated in Section 5.1 were used as the material properties of the finite elements in regions remote from the crack tip. The through-thickness distribution of elements used in the remote regions is shown in Fig. 5.3. The exact material properties given in eqs. (5.34) were used to model the laminate in the region near the crack tip, where an accurate representation of the steep stress gradient is crucial. Figure 5.4 shows the transition from the coarse mesh in the remote regions to the finer mesh near the crack tip. The elements in the central 0.1365 inch long region of the mesh were modeled with the exact single-ply material properties given in eqs. (5.34). The elements outside of this region were assumed to have the effective material properties derived in the previous section.

An accurate finite element representation of the regions remote from the crack tip is necessary to adequately model the motion of the laminate. Therefore, an investigation of the effect that the size of the remote elements has on the calculated response at the crack tip was conducted. For this study, all elements were assumed to have the equivalent material properties calculated earlier. Thus, the only effect on the crack tip energy calculation was that due to mesh refinement, not variability in the assumed material representation. In addition, the near tip mesh was relatively coarse, so the system of equations would not become prohibitively large as the remote mesh was refined. For this study, the near tip region was modeled with six elements through the beam thickness, as shown in Fig. 5.3, and an assumed virtual crack extension ratio $\Delta a/a$ of 1/100. Figure 5.5 shows

the effect of remote mesh refinement on the calculated energy release rate. If the mesh is too coarse, the finite element model is excessively stiff, and the energy release rate is over estimated. When the element aspect ratio is reduced to 4:1, the solution has apparently converged. This is indicated by the insignificant change in the calculated solutions for the 4:1 and the finer 2:1 aspect ratios. Therefore, an aspect ratio of 4:1 is considered the maximum allowable value required to accurately model the bending of the beam in regions remote from the crack.

A second convergence study was performed for the mesh near the crack tip. If this mesh is too coarse, the stress gradient near the crack tip will not be adequately represented, and the strain energy release rate calculation will be affected. In this study, the aspect ratio of the remote mesh was kept at 4:1 while successive refinements of the near-tip mesh were performed. Figure 5.6 indicates that the finite element models using 20 and 40 elements through the beam thickness represent the near-tip response with equal accuracy. A small but consistent variation from the solution obtained using the coarsest mesh is evident. The two convergence studies have thus indicated that a finite element mesh with a maximum 4:1 aspect ratio remote from the crack and 20 elements through the beam thickness in the region nearest the crack tip will yield a converged solution for the beam with homogeneous material properties. This mesh convergence will also be assumed valid for the laminated beam.

The quadrilaterial elements were taken to be square near the crack tip. Thus, for the twenty-plied laminate the virtual crack extension

Δa used in the energy release rate calculation and assumed equal to one near-tip element length [25], is equal to the thickness of one lamina, approximately .005 inch.

Newmark's implicit time integration scheme [45] was used to numerically integrate the equations of motion. For the choice of parameters used in the integration, $\gamma = 0.5$ and $\beta = 0.25$, this method is also known as the "Constant Average Acceleration" method, and is unconditionally stable for linear problems. Thus, a relatively large time step, $\Delta t = 2.5$ μsec, could be used to obtain a converged solution.

The three-parameter model of the impact force history, discussed in the previous chapter, was used in the following analyses of the cracked laminates. The particular parameters used for these cases were extrapolated from the data in Figs. 4.32-4.34. The force histories for each of the three following analyses are given in Table 5.1.

5.3 Strain Energy Release Rate

Of interest to the present study is finding a parameter that can be used to gage the on-set of dynamic delamination crack propagation. A natural choice is the use of dynamic strain energy release rate G, which can be calculated by using the crack-closure energy given by [24]

$$G = \lim_{\Delta a \to 0} \frac{1}{2\Delta a} \int_0^{\Delta a} (\sigma_{yy} v + \sigma_{xy} u) dx \tag{5.41}$$

in which σ_{yy} and σ_{xy} are evaluated at the original crack size a, and u and v are the near-tip displacements corresponding to the extended

crack of length (a + Δa). Using the finite element method, the integral in eq. (5.41) can be carried out by using discrete nodal forces and displacements. Moreover, if a fine mesh is used, i.e. Δa << a, then crack opening displacements u and v can be approximated by those for crack of length. The finite element mesh near the crack tip of interest is shown schematically in Fig. 5.7. Using the crack closure method of calculating the strain energy release rate [25], the Mode I and Mode II contributions can be calculated separately:

$$G_I = \lim_{\Delta a \to 0} \frac{1}{2\Delta a} \bar{F}_a (v_a - v_b)$$

and (5.42)

$$G_{II} = \lim_{\Delta a \to 0} \frac{1}{2\Delta a} \bar{T}_a (u_a - u_b)$$

where $\bar{T}_a$ and $\bar{F}_a$ are the nodal forces in the u and v directions that are needed to "close" the crack by an amount Δa. For a small enough element length Δa, these can be approximated by T_c and F_c, respectively.

5.3.1 Verification of Crack Closure Method

A centrally cracked rectangular panel of homogeneous isotropic material subjected to a uniform tensile step function loading was analyzed by Chen using a finite difference method [46]. His solution was used in this study to validate the aforementioned finite element method in conjunction with the crack closure energy calculation. To compare with Chen's solution, which was presented in terms of stress intensity factors, the following relation for Mode I fracture

$$G_I(t) = \frac{\kappa+1}{8\mu} K_I^2(t) \tag{5.43}$$

was used. In eq. (5.43), μ is the shear modulus, K_I is the Mode I stress intensity factor and

$$\kappa = \begin{cases} 3 - 4\nu & \text{for plane strain} \\ (3-\nu)/(1+\nu) & \text{for plane stress.} \end{cases} \tag{5.44}$$

This relation can also be applied to stationary cracks under dynamic loading [47].

Figure 5.8 shows the geometry and material constants of the model studied by Chen [46]. Due to symmetry, only a quadrant was modeled. Figure 5.9 shows the histories of the normalized stress intensity factor $\bar{K}_I$, given by

$$\bar{K}_I = \frac{K_I}{P\sqrt{\pi a}} \tag{5.45}$$

obtained by [46] and by the present method.

Three finite element meshes were used. The coarse mesh consists of 99 4-node quadrilateral plane strain elements and 221 degrees of freedom. In the critical area near the crack tip, the mesh size yields a ratio of $\Delta a/a = 1/4$. The finer mesh is composed of 323 elements with 682 degrees of freedom and a near-tip mesh size of $\Delta a/a = 1/16$. The result from the third mesh was found to agree very well with that from the second mesh and thus can be considered a converged solution. The comparison presented in Fig. 5.9 shows that

the present method is quite acceptable.

5.4 Impact Analysis of Cracked Laminates

The threshold impact velocities required to cause crack extension in each of the impact specimen configurations shown in Fig. 3.1 were determined from the data presented in Figs. 3.2-3.7. Finite element analyses were performed to calculate the dynamic strain energy release rate that results from an impact of each specimen configuration at its particular threshold velocity. The force history used in the analyses were determined from linear extrapolations of the data shown in Figs. 4.32-4.34. The parameters obtained are given in Table 5.1. Because each analysis is performed at the threshold impact velocity for the particular specimen configuration, the maximum value of energy release rate reached after impact can be considered to be the critical value of G necessary to cause crack extension. THe maximum values calculated in the following analyses are therefore given in Table 5.1 as estimates of G_c.

Specimen configurations B, G, and H have initial crack lengths of 1.0, 0.5, and 2.0 inches, respectively. The strain energy release rate was calculated at both crack tips for each of these specimens. The results indicate that the crack tip nearest the fixed end always reaches a higher maximum value of energy release rate, and can therefore be considered the "critical crack tip. Experimental evidence that this is indeed the case for specimen configuration C, in which the initial delamination is not on the beam midplane, is presented in Figs. 3.17 and 3.19. In both cases, the crack tip nearest the fixed end extends first. This crack tip must therefore reach the critical energy

release rate before the free-end crack tip. Two notable exceptions to this generality are configurations D and F. An earlier investigation [48] showed that in these two cases, a "peeling" action occurs in which the crack tip nearest the free end extends to the free boundary before the other crack tip moves, causing separation of the specimen. The free-end crack is therefore the critical one in these cases. With the exception of the three cases mentioned earlier, the energy release rate was calculated only at the critical crack tip.

The values of G_c given in Table 5.1 for the different specimen configurations analyzed in Figs. 5.10-5.17 indicate that G_c for the Mode I cracks is considerably lower than that for Mode II. This trend has been clearly identified in experimental work using static loading [9]. The empirical method used to find the impact force for this analysis may have predicted a higher force than actually occurred in the case of the higher impact velocities. The data in Fig. 4.2 begins to deviate slightly from the linear approximation as the impact velocity increases. Therefore, the energy release rate calculations for those specimens impacted at the higher velocities, most notably configuration G, may be less accurate than the other estimates.

As expected from the experimental results, the Mode of crack extension varies as the location of the delamination through the thickness of the laminate is varied. The calculated energy release rates indicate that the initial crack extension for the off-midplane crack geometries involves primarily Mode I action, while the specimens with the initial delamination on the beam midplane undergo only Mode II crack extension. Although there is a small Mode II contribution for

the off-midplane specimens before the peak value is reached, it is insignificant in comparison to Mode I when $G = G_c$. In the analysis of the midplane cracked specimens, the Mode I contribution was always insignificant in comparison to Mode II.

Static measurements of the critical strain energy release rate necessary to cause delamination crack extension in Graphite/Epoxy laminates have been performed by several investigators, with relatively consistent results. O'Brien [8] measured the strain energy release rate at the onset of delamination in tensile tests of $[\pm 30/\pm 30/90/\overline{90}]_s$ laminates. The critical value of G for a delamination at the -30/90 interface was found to be 0.78 in-lb./in^2. This value was then used to predict the onset of delamination in laminates with different layups. The results indicated that G_c may be independent of the ply orientations along the delamination interface. Wilkins [9] used Double Cantilever Beam and Cracked Lap Shear specimens to generate pure Mode I and Mode II cracks. Two different layups were used for both the Mode I and Mode II tests. For the Mode I case, the first ply configuration used was $[0_{12}/D/0_{12}]$ where D represents the initial delamination produced by embedding Kapton film between the two center plies of the 24-ply unidirectionally reinforced laminate. The other layup tested for the Mode I case was $[0_2/90/0_9/\overline{D,\ 90}]_s$ where D, 90 represents the embedded delamination adjacent to a 90 degree ply located on the midplane of the DCB specimen. In the first layup used, the delamination extends along a 0/0 interface and in the second layup, along a 0/90 interface. Two different ply orientations were also tested for the shear specimen. The first was $[0/\pm 45_4/0/D/0/90/0_2]$, so ten plies are on one side of the

delamination and four on the other. In this case the delamination is embedded at a 0/0 interface. The second layup tested was $[0/\pm 45_2 \mp 45_2/0/D/90/0_3]$ so the embedded delamination lies along a 0/90 interface. Critical energy release rate values were found to be 0.5 and 0.8 in-lb./in^2 for the Mode I and Mode II cases, respectively. In addition, the G_c values for each case were nearly the same at the 0/90 and 0/0 interfaces. This is further evidence that G_c may be independent of the ply orientations along the delaminating interface.

It should be expected that the magnitude of the strain energy release rate necessary to cause crack extension in the case of dynamic loading would be higher than that in the static case. This trend was found to be true for steels [14]. The dynamic values of G_c estimated here show a similar relationship to the static values, so in that sense some confidence can be placed in these results.

Table 5.1 Force Histories Used in Analysis of Pre-Cracked Composite Beam Specimens

Configuration	V_*(in/s)	F_o(lb)	t_{F_o} (μs)	T(μs)	r_o(in)	G_c(in-lb/in^2)
A	5568	513	7.2	112	0.4	4.5*
B	5809	558	6.9	108	0.4	10.6
C	4610	352	8.7	136	0.375	2.0*
D	4330	310	9.2	144	0.375	1.9*
E	5590	517	7.2	112	0.4	7.3
F	5500	501	7.3	114	0.4	5.5*
G	9615	1972	4.1	49.4	0.5	16.1*
H	6124	800	6.4	77.1	0.425	14.6

* off-midplane crack

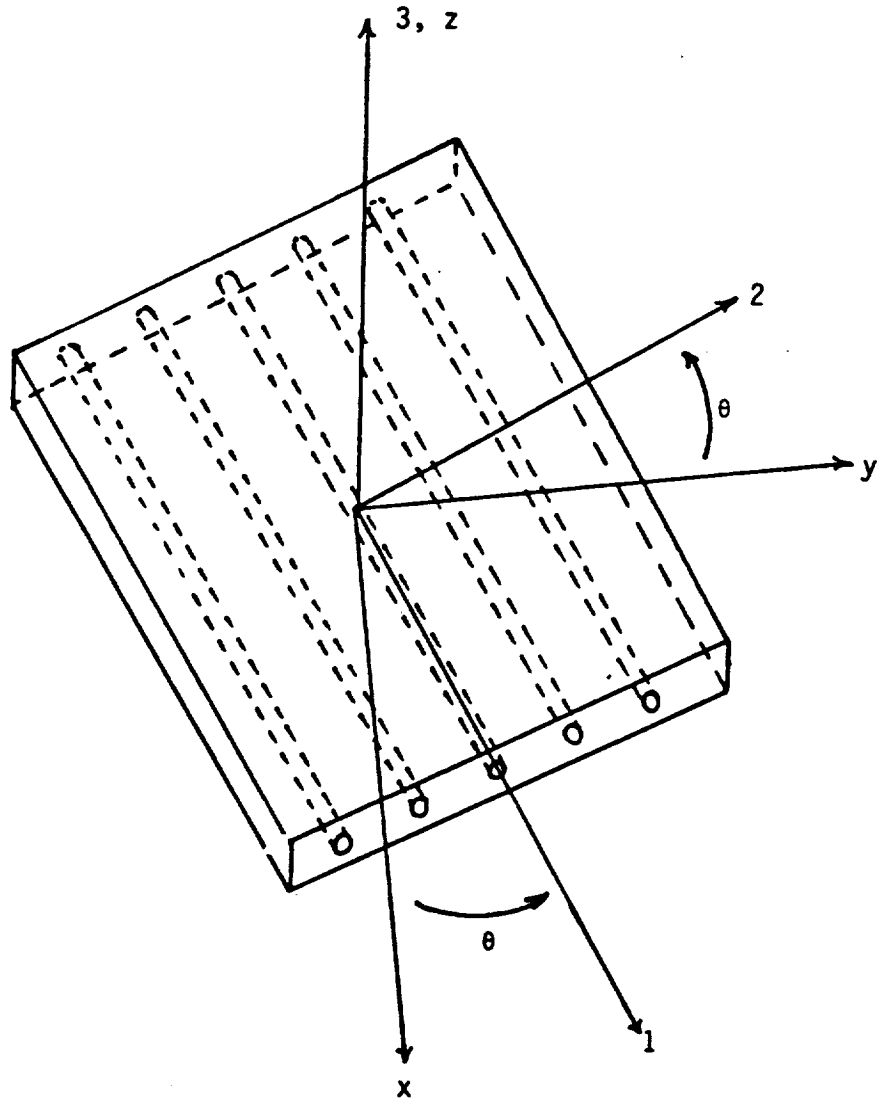

Figure 5.1 Lamina Reference Axes

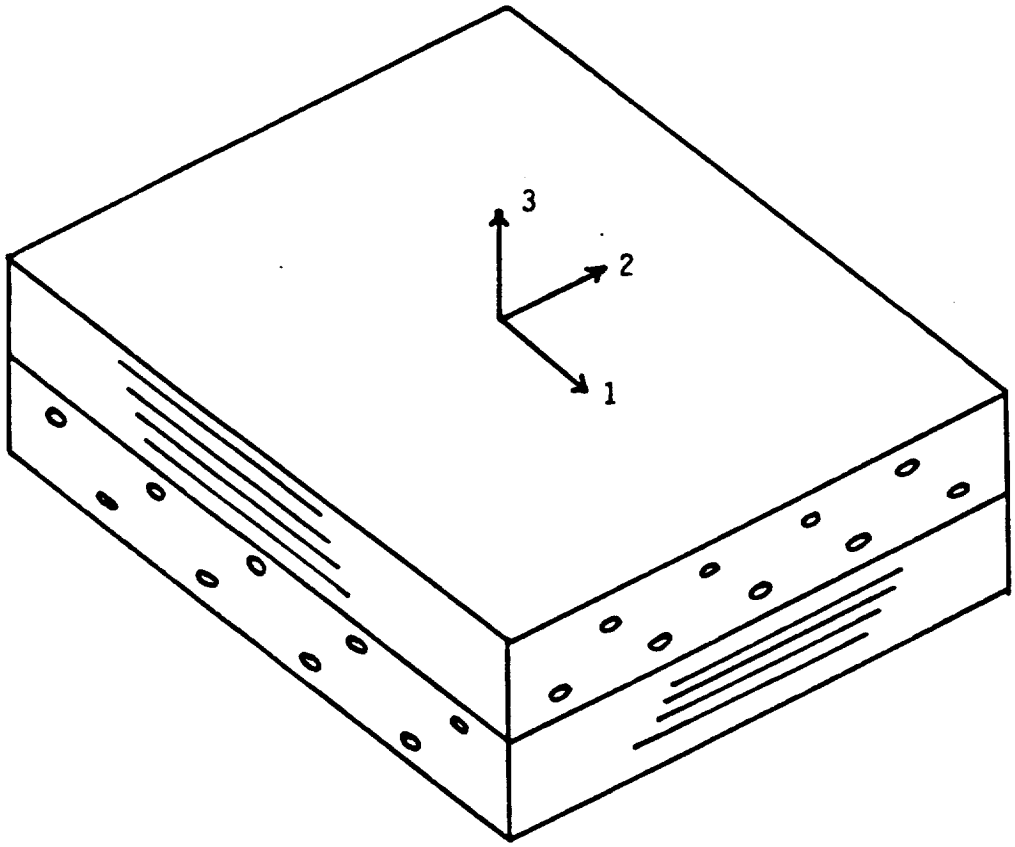

Figure 5.2 [0/90] Laminate and Reference Axes

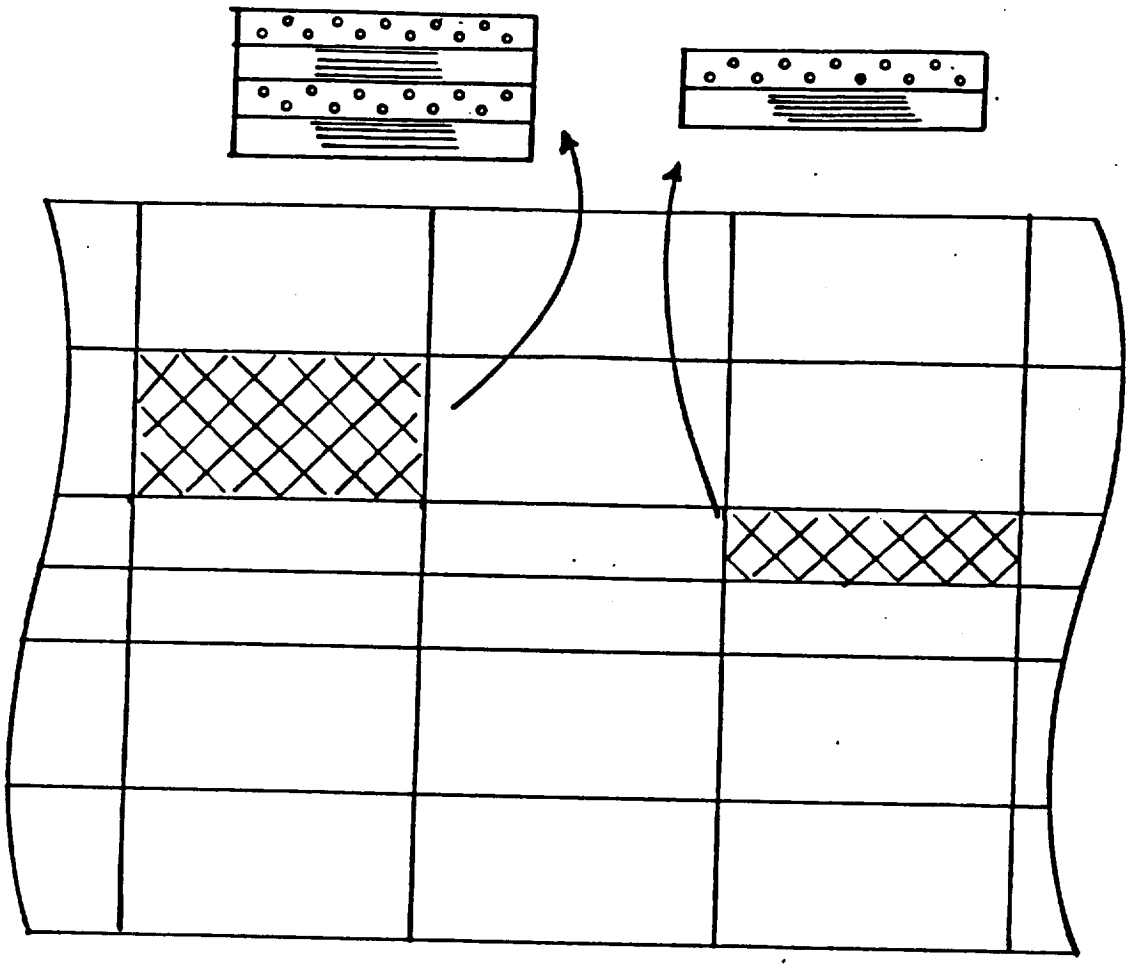

Lamina Properties:

$E_1 = 19.5 \times 10^6$ psi

$E_2 = 1.5 \times 10^6$ psi

$G_{12} = 0.725 \times 10^6$ psi

$\nu_{12} = \nu_{13} = \nu_{23} = 0.33$

$\rho = 1.49 \times 10^{-4} \frac{lb.s^2}{in^4}$

Finite Element Constants:

$\bar{E}_1 = \bar{E}_2 = 10.5 \times 10^6$ psi

$\bar{E}_3 = 1.5 \times 10^6$ psi

$\bar{G}_{12} = 0.725 \times 10^6$ psi

$\bar{\nu}_{13} = \bar{\nu}_{23} = 0.33$

$\bar{\nu}_{12} = 0.05$

Figure 5.3 Finite Element Discretization of $[90/0]_{5s}$ Graphite/Epoxy Laminate Remote from Crack Tip

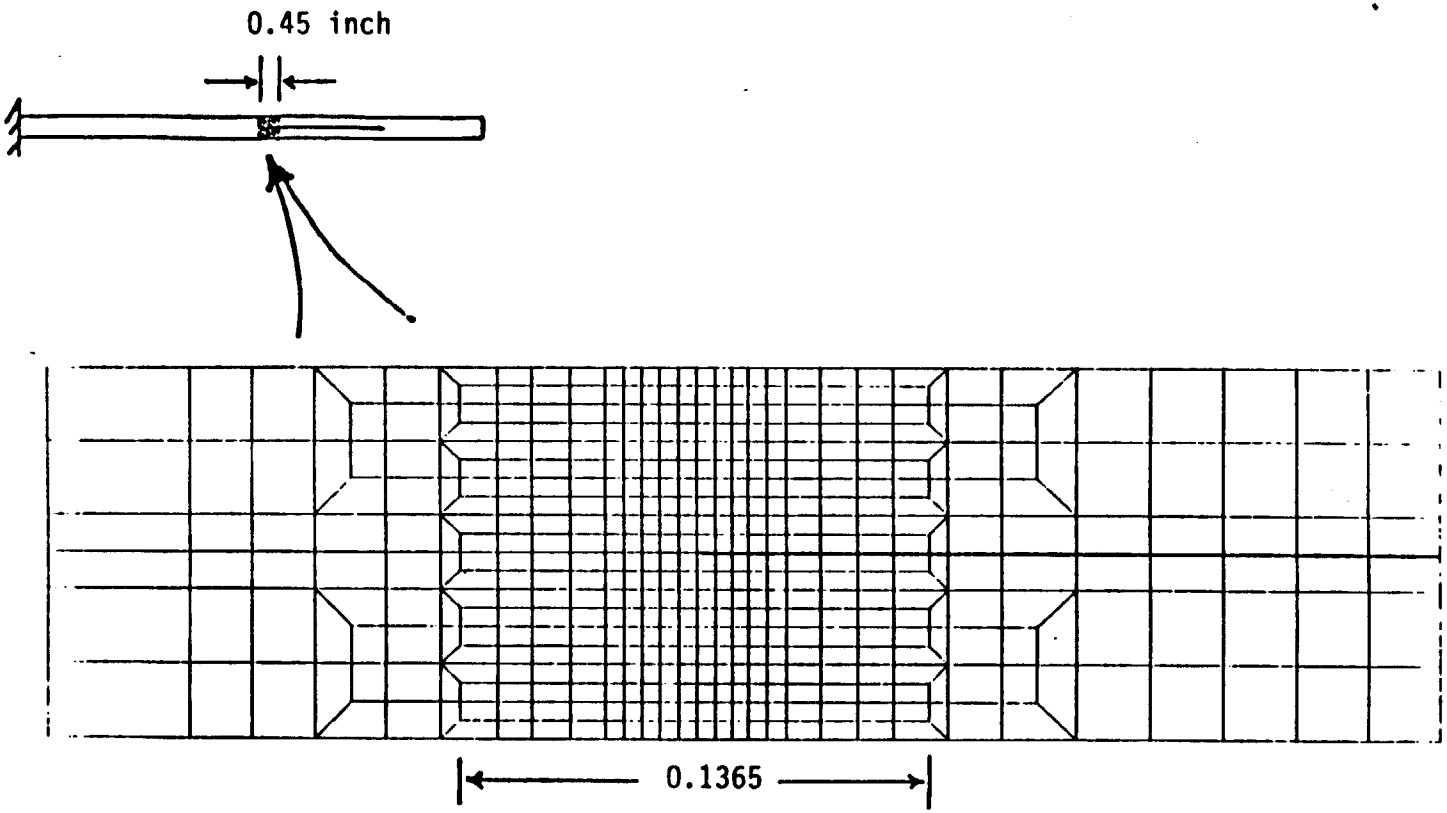

Figure 5.4 Finite Element Mesh Gradient Near Crack Tip

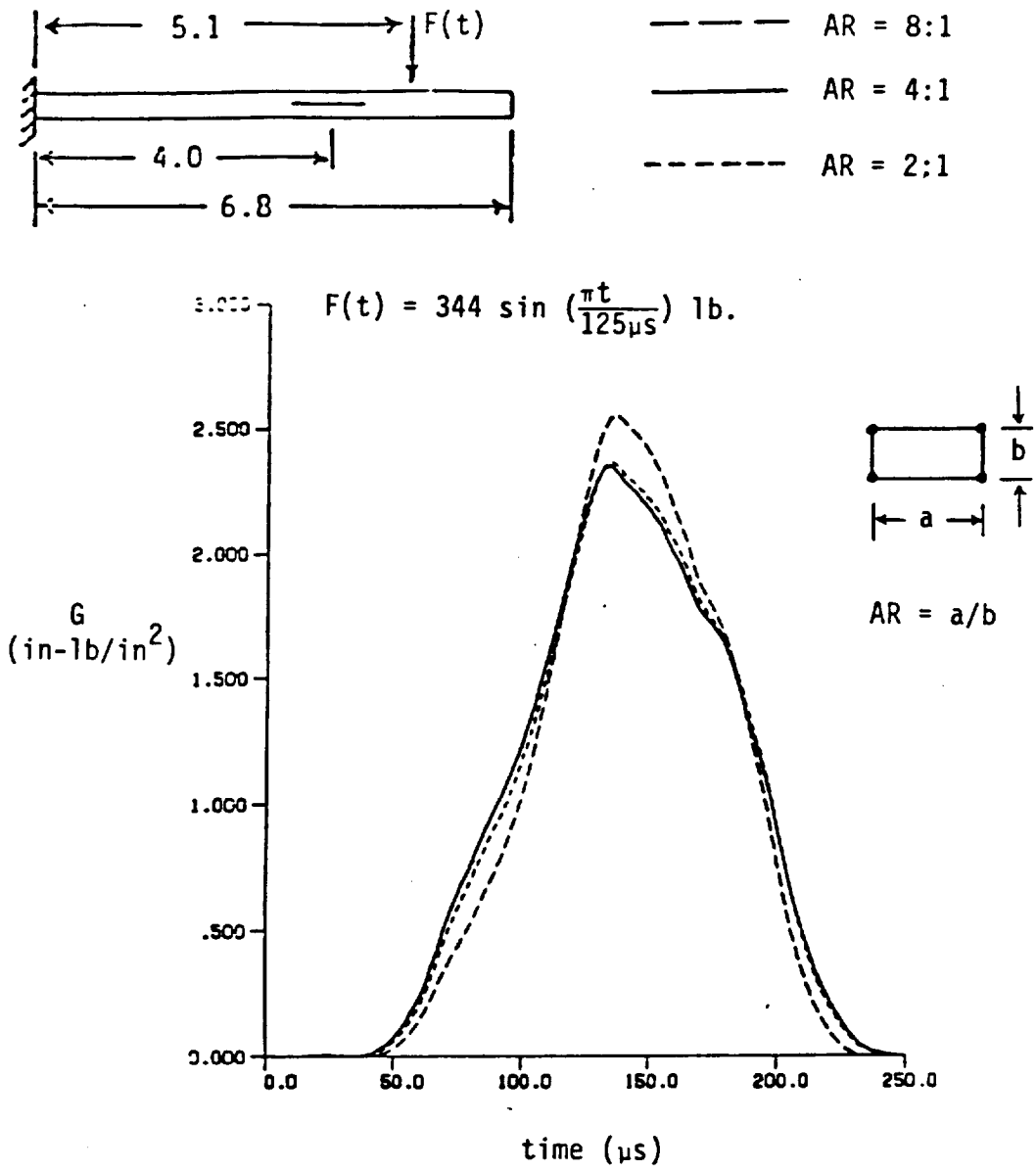

Figure 5.5 Effect of Remote Mesh Refinement on Crack Tip Response of Homogeneous Beam with 1.0 Inch Crack

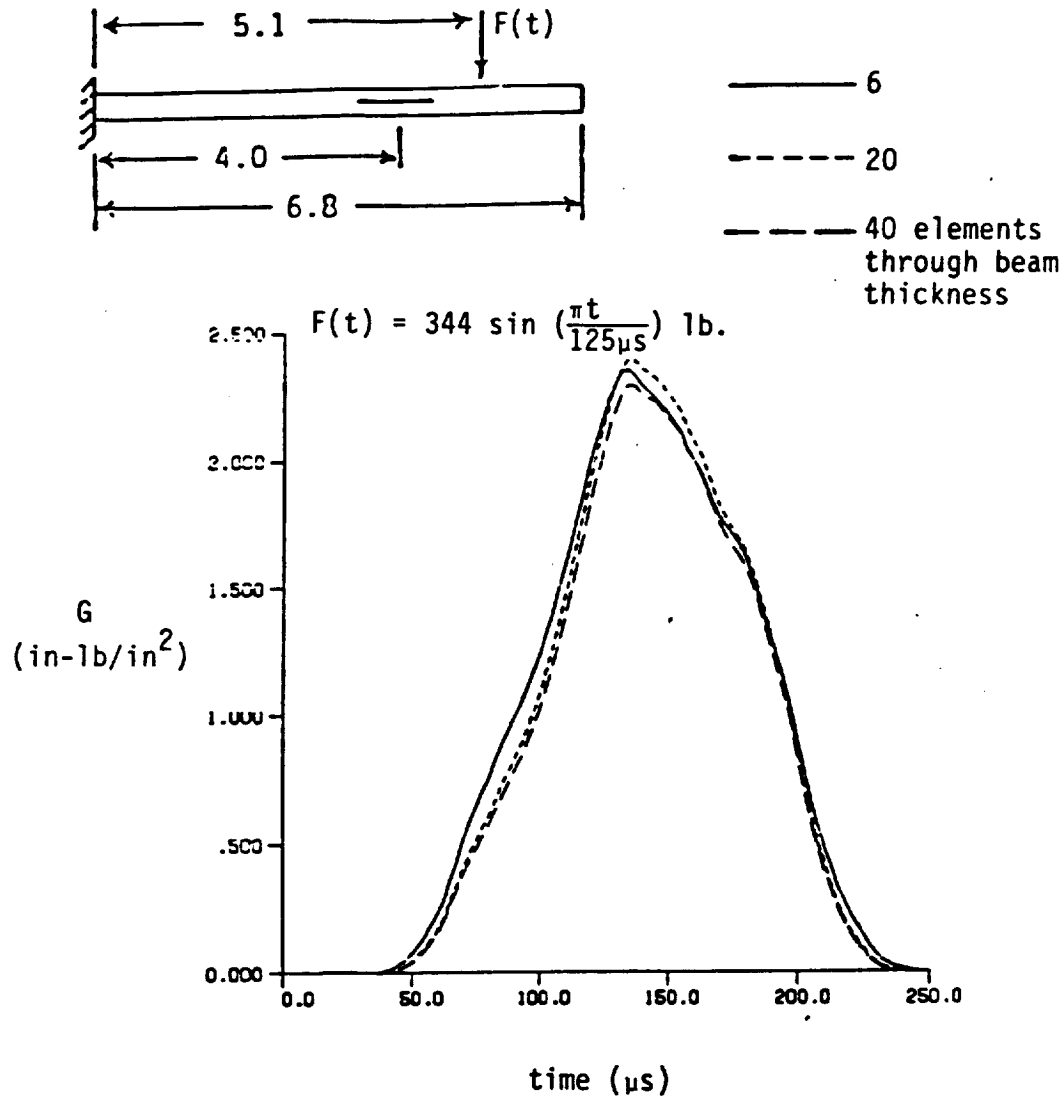

Figure 5.6 Effect of Near Crack Tip Mesh Refinement on Crack Tip Response of Homogeneous Beam with 1.0 Inch Crack

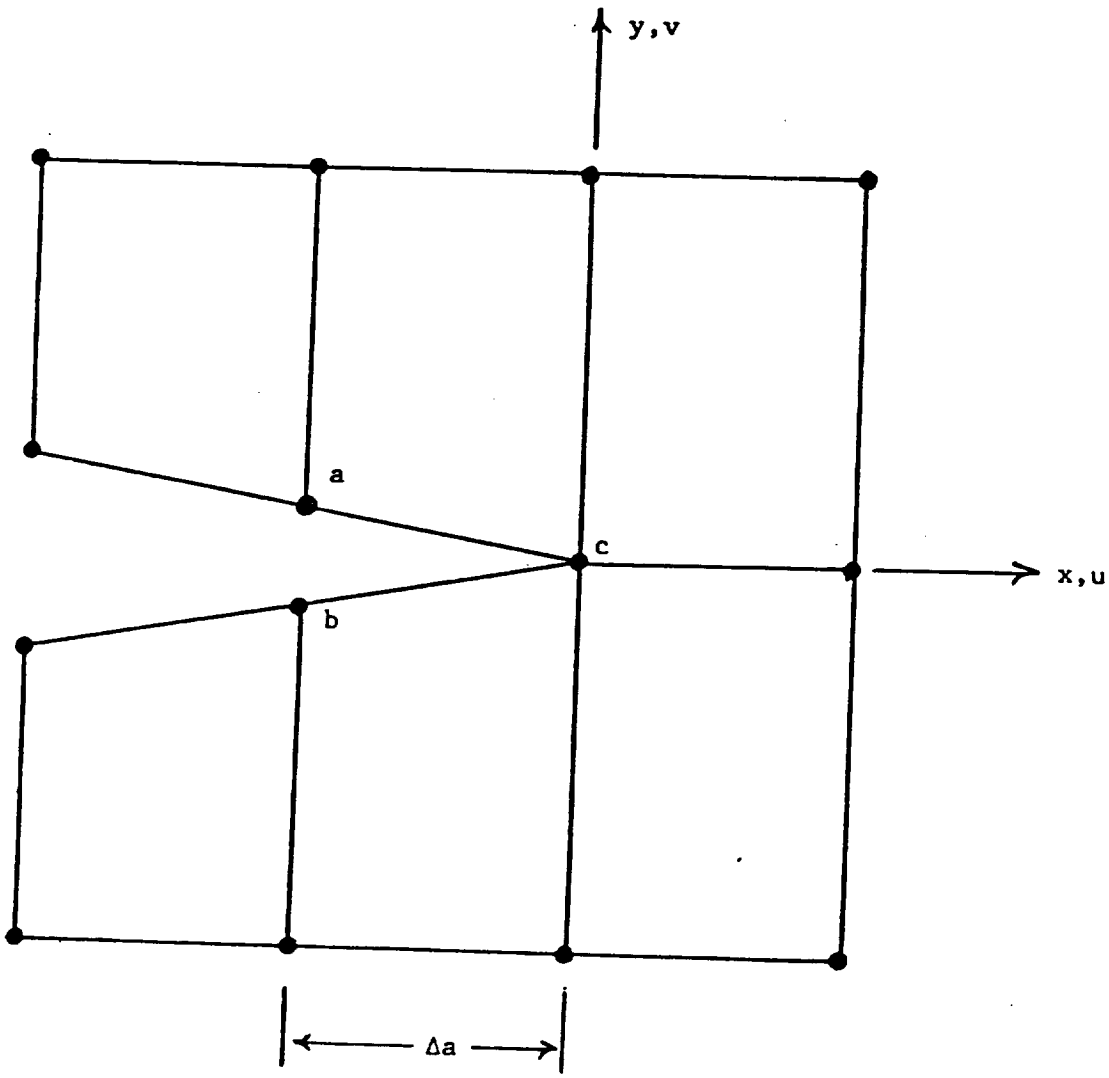

Figure 5.7 Crack Tip Notation

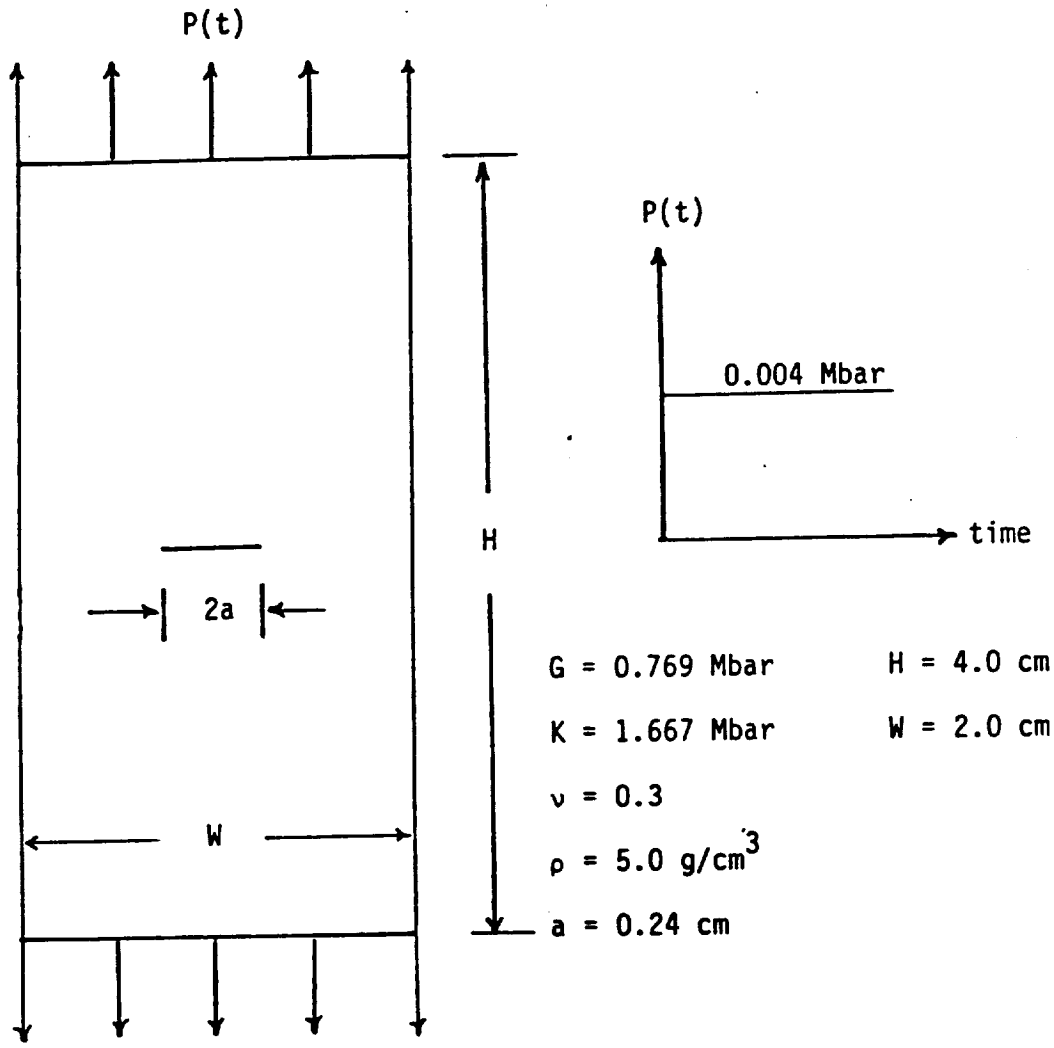

Figure 5.8 Center-Cracked Panel Problem

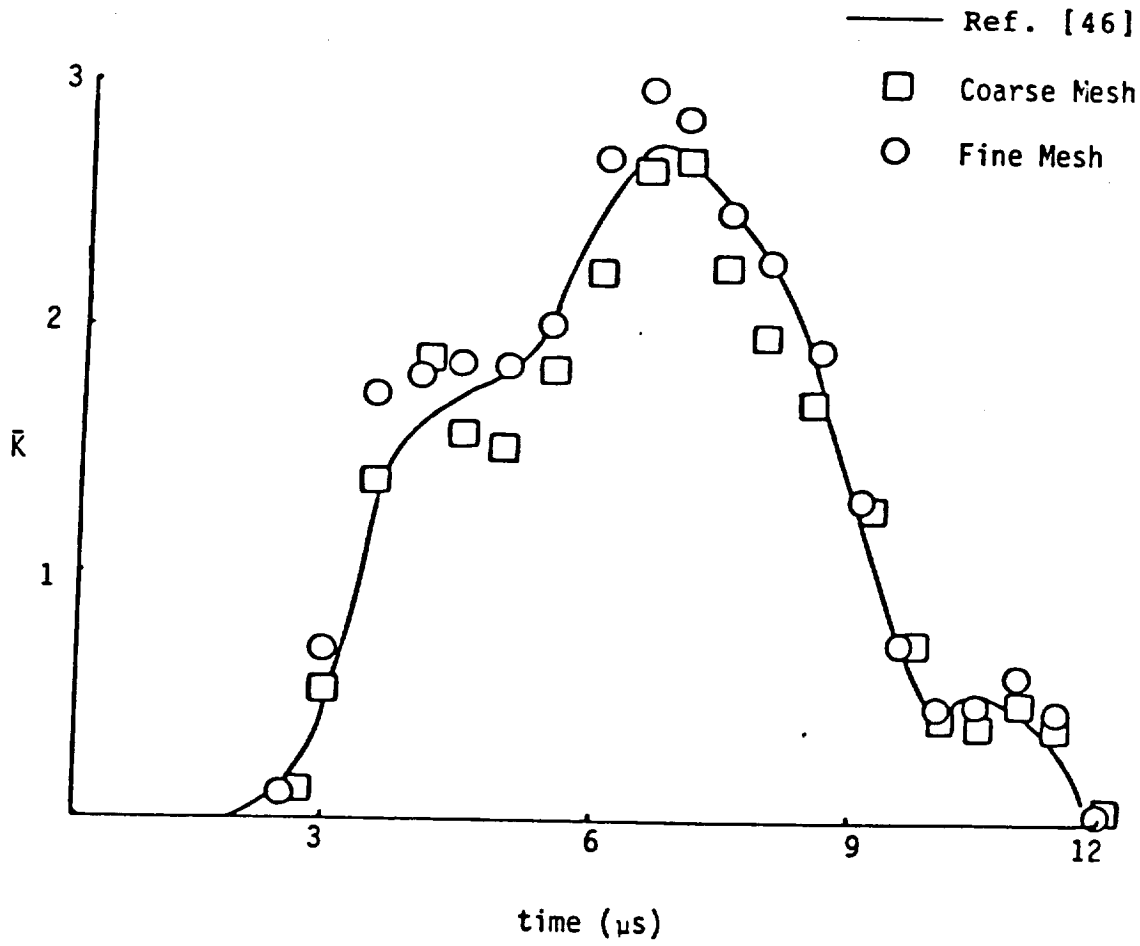

Figure 5.9 Dynamic Stress Intensity Factor for Center-Cracked Panel

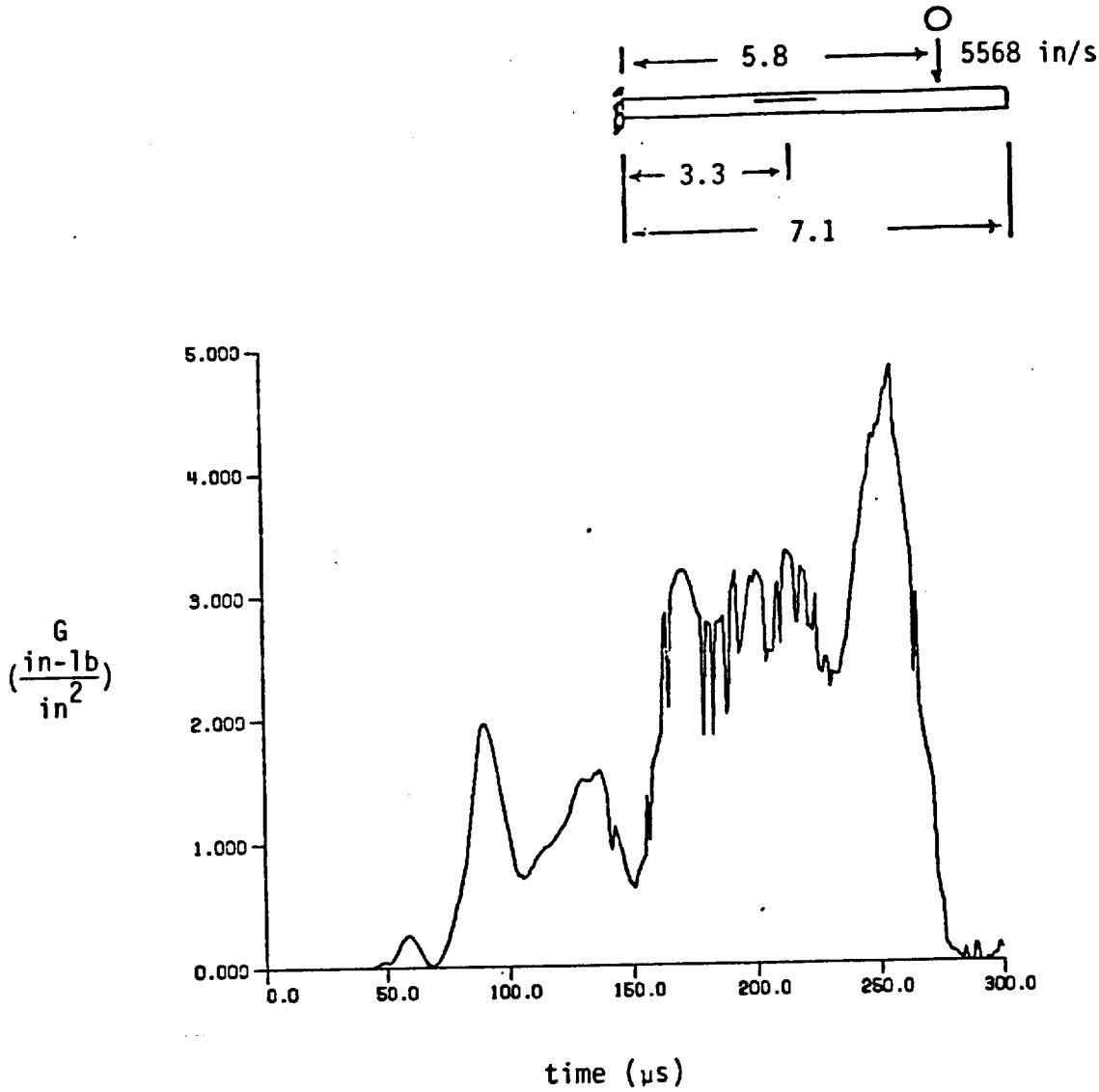

Figure 5.10 Dynamic Strain Energy Release Rate for Specimen Configuration A

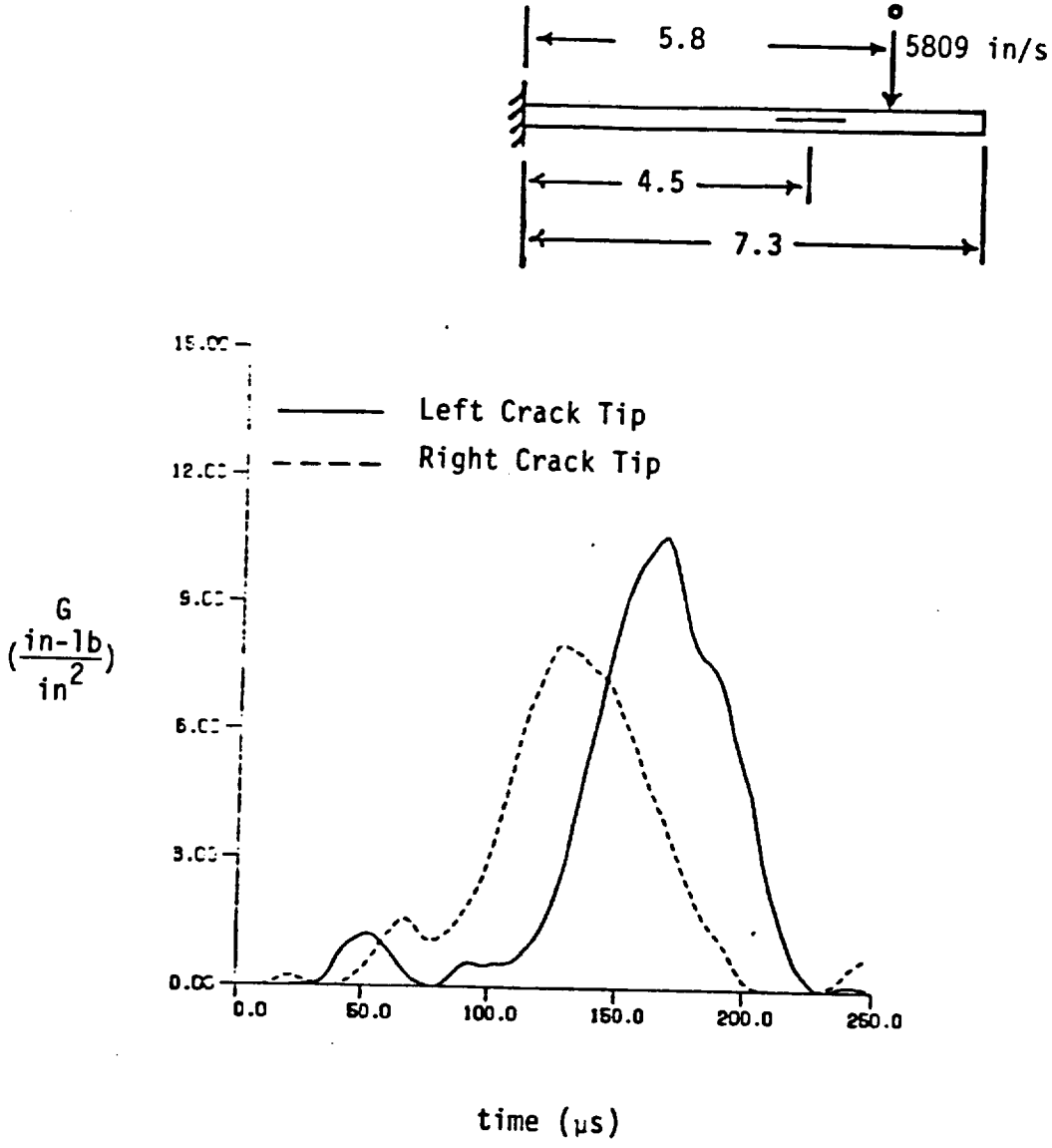

Figure 5.11 Dynamic Strain Energy Release Rate for Specimen Configuration B

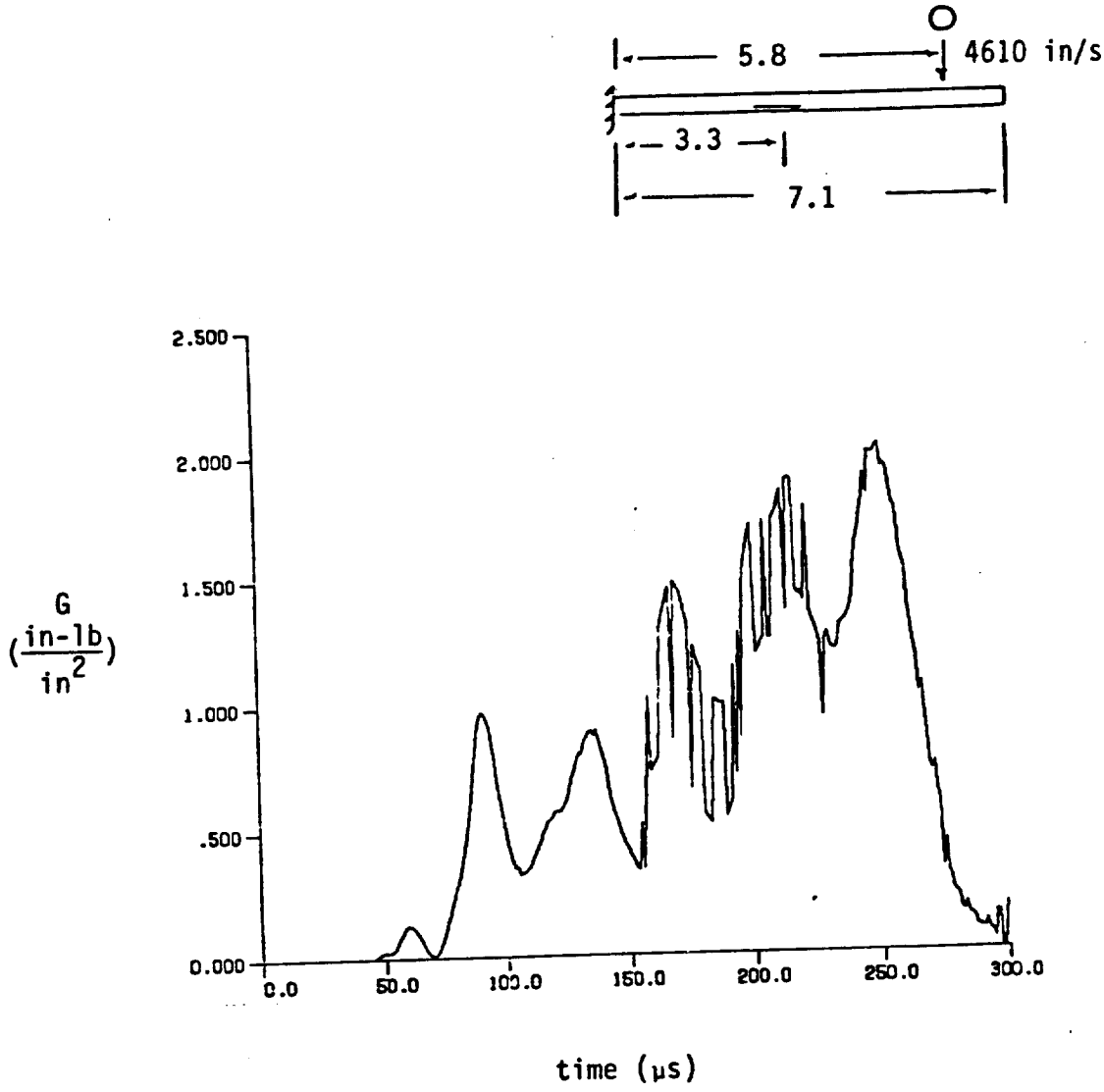

Figure 5.12 Dynamic Strain Energy Release Rate for Specimen Configuration C

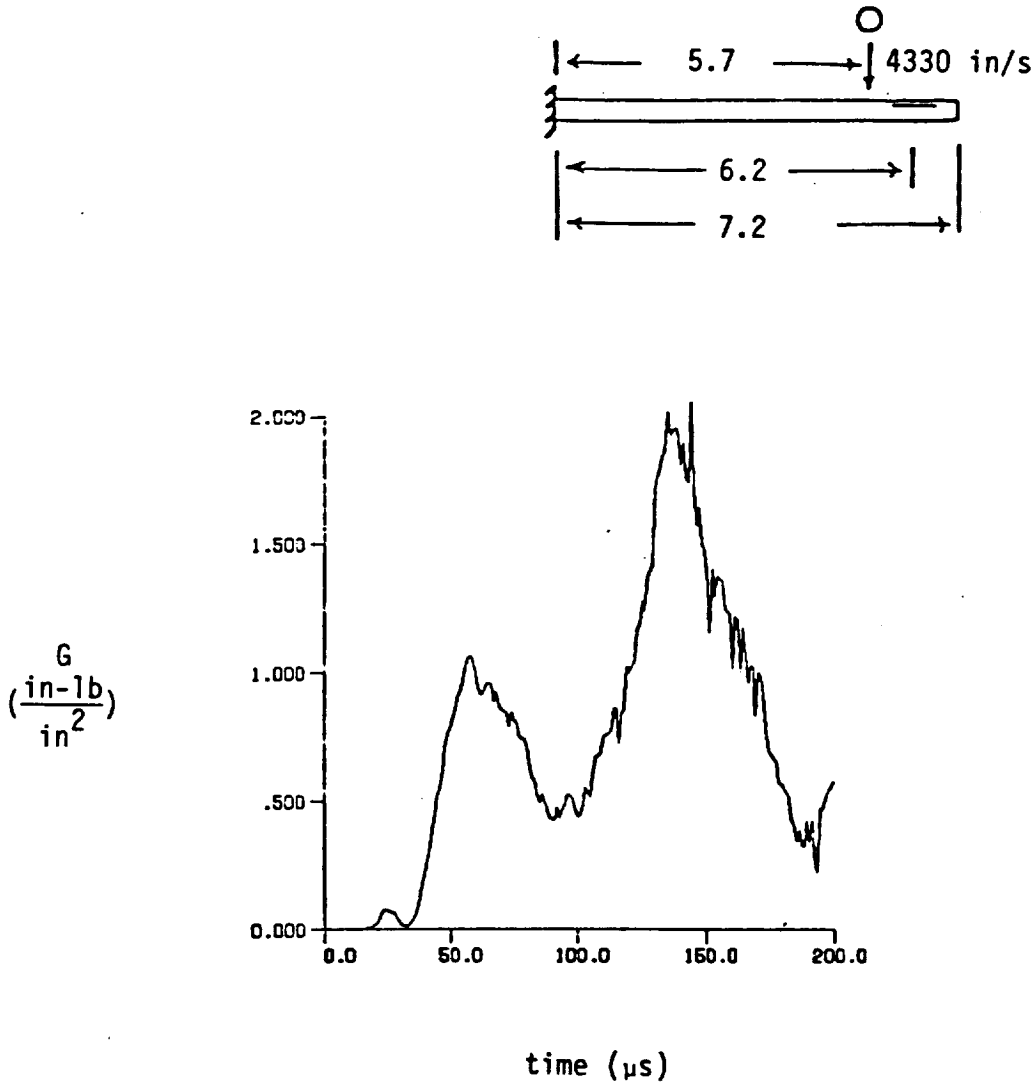

Figure 5.13 Dynamic Strain Energy Release Rate for Specimen Configuration D

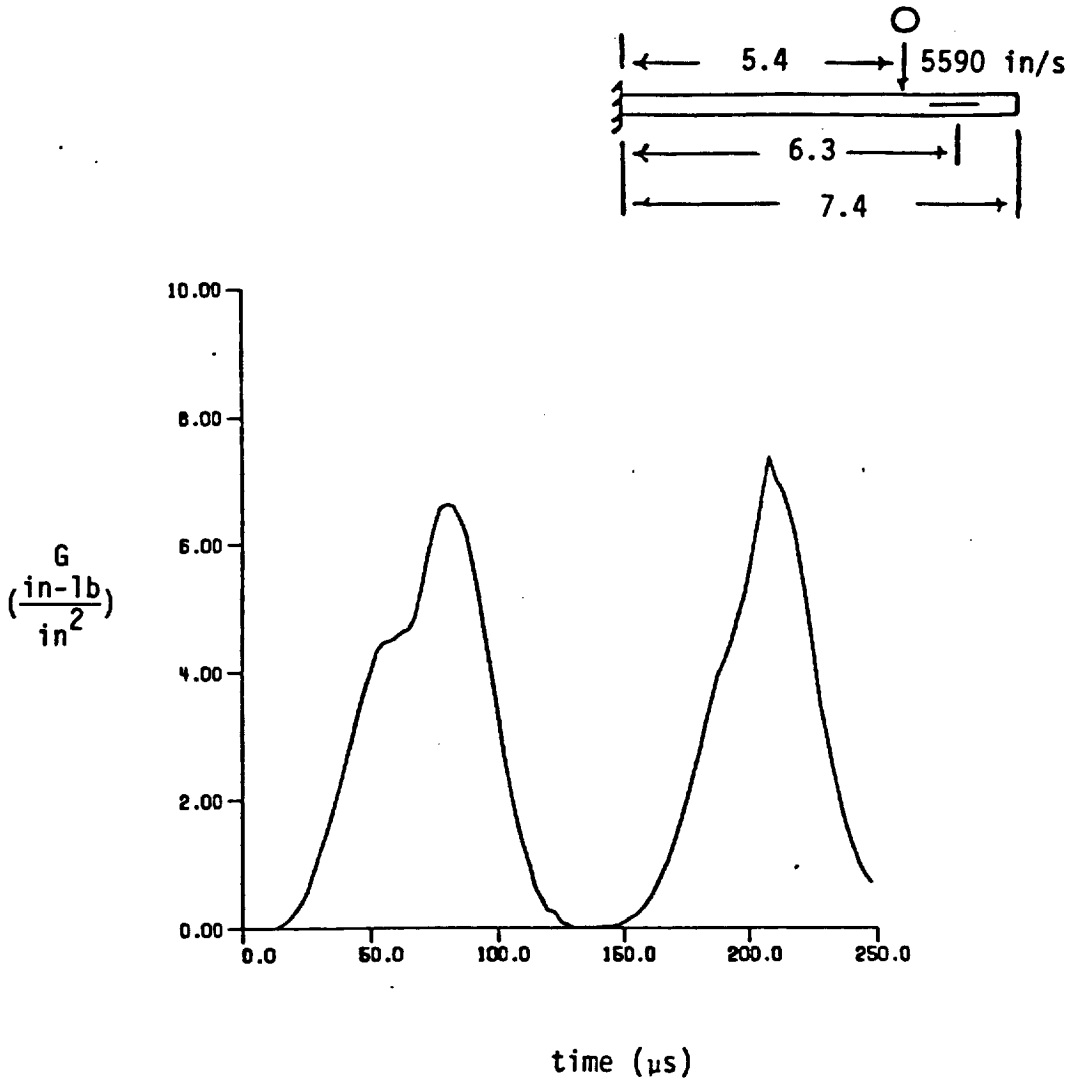

Figure 5.14 Dynamic Strain Energy Release Rate for Specimen Configuration E

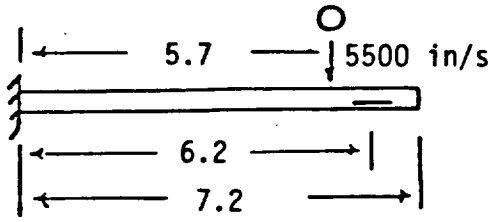

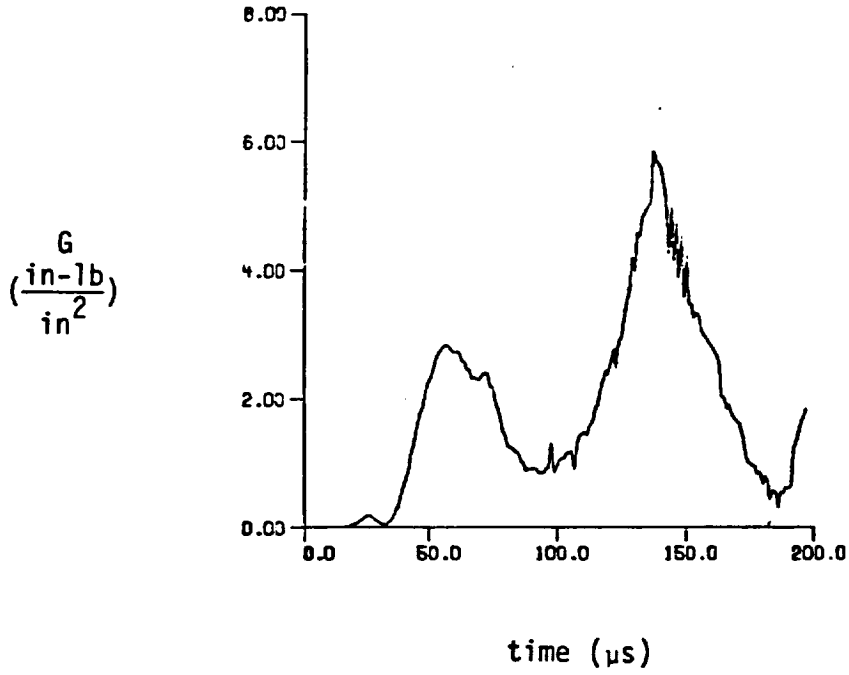

Figure 5.15 Dynamic Strain Energy Release Rate for Specimen Configuration F

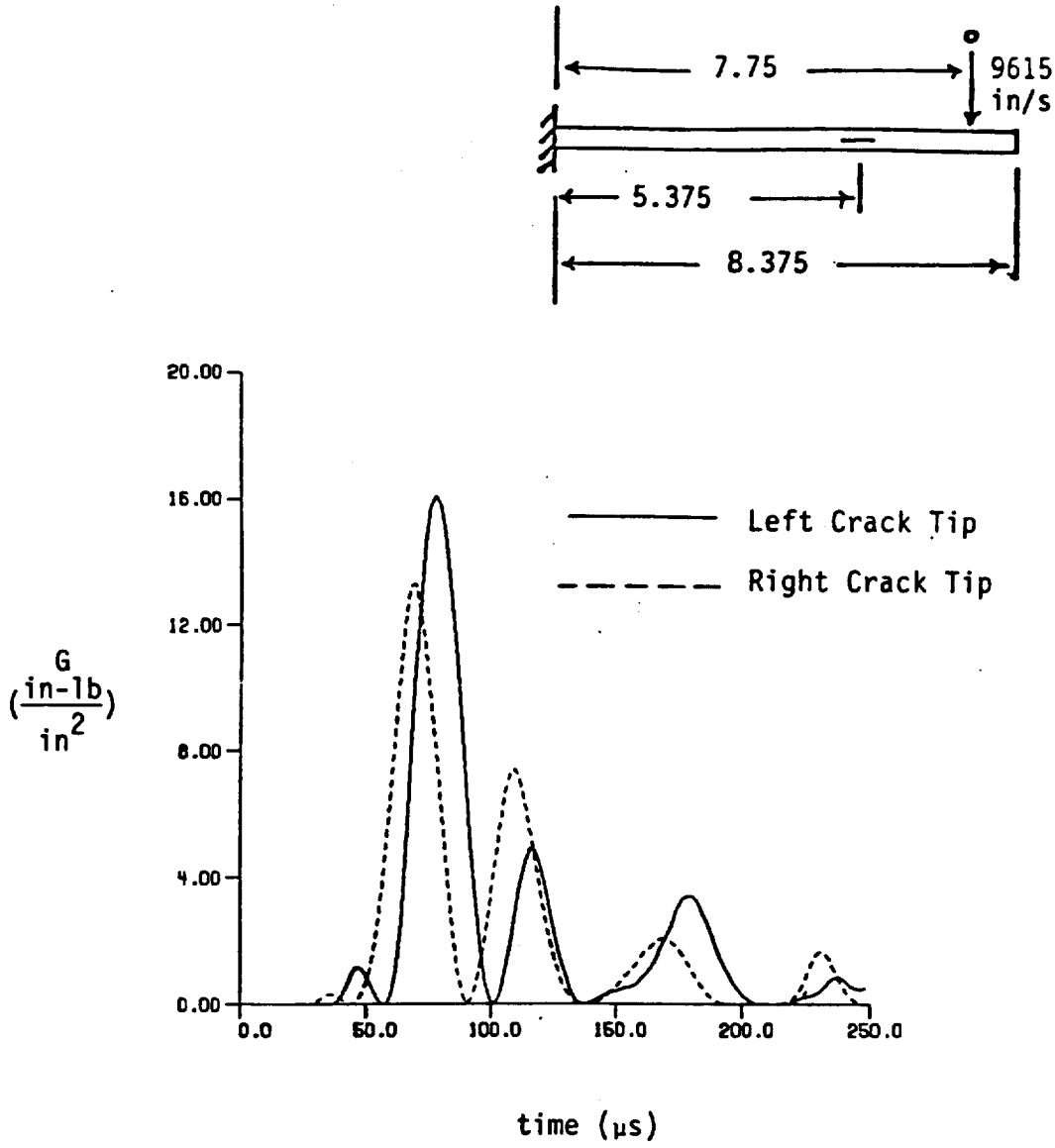

Figure 5.16 Dynamic Strain Energy Release Rate for Specimen Configuration G

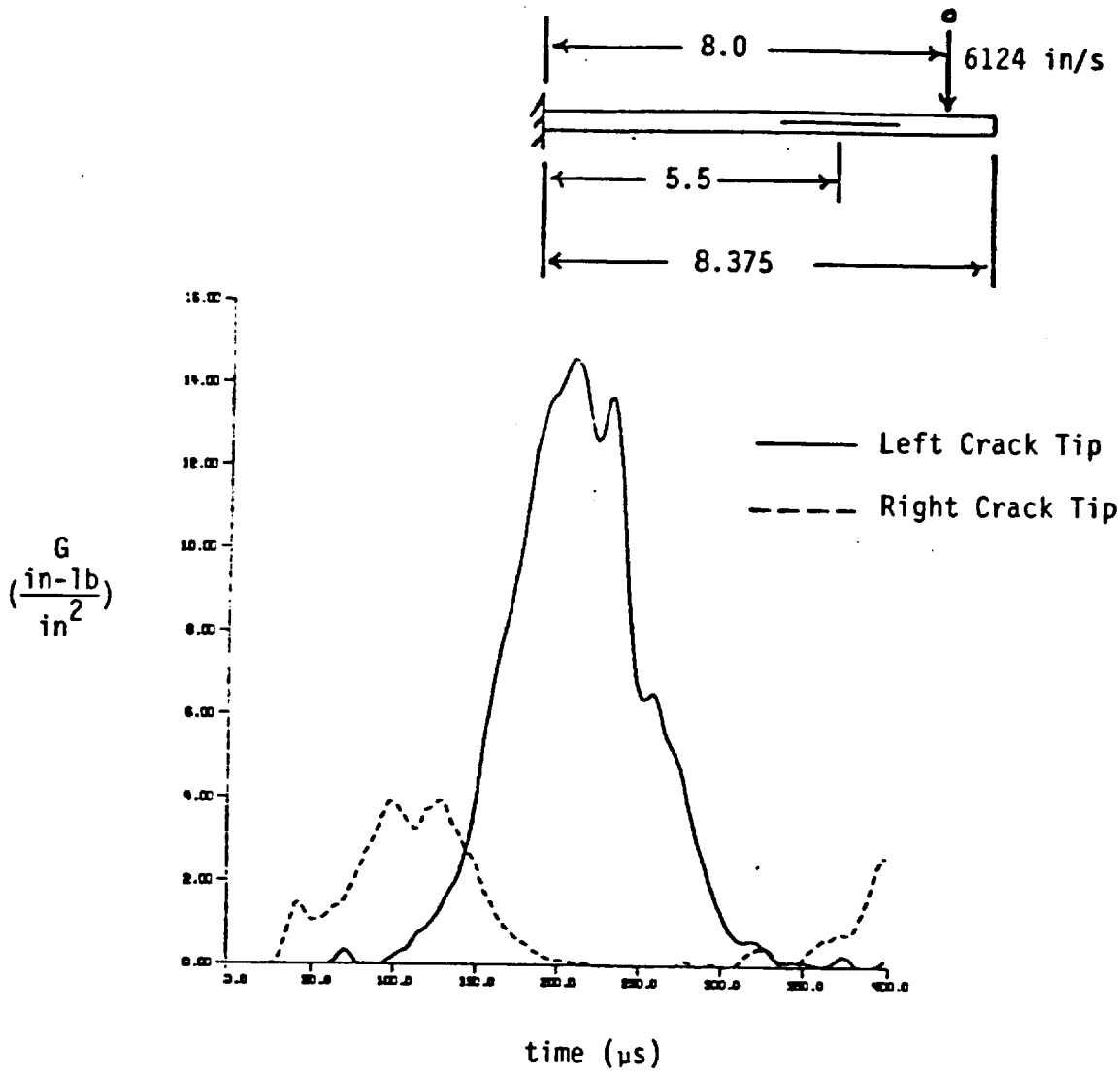

Figure 5.17 Dynamic Strain Energy Release Rate for Specimen Configuration H

6. SUMMARY

Dynamic delamination crack propagation in a $[90/0]_{5s}$ Graphite/Epoxy laminate with an embedded interfacial crack was investigated experimentally using high speed photography. The dynamic motion was produced by impacting the beam-like laminate specimen with a silicon rubber ball. The threshold impact velocities required to initiate dynamic crack propagation in laminates with varying initial crack positions were determined. The crack propagation speeds were estimated from the photographs.

Experimental results show that the through-the-thickness position of the embedded crack can significantly affect the dominant mechanism and the threshold impact velocity for the onset of crack movement. If the initial delamination is placed near the top or bottom surface of the laminate, local buckling of the delaminated plies may cause instability of the crack. If the initial delamination lies on the midplane, local buckling does not occur and the initiation of crack propagation appears to be dominated by Mode II fracture. The crack propagation and arrest observed was seen to be affected by wave motion within the delaminated region.

The contact behavior between the compliant impactor and the laminate could not be adequately described by the classical Hertzian contact law due to the extent of the deformation and the change in

shape undergone by the impactor during the contact interval. An empirical model was therefore used to describe the variation of the impact force history with impact velocity. Impact tests of an uncracked laminate instrumented with strain gages were used to determine the variation of the force history with impact velocity for the rubber impactor. It was found that a three-parameter description of the force history was necessary to adequately estimate the actual contact force. The variation of contact force with time is characterized in this model by two quarter-sine waves of different periods; the first represents the loading phase of the force history and the second represents the unloading phase. The assumed force history was varied in the finite element analysis of the uncracked laminate until the calculated strain response sufficiently matched the measured response. It was found that the variation of force history with impact velocity for the transverse impact of the beam-like laminate followed the same trends as in the case of longitudinal impact of a prismatic bar. Boundary effects due to wave reflections were not significant in the latter case, but were seen to have a considerable effect on the force history for the beam specimens. This was due primarily to the length of the beam specimens used, and the long contact duration of the impactor. As a result, the Force History versus Impact Velocity data from these tests did not follow the trends predicted by the simple single-degree-of-freedom spring-mass model of interaction between the impactor and target, in which wave effects are not considered.

Calcuation of the dynamic strain energy release rate prior to crack extension for specimens of several different geometries indicate that there may exist a critical value of this parameter above which a delamination crack will become unstable.

The experimental procedure used here can be improved in several ways. Uniformity of the test specimens is necessary whenever the results of several tests are to be compared. This was particularly important in determining the threshold impact velocities. In fact, there were small variations in the length of the composite beam specimens, which may have affected the accuracy of the estimate of threshold velocity in some cases. More significantly, vibration of the long barrel of the air gun caused some variation in the location of the impact on the specimens. The magnitude of these variations is shown in Tables 3.1-3.7. The distance between the crack tip and the impact site can appreciably affect the impact velocity required to cause the crack to extend, so this variation undoubtedly contributed to the scatter of the data shown in Figs. 3.2-3.7, from which the threshold impact velocities were determined. In several cases, the accuracy of the estimate of threshold velocity was hindered by the lack of sufficient data. The number of different specimen configurations tested should be limited, thus allowing more tests of each configuration.

A more complete evaluation of G_c as a criterion for crack extension could be performed if the time at which the initial crack extension occurred could be determined accurately from the experimental data. Comparison of the data and the analysis presented in Chapter 5 indicate that a higher speed camera would be more suitable for

experiments of this nature. A camera with a framing rate of one frame every ten microseconds would provide data from which a reasonably accurate estimate of the time of initial crack extension could be obtained. The calculated energy release rate at this time could then be used as an estimate of the critical value necessary to extend the crack.

The inverse method used to obtain the parameters describing the impact force history may have some inherent inaccuracy. Wave reflections from the boundaries of the relatively short impact specimens used contributed significantly to the observed strain response, and may have obscured that part of the response due solely to the contact of the impactor. Therefore, a longer beam would be more suitable if this approach is used to obtain impact force characteristics of the impactor.

LIST OF REFERENCES

[1] Sendeckyj, G.P., Stalnaker, H.D., and Kleismit, R.A., "Effect of Temperature on Fatigue Response of Surface-Notched $[(0/\pm45/0_s]_3$ Graphite/Epoxy Laminate," Fatigue of Filamentary Composite Materials, ASTM STP 636, K.L. Reifsnider and K.N. Lauraitis, Eds., American Society for Testing and Materials, 1977, pp. 123-140.

[2] Rodini, B.T. and Eisenmann, J.R., "An Analytical and Experimental Investigation of Edge Delamination in Composite Laminates," Fibrous Composites in Structural Design, Plenum Press, 1980, pp. 441-457.

[3] Raju, I.S., and Crews, J.H., Jr., "Interlaminar Stress Singularities at a Straight Free Edge in Composite Laminates," Computers and Structures, Vol. 14, No. 1-2, 1981, pp. 21-28.

[4] Crossman, F.W., and Wang, A.S.D., "The Dependence of Transverse Cracking and Delamination on Ply Thickness in Graphite/Epoxy Laminates," Damage in Composite Materials, ASTM STP 775, K.L. Reifsnider, Ed., American Society for Testing and Materials, 1982, pp. 118-139.

[5] Roderick, G.L., Everett, R.A., and Crews, J.H., "Debong Propagation in Composite-Reinforced Metals," Fatigue of Composite Materials, ASTM STP 569, American Society for Testing and Materials, 1975, pp. 295-306.

[6] Rybicki, E.F., Schmueser, D.W., and Fox, J., "An Energy Release Rate Approach for Stable Crack Growth in the Free-Edge Delamination Problem," Journal of Composite Materials, Vol. 11, 1977, pp. 470-487.

[7] Wang, A.S.D. and Crossman, F.W., "Initiation and Growth of Transverse Cracks and Edge Delamination in Composite Laminates," Journal of Composite Materials, Supplementary Vol. 14, 1980, pp. 71-106.

[8] O'Brien, T.K., "Characterization of Delamination Onset and Growth in a Composite Laminate," Damage in Composite Materials, ASTM STP 775, K.L. Reifsnider, Ed., American Society for Testing and Materials, 1982, pp. 140-167.

[9] Wilkins, D.J., Eisenmann, J.R., Camin, R.A., Margolis, W.S., and Benson, R.A., "Characterizing Delamination Growth in Graphite/ Epoxy," Damage in Composite Materials, ASTM STP 775, K.L. Reifsnider, Ed., American Society for Testing and Materials, 1982, pp. 168-183.

[10] Graff, K. Wave Motion in Elastic Solids, Ohio State University Press, 1975, pp. 133, 100-108.

[11] Kraft, J.M., and Irwin, G.R., "Crack Velocity Considerations," ASTM STP 381, 1965, pp. 114-129.

[12] Broek, D. Elementary Engineering Fracture Mechanics, Martinus Nijhoff Publishers, 1984, pp. 165-167.

[13] Kanninen, M.F., "An Augmented Double Cantilever Beam Model for Studying Crack Propagation and Arrest." International Journal of Fracture, Vol. 9, 1973, pp. 83-92.

[14] Kanninen, M.F., Gehlen, P.C., Barnes, C.R., Hoagland, R., and Hahn, G.T., "Dynamic Crack Propagation Under Impact Loading," Nonlinear and Dynamic Fracture Mechanics, (ed. S. Atluri and N. Perrone) ASME AMD Vol. 35, 1979, pp. 185-200.

[15] Williams, J.H., Jr., Lee, S.S., and Kousiounelos, P.N., "Dynamic Crack Propagation and Arrest in Orthotropic DCB Fiber Composite Specimens," Engineering Fracture Mechanics, Vol. 14, 1981, pp. 427-438.

[16] Hoagland, R.G., Rosenfield, A.R., and Hahn, G.T., "Mechanisms of Fast Fracture and Arrest in Steels," Metallurgical Transactions, Vol. 3, 1972, pp. 123-136.

[17] Hahn, G.T., Hoagland, R.G., and Rosenfield, A.R., "Dynamic Crack Propagation and Arrest in Structural Steels," Final Report on Project SR-201 to the Naval Ship Engineering Center, 1976.

[18] Hahn, G.T., Hoagland, R.G., and Rosenfield, A.R., "Influence of Metallurgical Factors on the Fast Fracture Energy Absorption Rates," Metallurgical Transactions, Vol. 7A, 1976, pp. 49-54.

[19] Kobayashi, A.S. and Mall, S., "Rapid Crack Propagation and Arrest in Polymers," Office of Naval Research Technical Report No. 30, 1977.

[20] Kobayashi, T., and Dally, J.W., "Relations Between Crack Velocity and the Stress Intensity Factor in Birefrinsent Polymers, Fast Fracture and Crack Arrest, ASTM STP 627, 1977, pp. 257-273.

[21] Kaltoff, J., Beinert, J. and Winkler, S., "Measurements of Dynamic Stress Intensity Factors for Fast Running and Arresting

[46] Chen, Y.M., "Numerical Computation of Dynamic Stress Intensity Factors by a Lagrangian Finite Difference Method," Engineering Fracture Mechanics, Vol. 7, 1975, pp. 653-660.

[47] Nilsson, F., "A Note on the Stress Singularity at a Non-Uniformly Moving Crack Tip," Journal of Elasticity, Vol. 4, No. 1, 1974, pp. 73-75.

[48] Grady, J.E., and Sun, C.T., "An Experimental Study of Dynamic Delamination in Graphite/Epoxy Laminates", NASA Contractor Report, submitted for publication.

REPORT DOCUMENTATION PAGE

Form Approved
OMB No. 0704-0188

1. AGENCY USE ONLY (*Leave blank*)	2. REPORT DATE	3. REPORT TYPE AND DATES COVERED
	October 1991	Final Contractor Report

4. TITLE AND SUBTITLE

Dynamic Delamination Crack Propagation in a Graphite/Epoxy Laminate

5. FUNDING NUMBERS

WU-505-63-5B

6. AUTHOR(S)

J.E. Grady and C.T. Sun

7. PERFORMING ORGANIZATION NAME(S) AND ADDRESS(ES)

Purdue University
School of Aeronautics and Astronautics
West Lafayette, Indiana 47907

8. PERFORMING ORGANIZATION REPORT NUMBER

None

9. SPONSORING/MONITORING AGENCY NAMES(S) AND ADDRESS(ES)

National Aeronautics and Space Administration
Lewis Research Center
Cleveland, Ohio 44135-3191

10. SPONSORING/MONITORING AGENCY REPORT NUMBER

NASA CR-187226

11. SUPPLEMENTARY NOTES

Project Manager, C.C. Chamis, Structures Division, NASA Lewis Research Center, (216) 433-3252.

12a. DISTRIBUTION/AVAILABILITY STATEMENT

Unclassified - Unlimited
Subject Category 24

12b. DISTRIBUTION CODE

13. ABSTRACT (*Maximum 200 words*)

Dynamic delamination crack propagation in a [90/0] 5s Graphite/Epoxy laminate with an embedded interfacial crack was investigated experimentally using high speed photography. The dynamic motion was produced by impacting the beam-like laminate specimen with a silicon rubber ball. The threshold impact velocities required to initiate dynamic crack propagation in laminates with varying initial crack positions were determined. The crack propagation speeds were estimated from the photographs. Results show that the through-the-thickness position of the embedded crack can significantly affect the dominant mechanism and the threshold impact velocity for the onset of crack movement. If the initial delamination is placed near the top or bottom surface of the laminate, local buckling of the delaminated plies may cause instability of the crack. If the inital delamination lies on the midplane, local buckling does not occur and the initiation of crack propagation appears to be dominated by Mode II fracture. The crack propagation and arrest observed was seen to be affected by wave motion within the delamination region.

14. SUBJECT TERMS

Fiber composites; Experimental; Embedded; Near-surface; Mid-plane sublaminate buckling; Fracture toughness; Crack arrest; Mode I; Mode II

15. NUMBER OF PAGES
160

16. PRICE CODE
A08

17. SECURITY CLASSIFICATION OF REPORT	18. SECURITY CLASSIFICATION OF THIS PAGE	19. SECURITY CLASSIFICATION OF ABSTRACT	20. LIMITATION OF ABSTRAC
Unclassified	Unclassified	Unclassified	